Biophotonics characterization of upconversion nanoparticles

by Lei DING

Thesis submitted in fulfilment of the requirements for the degree of

Doctor of Philosophy

under the supervision of Prof. Igor Aharonovich, Dr. Fan Wang

University of Technology Sydney
Faculty of Science

21/07/2022

Certificate of Original Authorship

I, Lei DING declare that this thesis is submitted in fulfilment of the requirements for the award of Doctor of Philosophy, in the School of Mathematical and Physical Sciences, Faculty of Science, at the University of Technology Sydney.

This thesis is wholly my own work unless otherwise reference or acknowledged. In addition, I certify that all information sources and literature used are indicated in the thesis.

This document has not been submitted for qualifications at any other academic institution.

This research is supported by the Australian Government Research Training Program and the China Scholarship Council Scholarship.

Signature:

Production Note:
Signature removed prior to publication.

Date: 21/07/2022

Acknowledgements

This thesis is the end of a long journey at UTS. It would not have been possible without the support and help from my family, supervisors, colleagues, and friends.

I would like to express my greatest gratitude to my supervisors. I thank **Prof. Igor Aharonovich** for timely help whenever I need it. I thank **Dr. Fan Wang** for offering me the extraordinary opportunity to work on optical technologies and for providing tremendous suggestions and guidance on my projects. I benefit a lot from your passion and dedication to research. I thank **Dr. Qiang Fu** for discussing the TTA project and for timely help whenever I need it. I thank **Prof. Dayong Jin** and **Pof. Jiajia Zhou** for their acceptance and supervision at the beginning of my PhD study.

I am grateful to all **Fan's Group members** that I have worked with during the past years. I particularly thank **Xuchen** for the great help with optical tweezers, Matlab, and Labview. I thank **Baolei** for teaching me optical knowledge and Matlab. I thank **Chaohao** for the help with super-resolution knowledge and experiments. I thank **Kevin** for keeping the Photonic Lab running and giving prompt assistance whenever it is required. I thank **Prof. David McGloin** and **Dr. Peter Reece** for their optical help.

I thank all the colleagues and friends in Photonic Lab and Faculty of Science: **Xiangjun** and **Dejiang** for the assistance in biological experiments and delicious food in daily life; **Ziqing**, **Shihui**, and **Xiaoxue** for the help with lanthanide-doped nanoparticles; **Ling**, for the happy chat during lunch; **Anna**, for discussion and instant help about optical tweezers; **Guochen**, for the chichat about life and fishing, and the help about organic synthesis in the first two years of my PhD study; **Guocheng**, for the car-service for relaxing at the weekend; **Mahnaz**, for the polymers for modifying nanoparticles and casual talk; **Peter (Qian)**, for the biological dishes; **Jiayan**, for the help about nanoparticles.

I thank my drinking buddies and basketball friends, **Dejiang**, **Chi**, **Milad**, **Xiaofei**, and **Mingshan**. I appreciate **Kang**, **Xuefei**, **Minghong** and **Feng** for the enjoyable time of talking and travelling.

Finally, I thank my family, **mother**, **father**, **sisters**, **aunt** and **uncles** for their continuous support and love throughout my whole life. I thank my girlfriend, **Hui**, for her understanding, care and support. I acknowledge the China Scholarship Council Scholarship for providing the scholarship.

Format of Thesis

This thesis is composed of six chapters. Chapter 1 is the introduction. Chapters 2-5 refer to the research results for the four goals (to see, sense, modulate, and develop new upconversion probes) in my PhD study. Chapter 6 gives the conclusion and perspective.

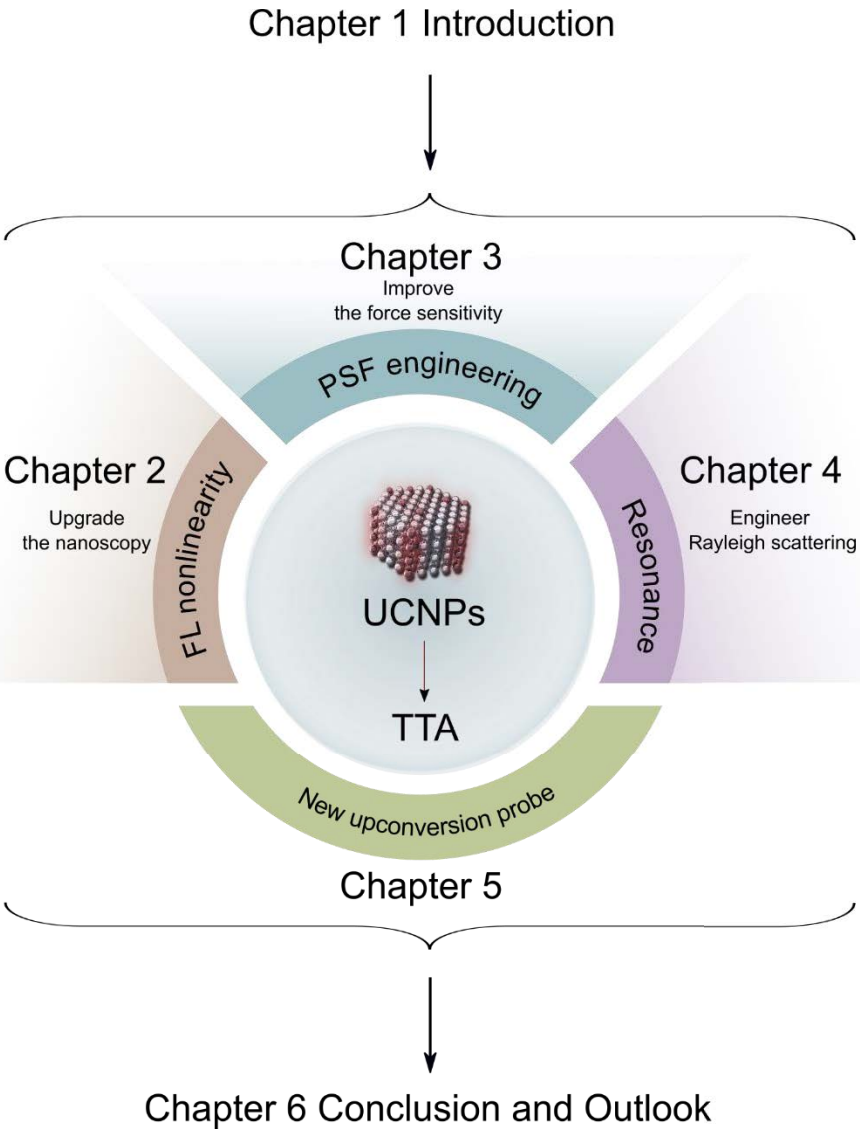

List of Publications

➢ Articles

1. **L. Ding**†, X. Shan†, P. Reece, I. Aharonovich and F. Wang*. Controlling Rayleigh scattering from lanthanide ion-doped nanoparticles. (*under review*)
2. X. Shan†, **L. Ding**† (co-first), S. Wen, J. Lu, J. Chennupati, X. Zhong*, D. Jin* and F. Wang*. Atto-Newton Force Sensitivity of Machine Learning Empowered Astigmatism Optical Tweezers. (*to be submitted*)
3. C. Chen†, **L. Ding**† (co-first), B. Liu and F. Wang*. Exploiting The Tunable Nonlinearity in Upconversion Nanoparticles for Super-resolution Imaging. (*under review*)
4. **L. Ding***, Q. Fu*, I. Aharonovich and F. Wang. Breaking Oxygen Quenching of Triplet–Triplet Annihilation Upconversion by Multidimensional Structures. (*to be submitted*)
5. **L. Ding**, J. Zhou*, Q. Fu, G. Bao, Y. Liu and D. Jin. Triplet-fusion Upconversion with Oxygen Resistance in Aqueous Media. Anal. Chem., 2021, 93, 4641–4646.
6. B. Liu, J. Liao, Y. Song, C. Chen, **L. Ding**, J. Lu, J. Zhou* and F. Wang*. Multiplexed Structured Illumination Super-Resolution Imaging with Lifetime-engineered Upconversion Nanoparticles. Nanoscale Adv., 2022.
7. X. Shan†, F. Wang†*, D. Wang, S. Wen, C. Chen, X. Di, P. Nie, J. Liao, Y. Liu, **L. Ding**, P. J. Reece* and D. Jin*. Optical Trapping Beyond Refractive Index Mismatch Using Highly Doped Nanoparticles. Nat. Nanotechnol., 2021, 1-7.
8. L. Zhang, K. Cook, A. Szmalenberg, B. Liu, **L. Ding**, F. Wang, D. McGloin*. Dual beam optical fiber traps for aerosols with angular deviation. Complex Light and Optical Forces XVI 12017, 2022, 126-132.

Table of Symbols

λ	laser wavelength	k_B	Boltzmann's constant
n	Refractive index	T	Temperature
σ_{sat}	Scattering cross-section	k	Stiffness
α	Polarizability	F_{ex}	Restoring force
ε	Permittivity	δ_{eq}	Position shift
φ	Phase difference	SD_{eq}	Standard deviation of position shift
I_r	Reflect light intensity	σ_k	Possibility variance of position
I_s	Scattering intensity	σ_p	Localisation accuracy
E_r	Reflect filed	ω	Angular frequency
E_s	Scattering field	k_m	Wavenumber
c_i	Energy transfer ratio	σ_i	Damping coefficient
k_{ij}	Cross-relaxation coefficient	ϕ_{UC}	UC quantum efficienc
a_{ij}	Branching ratio from energy level	η	Refraction cofficient
n_i	Population of photons	S_r	Sensitivity
w_i	Intrinsic decay rate	Q	Integral upconversion intensity
$F_i(x)$	Fluorescence intensities	$U(x)$	Potential energy
N_0	Fluorophore concentration	$g(x)$	Components of spatial information
k_B	Boltzmann's constant		

Abbreviations

UCNP	upconversion nanoparticle
HAADF-STEM	high-angle annular dark-field scanning transmission electron microscopy
Ln-NPs	lanthanide-doped nanoparticles
TEM	transmission electron microscopy
PSF	point spread function
TTA	triplet-triplet annihilation
ISC	intersystem crossing
NA	numerical aperture
STORM	stochastic optical reconstruction microscopy
PALM	photoactivated localisation microscopy
SIM	structured illumination microscopy
STED	stimulated emission depletion
SLM	spatial light modulator
QPD	quadrant photodiode detector
CCD	Charge-Coupled Device
CMOS	Complementary Metal Oxide Semiconductor
3D	three-dimensional
aN	attoNewton
iSCAT	interferometric scattering
SPAD	single-photon counting avalanche photodiode
FWHM	full width at half maximum
OA-VT	astigmatism video tracking
DNN	deep neural network

fN	femtoNewton
2D	two-dimensional
CL	cylindrical lens
PS	polystyrene sphere
M-iSCAT	multiplexed iSCAT
OA	oleic acid
ODE	1-octadecene
BF	bright-field
FL	fluorescence
PdTCPP	Pd(II) meso-Tetra(4-carboxyphenyl)porphine
QCDPA	5,5'-(9,10-anthracenediyl)diisophthalic acid
DMF	dimethyl formamide
NMR	nuclear magnetic resonance

Table of Contents

List of Figures

List of Tables

Abstract

Upconversion materials have attracted enormous attention for a broad range of applications in biological imaging, energy-related light harvesting, and sensing, due to their unique physicochemical properties. However, the comprehensive understanding and characterization of upconversion nanoparticles for novel applications remain challenging. In this thesis, we set four goals to refresh the present characterization and provide a wider and deeper cognition of these upconversion nanoparticles. After the delicate design of optical setups and nanomaterials, we realized the super resolution enhancement, optical force sensitivity improvement, Rayleigh scattering modulation, and a new water-soluble molecular upconversion probe.

Experimentally and theoretically, we upgrade the nanoscopy by exploiting the unique nonlinearity of upconversion nanoparticles using conventional confocal microscopy. We realize three-dimensional attoNewton-level optical force of optical via revolutionizing the configuration, data collection and accuracy analysis based on the property of upconversion nanoparticles. We refresh the morphology-independent method of engineering Rayleigh scattering at the nanoscale level based on the resonance effect of upconversion nanoparticles. We develop water-soluble molecular upconversion materials based on the ionic equilibrium of upconversion dyes. Based on the improved characterization of upconversion materials, as well as the technologies, we anticipate the potential applications in future, such as, deep tissue imaging, monitoring the interaction in the limit region (e.g., attoNewton level), and multiplexed scattering microscopy of cell dynamics.

Chapter 1 Introduction

Fluorescent probes have shown their magic in wide aspects, such as display, imaging, and sensing. Among these fluorescent materials, upconversion nanoparticles (UCNPs) become outstanding due to their many unique physicochemical properties, such as homogenous morphology, stable fluorescence, high brightness, controllable doping, long lifetime, and nonlinear photo-response. However, it remains challenging for some sub-fields by fully characterizing UCNPs and consequently realize the advanced applications based on their unique properties, such as the imaging resolution, the weak optical force of single UCNPs, and scattering/fluorescence strength modulation. In this thesis, we aim to implement the projects based on the challenges. In this chapter, I will briefly introduce fluorescent upconversion materials and the biophotonics technologies used in this thesis.

1.1 Fluorescent upconversion materials

Fluorescent upconversion materials as probes have been widely used to investigate biological imaging [1][2], sensing [3][4], therapies [5][6], photocatalysis [7] and photovoltaics [8]. Upconversion material could convert the low-energy light to high-energy light, enabling a super-high signal-to-background ratio. There are several kinds of upconversion materials based on the upconversion mechanisms, such as two-photon upconversion, inorganic lanthanide ion-doped nanoparticles, and molecular triplet-fusion-based upconversion. This thesis only focuses on the latter two types.

1.1.1 **Lanthanide-doped upconversion nanoparticles**

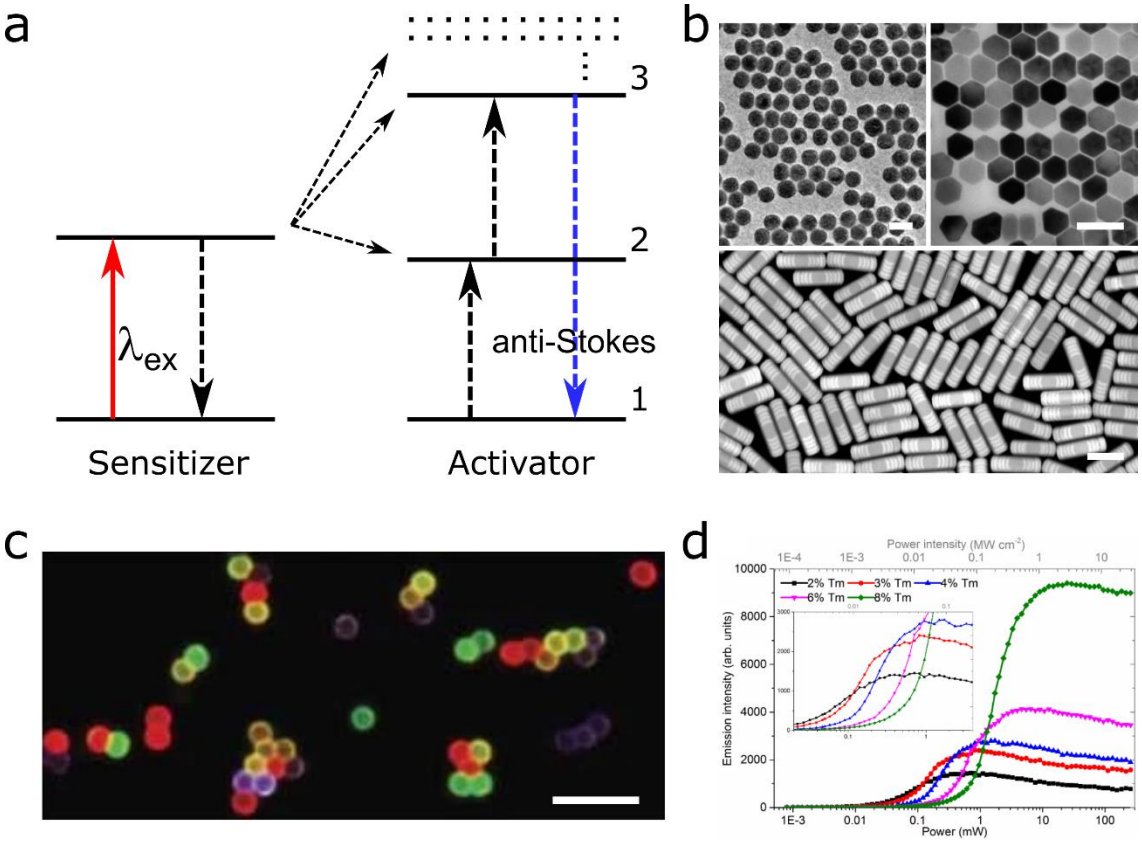

Figure 1-1. UCNP and its properties. (**a**) Schematic of energy transfer for UCNP. (**b**) Transmission electron microscopy (TEM) images of $NaYF_4$ (upper) and high-angle annular dark-field scanning transmission electron microscopy (HAADF-STEM) image of 18-segment heterogeneous nanorods. Scale bar is 100 nm. (**c**) Luminescence micrograph of polystyrene beads tagged with $NaGdF_4$:Yb,Tm@$NaGdF_4$ (blue), $NaGdF_4$:Yb,Tm@$NaGdF_4$:Tb (green), $NaGdF_4$:Yb,Tm@$NaGdF_4$:Eu (red), and a binary mixture of $NaGdF_4$:Yb,Tm@$NaGdF_4$:Tb and $NaGdF_4$:Yb,Tm@$NaGdF_4$:Eu (yellow), respectively. Scale bar is 10 μm. (**d**) Power-dependent 800 nm-emission from a single UCNP with different Tm^{3+} doping concentration ($NaYF_4$:20% Yb^{3+}, x% Tm^{3+} nanoparticles, x=2, 3, 4, 6 and 8) under 980 nm excitation. Panels b, c and d adapted with permission from refs. [9], [10], [11] and [12], respectively; Copyright 2006 American Chemical Society; Copyright 2020 Springer Nature; Copyright 2011 Springer Nature; Copyright 2018 Springer Nature.

For nearly twelve years, lanthanide-doped nanoparticles (Ln-NPs, same as UCNPs) have attracted extreme attention due to their unique properties and resultant broad applications [13][14]. This kind of nanoparticle is composed of a crystal host, i.e., $NaYF_4$ and $LiYF_4$, with embedded hundreds of thousands of trivalent lanthanide ions. These lanthanide ions play two roles in the host structure, some lanthanide ions, e.g., Yb^{3+}, serves as the sensitizer for absorbing photons, while others, e.g., Er^{3+}, Tm^{3+}, provide multiple energy levels to receive the photons from the excited sensitizer. After experiencing complex energy transfer processes, the anti-Stokes fluorescence will be produced (**Figure 1-1a**).

Because of the multiple electron energy levels and integrated-flexible nanostructures, lanthanide-doped nanoparticles have many merits for exploring their internal nature and applications, such as the super-high fluorescence brightness and super-long photostability. Here, we only show the following three merits of UCNPs which are closely related to my PhD work, while other merits, such as the tunable lifetime, can be found in many references [15][11][16].

(1) **Controllable synthesis for doping and morphology.** Because of the highly programmable crystal host of YF_4^-, other kinds of lanthanide ions can substitute Y^{3+} easily in the host structure, of which concentration can be even controlled very precise. Therefore, many types of lanthanide-doped nanoparticles can be synthesized with a designed concentration [10][17][18]. In addition to the precise control for doping types and concentration, the morphology of UCNPs is also controlled by adjusting the synthesis conditions. **Figure 1-1b** shows the homogeneous structures of UCNPs, which can be nanosphere, nano-hexagonal, nanorod and nano-dumbbell [10][9][17] and so on. The controllable doping and morphology provide the possibility to investigate the properties of a single UCNP nanoparticle. My PhD projects displayed in Chapters 2, 3, and 4 are the investigation of single UCNPs, which are based on controllable synthesis.

(2) **Tunable emission spectrum.** One of the most attractable properties of UCNPs is the abundant emission spectra enabling display applications (**Figure 1-1c**) [11]. The multiple energy levels of lanthanide ions provide the chance of energy transfer from the excited intermediate state to the ground state, accompanied by energy cross-relaxation, non-radiation and photon avalanche [1][19][20]. This brings rich emissions with different wavelengths. We can obtain UCNPs with different colours by changing the dopant types and concentration [11], as well as the excitation wavelength and power [21]. Therefore, UCNPs are the ideal nanomaterials for display and imaging. This tunable emission spectrum is leveraged in Chapters 2 and 4 for resolution improvement and particle recognition, respectively.

(3) **Tunable fluorescence nonlinearity**. This property results from the absorption and emission of the multi-photons energy transferring process since the sensitizers transfer the absorbed photons to the activators. The energy transfers between multiple energy levels and produces the emission with different responses, such as two-photon fluorescence, three-photon fluorescence, and four-photon fluorescence. Under a certain

excitation power, one kind of response is predominant while others can be neglected. The response varies with the excitation powers, resulting in fluorescence nonlinearity (**Figure 1-1d**) [12]. This nonlinear response is always called the power-dependent curve of excitation and emission. Tm-doped UCNP is a widely studied example [22][12][23][19]. We can adjust the nonlinearity by controlling the doping concentration of Tm^{3+}. This nonlinear nature of UCNPs provides the chance to improve the resolution by conventional confocal microscopy in Chapter 2.

In a word, the programmable synthesis of UCNPs for doping (e.g., types and concentration) and morphology guarantees the individual but stable property of single nanoparticles, while the abundant electron energy levels for energy transfer provide the chance to engineer the performance on the single-nanoparticle level. Based on this, I investigate the fluorescence nonlinearity of Tm-doped UCNPs for upgrading the nanoscopy (Chapter 2), take advantage of the engineerable point spread function (PSF) for improving the optical force sensitivity (Chapter 3), and leverage the resonance effect for modulating the Rayleigh scattering at the nanoscale (Chapter 4).

1.1.2 **Triple-fusion-based upconversion materials**

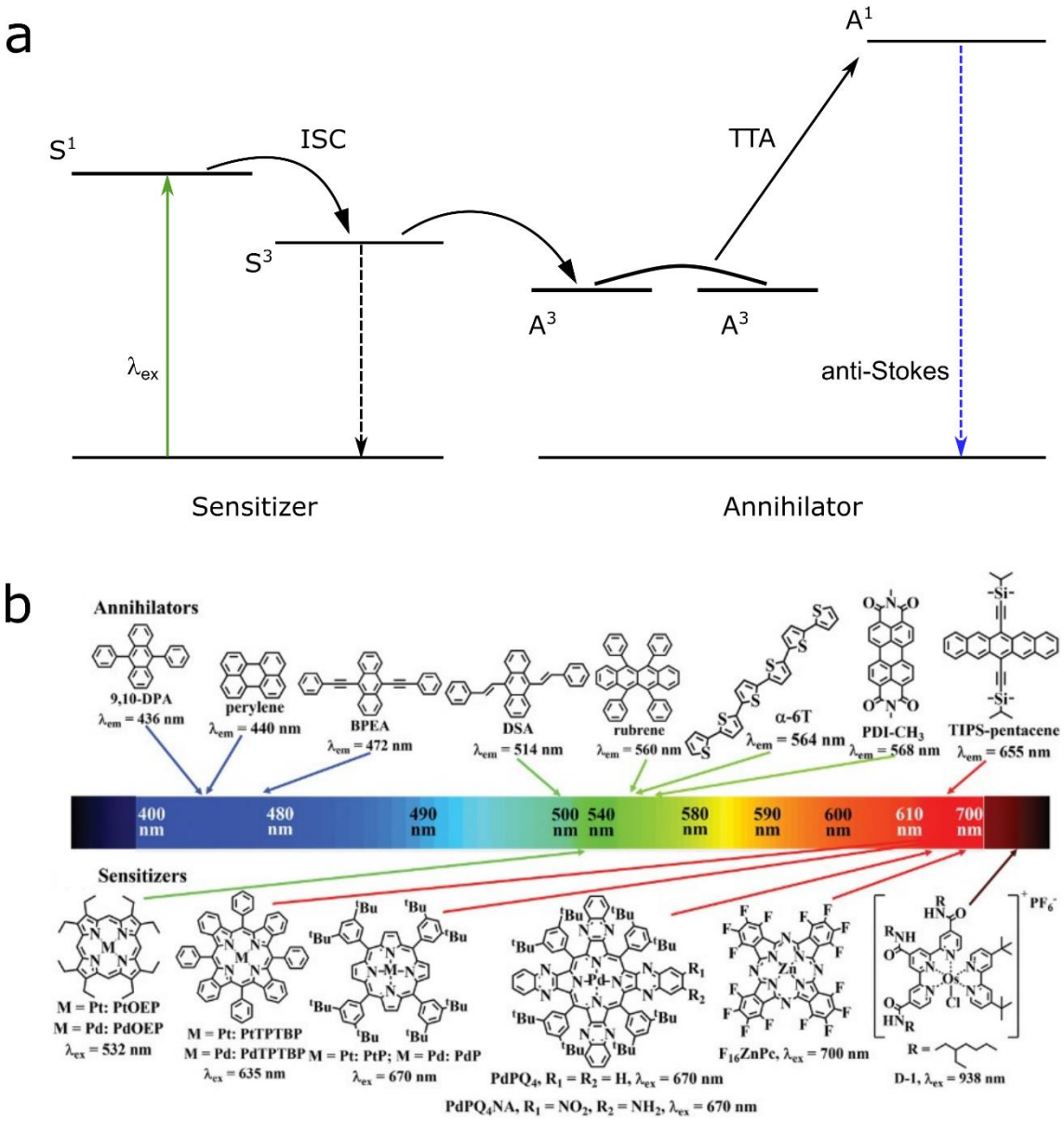

Figure 1-2. TTA and conventional TTA dyads. (**a**) Mechanism of energy transfer between sensitizer and annihilator. Superscript 3 denotes molecule with triplet, whole superscript 1 means molecule with singlet state. (**b**) Commonly used annihilators and sensitizers for a wide range of absorption and emission. Panel b adapted with permission from ref. [24]. Copyright 2021 Wiley-VCH.

Triplet-fusion-based material is another popular upconversion example. Triplet-fusion-based upconversion is also called triplet-triplet annihilation (TTA). This kind of upconversion process underlies molecular energy transfer. Triplet-fusion-based upconversion contains two separate components, molecular sensitizer and annihilator. **Figure 1-2a** shows the mechanism of TTA. Sensitizer molecules are generally excited by

the long-wavelength light to the active ones with singlet energy. After a quick electron spin-flip, namely intersystem crossing (ISC), the sensitizer with singlet energy will turn into one with triplet energy. The molecule with a triplet state always has a long lifetime (from nanosecond to millisecond level), providing enough time to diffuse and transfer energy between the molecules with matchable energy levels. Usually, the annihilator molecules on the ground state are easily activated by the triplet-state sensitizer to the ones with the triplet state. Under the oxygenated environment, oxygen molecules are much easier than annihilators to be excited by the triplet-state sensitizers, which is called oxygen quenching [25][26]. In the triplet-fusion-based upconversion system, two annihilator molecules with triplet energy collide and then produce the anti-Stokes fluorescence, which is regarded as the triplet-triplet annihilation process. From the mechanism, we can know TTA upconversion is a diffusion-controlled process. Therefore, any external perturbation for the diffusion process will influence the TTA performance, which can be designed for stimulated sensors [27]. For TTA-based upconversion, the most appealing advantage is the flexible and programmable platforms by constructing the sensitizer-annihilator pair. For conventional TTA systems, both the sensitizer and annihilator are organic molecules [24], while the absorption light and anti-Stokes fluorescence range from the near-infrared region to the ultraviolet region (**Figure 1-2b**). In recent ten years, more and more novel sensitizers have been exploited, such as quantum dots [26], perovskite particles [28], and lanthanide-doped nanoparticles [29]. These novel sensitizers propel the development of TTA systems, as they provide more freedom to design target-oriented platforms and study the novel mechanism of energy transfer. In my PhD work, I focus on developing aqueous TTA systems by avoiding organic solutions, meanwhile, I try to work out oxygen quenching, one of the most challenges for TTA upconversion.

1.2 Biophotonics technologies

The advances in upconversion materials boost the emerging biophotonics technologies for characterization. Here I mainly introduce the technologies related to my PhD work.

1.2.1 Super-resolution microscopy

To observe and understand microscopic objects is always the dream of humans. Over the centuries, scientists have been devoted to developing optical technologies to explore the

microscopic world [30][31]. With loads of effort, the resolution of technologies is improved to the limitation, named Abbe diffraction limit[32]. This limit is applied to both optical microscopy and electron microscopy, and here I just claim for optical technologies. The diffraction limit is determined by the light wavelength and the numerical aperture (NA), which is related to the refractive index and the collecting angle of the lens. For two adjacent spots, the resolution is $x = \frac{0.61\,\lambda}{\mathrm{NA}}$ [33]. **Figure 1-3a** shows the scheme that, within the Rayleigh Criterion, the two (adjacent) point sources observed in the microscope can be resolved, otherwise it is out of the resolution capacity.

To break the diffraction limit, many methods have been explored. They can be classified into three strategies.

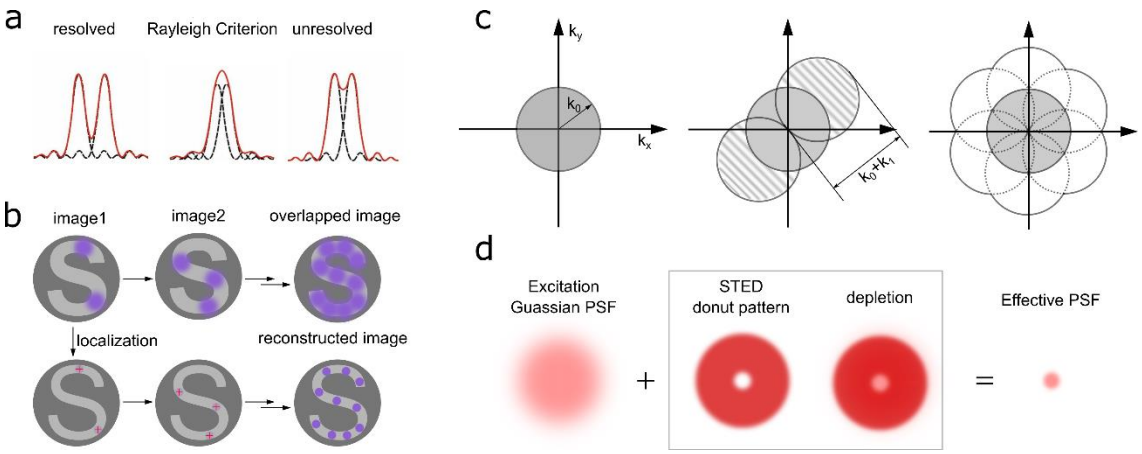

Figure 1-3. Super-resolution mechanisms. (**a**) Rayleigh criterion for resolving ability. (b) Single-molecule localization mechanism. (**c**) Structured light mechanism. (**d**) PSF engineering for super-resolution microscopy.

1) **Single-molecule localization.** For this strategy, the representative examples are stochastic optical reconstruction microscopy (STORM) [34][35][36][37] and photoactivated localization microscopy (PALM) [38][39][40][41]. The key point is using photo-switchable molecules to realize the on-state and off-state under different excitation wavelengths. **Figure 1-3b** depicts the scheme of the mechanism. The target needs to be first labelled with the photo-switchable molecules. Under the excitation, several molecules can be excited with on-state, which is recorded as an image. The distribution of the individual bright molecules obeys the Gaussian function [42]. Therefore, the localization of these molecules can be determined according to Gaussian fitting. This process needs to be repeated hundreds of thousands of times under the excitation

switching on and off. The reconstruction of loads of raw images will finally give the super-resolved image of the target. This strategy is widely applied in biological imaging. However, the requirements of stable but switchable molecules and complex data processing, as well as the mass of data to deal with, restrict the effectiveness of this strategy.

2) **Structured light.** A typical example is structured illumination microscopy (SIM) [43], which breaks the diffraction limit via modulating the scanning illumination patterns. In Fourier space, the higher frequency, away from the centre, represents more detailed information, and vice versa. Within the diffraction limit, the observed region via the microscope can be regarded as a circle, of which the radius is proportional to the numerical aperture and the inverse of the wavelength (**Figure 1-3c**). This causes the loss of high-frequency information outside the circle through imaging, resulting in low resolution of the target. If using the illumination with a simple sinusoidal intensity pattern corresponding to three frequency points (**Figure 1-3c**), the observed region can be extended along the angle of the pattern, just like the previous circle translate to a k_0 distance from the origin. This can shift the high-frequency information outside the circle into the circle and become effectively observable as moiré fringes (**Figure 1-3c**). The next step is separating the extra information from the mixture with the normal resolution information via solving a set of linear equations from enough raw images. Each raw image is recorded under the same excitation pattern but with a different phase. The lateral resolution can be enhanced only along the line perpendicular to the excitation pattern stripes (**Figure 1-3c**). Another two angles equally spaced by 60° are rotated and acquired for achieving isotropic resolution. All the components available from all pattern orientations (the seven circles in **Figure 1-3c**) are then "stitched" back together according to their original positions in frequency space, forming a final reconstructed image with extended resolution. Compared to other super-resolution technologies, SIM performs well in single living cell imaging[44], and recently also works well for deep tissue imaging by using UCNP[45].

3) **PSF engineering**. The representative example is stimulated emission depletion (STED) microscopy [46][47]. In general, the target under the Gaussian excitation will produce a Gaussian-like PSF. During STED microscopy, two lasers are simultaneously used. Gaussian-shaped excitation illuminating the target generates a bigger PSF, while the

depletion excitation with a doughnut-shaped pattern will suppress the emission within the doughnut region, just leaving the smaller bright central region. The resultant smaller PSF stands for higher resolution (**Figure 1-3d**). By engineering the PSF with two lasers, we can break the diffraction limit easily.

Super-resolution microscopes based on the above mechanisms make it possible to observe the microscopic world by breaking the optical diffraction limit. To do so, another key point is the selection of fluorescent probes. The typical and most widely used are fluorescent dyes[48][35][38][42]. The small molecules make them easy to label cellular membranes, organelles and biological tissues via endogenous gene expression, as well as the high fluorescence efficiency. However, the drawbacks of photobleaching and instability pose challenges for these super-resolution microscopes, in particular, the microscopes need a long time to scan and record images. Lanthanide-doped nanoparticles with the merits of super-high brightness and long-time photostability become the ideal choice for many kinds of super-resolution microscopes.

1.2.2 **Optical tweezers**

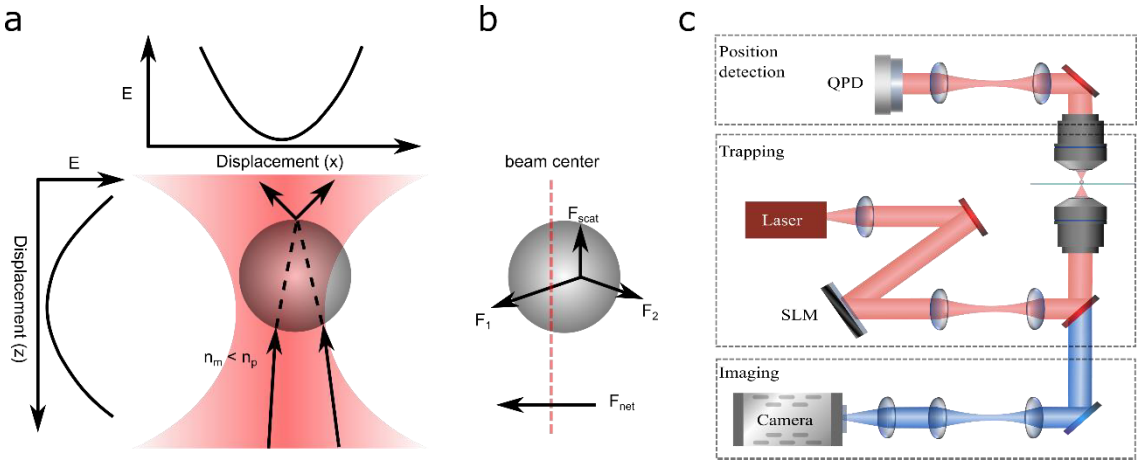

Figure 1-4. Optical tweezers. (a) Schematic of laser potential wells in x and z directions and trapped particle. Upper and left are the potential energy along the distance. (b) Force balance of trapped particle in the potential well. (c) Typical setup of optical tweezers.

Optical tweezers are a powerful tool to isolate and characterize single nanoparticles by optically trapping, manipulating and rotating [49]. The particle trapped within the potential well produced by the laser will be subject to two forces, scattering force and gradient force (gravity force can be neglected as the mass of the nanoparticle is super

tiny) (**Figure 1-4a**). The scattering force pushes the particle away from the centre of the potential well and moves in the direction in which the light propagates. The gradient force attracts the particle back to the centre. Under the balance of scattering and gradient force, the particle can be trapped at the place where the light is strongest. At the trapped position, the particle moves in Brownian motion. This property enables optical tweezers to be super sensitive to external stimulation, such as external force and refractive index of the surrounding medium and particle itself. Typically, the setup of optical tweezers contains three parts: the trapping part, position detection part and imaging part (**Figure 1-4b**). In the trapping part, the delicate optical path is designed for controlling the laser pattern and manipulating the particles. A spatial light modulator (SLM) is always utilized to form a trapping laser with a customer-designed pattern for manipulating single/multiple particles by rotating or translating. In the position detection part, the quadrant photodiode detector (QPD) is used to record the position shift due to Brownian motion by collecting the scattering signal from the trapped particle. This method to measure optical force is also named the QPD method [49]. In the imaging part, a camera (CCD or CMOS) is used to observe the wide-filed image or the fluorescence image for some fluorescent probes. This part can be designed and optimized for another method to measure the optical force of fluorescent particles, which is called the digital video microscopy method [50].

The challenge for present optical tweezers is trapping nanoscale particles, especially the nanoparticles with low refractive index, due to the weak optical force resulting from the similar refractive index of the particle with the surrounding medium. Besides, it also remains challenging to measure three-dimensional (3D) force as the two methods aforementioned are more effective for measuring the lateral force. In my PhD work, we developed a novel method for detecting 3D optical force and pushed the force sensitivity to attoNewton (aN) level based on the unique properties of UCNPs.

1.2.3 **Interferometric scattering microscopy**

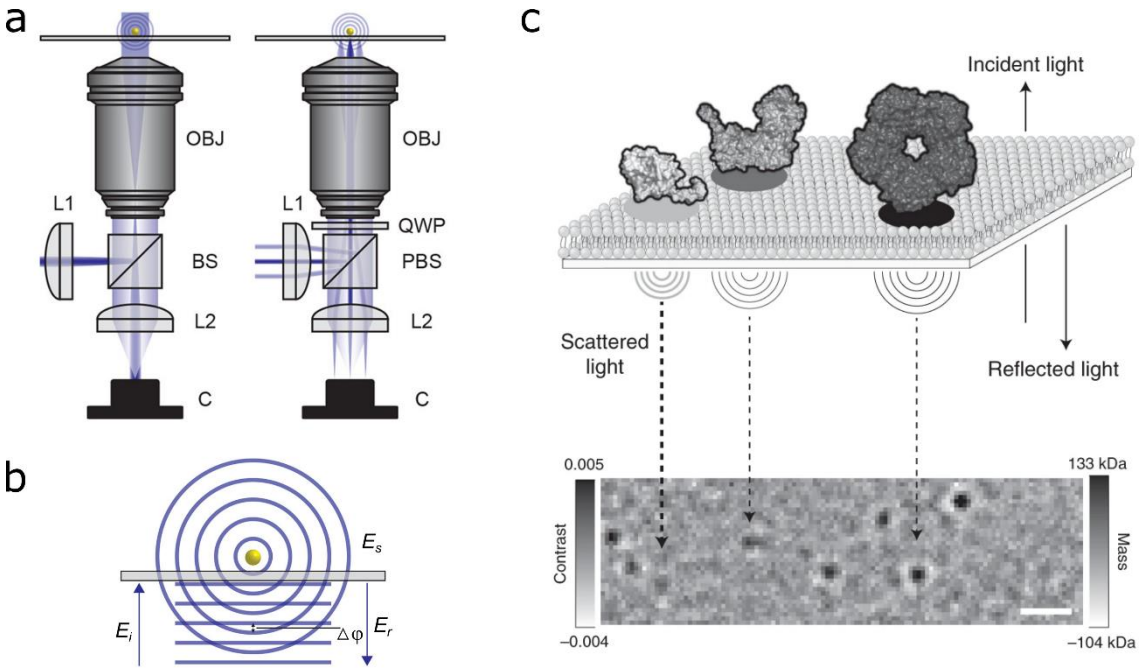

Figure 1-5. iSCAT microscopy. (a) Schematic of widefield illumination iSCAT (left) and rapid beam scanning illumination iSCAT (right). OBJ, objective; L1 and L2, lens; BS, beamsplitter; PBS, polarized beamsplitter; QWP, quarter-wave plate. (b) Schematic of the interference signal, *Ei* incident field, *Es* scattered field, *Er* reflected reference field, Δφ phase difference between the scattered and reflected fields. (c) Wide applications of iSCAT microscopy in protein imaging. Panels adapted with permission from refs. [51] for a and b, and [52] for c; Copyright 2021 American Chemical Society; Copyright 2021 Springer Nature.

Interferometric scattering (iSCAT) microscopy[53] shows outstanding performance in detecting the Raleigh scattering of nanoscale particles compared with other technologies, such as dark-field microscopy [51]. It was reported firstly by Sandoghdar's group that the 10 nm gold nanoparticle was imaged clearly [53]. Since then, iSCAT microscopy has been widely used to image and track the protein molecules on the cell membrane [54][52][55]. Relatively, iSCAT microscopy has a simple setup (**Figure 1-5a**). The laser light gets through the objective and arrives at the cover glass, which produces the reflect light. The reflected light and the scattering light from the nanoparticles will be collected by the same objective and produce the interference signal on the camera (**Figure 1-5b**). The iSCAT image is thus recorded by the camera. iSCAT microscopy mainly provides two advantages, super-fast detection and super-high sensitivity for scattering. The intense scattering signal makes iSCAT microscopy super high detection speed, which can be as high as 66000 frames per second (fps) [54].

Generally, the scattering strength is proportional to the scattering cross-section. According to the Rayleigh approximation [56], the scattering cross-section can be expressed by,

$$\sigma_{scat} = \frac{8}{3\pi^2}|\alpha|^2\lambda^{-4} \qquad (1-1)$$

here, λ is the laser wavelength and α is the polarizability of nanoparticle. The polarizability can be calculated as,

$$\alpha = 3\varepsilon_m V \frac{\varepsilon_p - \varepsilon_m}{\varepsilon_p + 2\varepsilon_m} \qquad (1-2)$$

where V is the volume of nanoparticle, ε_p and ε_m are the permittivity of the particle and the surrounding medium.

According to equations (1-1) and (1-2), we can know that the scattering cross-section is proportional to the volume of the nanoparticle.

In iSCAT image, the detected intensity (I_d) of the nanoparticles is the interference between the reflected beam and the scattered beam. It can be expressed as,

$$I_d = I_r + I_s + 2\sqrt{I_r I_s}cos\varphi \qquad (1-3)$$

where φ is the phase difference between I_r (reflection intensity) and I_s (scattering intensity), consisting of the Gouy phase accumulation, particle-induced phase change and the particle's axial position induced phase change. For the nanoscale particle, the scattering strength can be neglected because it is very weak. So the contrast of nanoparticle in iSCAT image is,

$$C = \frac{I_{det} - I_r}{I_r} \approx \frac{2\sqrt{I_r I_s}}{I_r}cos\varphi = 2\sqrt{\frac{I_s}{I_r}}cos\varphi \qquad (1-4)$$

The scattering strength of nanoparticle is proportional to its scattering cross-section and consequently the square of the polarizability, $I_s \propto \sigma_{scat} \propto \alpha^2$. Therefore, we can know the scattering strength in iSCAT image can be derived from the contrast, which is proportional to the square root of the volume of the nanoparticle ($C \propto \sqrt{I_s} \propto |\alpha| \propto V$) for a certain phase (e.g., $cos\varphi = -1$). It means that the iSCAT signal representing the scattering strength of the particle will not decrease as much as the conventional images

when the diameter of the particle decreases. So it is suitable to detect super-tiny scattering for nanoscale particles.

The unique advantages of iSCAT microscopy, super-high sensitivity and speed, make it popular technology to study the dynamic processes from protein-protein interactions (**Figure 1-5c**) [52][55] to the photogenerated carrier [57]. In my PhD work, we use iSCAT microscopy to detect the Rayleigh scattering from resonance-enhanced lanthanide-doped nanoparticles because of its super-high sensitivity. For iSCAT microscopy, it remains challenging to distinguish different types of nanoparticles in the iSCAT image, as the signal is the same and incapable of distinction. Based on the fluorescence and scattering properties of UCNPs, we modify the configuration and realize the multiplexed iSCAT microscopy for living cells.

1.3 Challenges to work out in the thesis

The merits of upconversion materials, especially UCNPs, e.g., well-organized individual, stable fluorescence, high brightness and the abundant energy levels of doped lanthanide ions, provide the wonderful platforms in many applications of imaging, sensing and photocatalysis. However, the potential of this nanoprobe is not limited to these reported applications. For some hot and emerging applications, this nanoprobe also can show its magic power when facing the present challenges of these sub-fields. (1) **Imaging.** The enhancement of resolution are always based on the complicated optical setups and redundant data processing. (2) **Force sensitivity.** It remains challenging to measure 3D super-sensitive optical force in aqeous solutions due to the weak trapping force of nanoparticle. (3) **Scattering modulation.** The current methods to engineer scattering features of nanoparticles limit to morphology controlling, which complicates the fabrication process. (4) **Oxygen resistance of molecular upconversion.** Molecular upconversion process is always destroyed by oxygen molecules in the environment. For these challenges, we can perfectly take advantage of the nature of upconversion materials to improve the present situation and obtain better performance. Therefore, by employing the optical technologies mentioned above, multiple goals and characterization of upconversion materials are expected.

1.4 Organization of the thesis

In the thesis, based on the properties of upconversion materials characterized by several biophotonics technologies, I will achieve the following four goals: (1) upgrade the nanoscopy by exploiting the nonlinear fluorescence of UCNPs; (2) improve the 3D optical force sensitivity using optical tweezers; (3) modulate the Rayleigh scattering of UCNPs immune to morphology; and (4) develop new organic molecule-based upconversion probe. According to the four goals, the thesis is constructed as follows except the Introduction (Chapter 1) and Conclusion and Outlook (Chapter 6).

Chapter 2 develops a stepwise strategy to upgrade the resolution. We extract the fluorescence nonlinearity using a stepwise strategy from *M* raw confocal images obtained under different excitation powers. Finally, we realize the resolution enhancement by $\sqrt{M}$ fold from *M* steps compared with the raw confocal image. This chapter demonstrates the possibility of further upgrading the resolution by a simple strategy instead of complex and expensive super-resolution setups and data post-processing.

Chapter 3 improves the sensitivity of optical force to attoNewton (aN) level. We first develop the method for measuring 3D force from optically trapped UNCP by combing optical astigmatism and deep learning. We then realize the force sensitivity up to 600 aN by analysing the position possibilities of a single trapped UCNP. This chapter provides an effective solution for measuring the trap stiffness of low-refractive-index nanoparticles, enabling single-molecule level force sensing.

Chapter 4 modulates Rayleigh scattering of UCNP based on the resonance effect originating from the lanthanide ions dopants. The resonance enhancement under the matching excitation wavelength results in the improvement of Rayleigh scattering strength, which is detected by iSCAT microscopy. Conceptually, we also develop multiplexed iSCAT microscopy to distinguish nanoparticles in living HeLa cells. The chapter provides an alternative strategy to engineer the scattering features immune to the geometry of nanoparticles.

Chapter 5 explores the molecule-based upconversion probe. In this chapter, we develop a simple strategy to realize aqueous TTA upconversion by controlling the ionic equilibrium of the TTA dyad. We find that the ionized organic dyad in physiological buffers and electrolyte-based media show natural aerotolerance without any complicated

structure engineering. We also demonstrate the potential of this TTA system as reversible pH and sensitive temperature sensors. This chapter can inspire the development of aqueous TTA for practical applications.

Chapter 2 Upgrade the nanoscopy by leveraging the tunable fluorescence nonlinearity of UCNPs

The nonlinear response of fluorescent probes can generate higher spatial frequency information beyond the diffraction limit of the optical systems. Most current nonlinearity-based strategies for improving resolution depend on either complicated illumination modulation or appropriate excitation power. In this chapter, we put forward a simple but efficient strategy that upgrades the resolution via tuning the fluorescence nonlinearity of single UCNPs. We develop a stepwise algorithm based on a series of confocal images (i.e., M images) of single UCNPs acquired under the gradient continuous-wavelength excitation within the superlinear regimes. The spatially encoded variations of M raw fluorescence images resulting from the nonlinearity can theoretically enable $\sqrt{M}$-fold higher resolution than that of the original sub-diffraction images. We experimentally achieve the resolution with 1.7-fold ($\sim\sqrt{3}$) beyond the diffraction limit by resolving two adjacent single nanoparticles. This strategy provides a novel dimensional insight to upgrading the resolution, immune to expensive setups and complex data processing.

Part content of this chapter is from the paper:

C. Chen†, **L. Ding†** (co-first), B. Liu, F. Wang*. Exploiting The Tunable Nonlinearity in Upconversion Nanoparticles for Super-resolution Imaging. (*under review*)

2.1 Nonlinearity based super-resolution microscopy

Investigation for nanoscale objects and even single molecules within the optical diffraction limit requires higher resolution of microscopy technologies. There are mainly two directions for improving the resolution, one is developing advanced optical techniques including modulation of the excitation pattern [58], and the other is looking for powerful nanomaterials with unique properties, such as nonlinear fluorescence [59][60]. In this chapter we are devoted to the latter one, upgrading the resolution by leveraging the property of lanthanide-doped UCNPs.

Regulating the transition of fluorescent probes from the ground to the excited states via excitation power can generate nonlinear fluorescence [61]. The patterned light excitation, such as fringes [62][63] and speckles [64][65], induced from the nonlinear techniques can be used to enhance the resolution since it contains the spatial frequency information from higher-order harmonics in the Fourier transformation. Excitation intensity can also be harmonically modulated for sub-diffraction imaging on a saturation excitation (SAX) microscopy [66] with confocal configurations. Nonetheless, complex illumination modulation is required to extract the buried higher spatial information from the nonlinear response.

A more direct method that utilizes the excitation power corresponding to the steepest slope (namely superlinear regime) of the power-dependent curve has been developed on conventional confocal microscopy[19][23][67]. The superlinear regime generates spatial modulations resulting in a better spatial resolution. However, complicated modulation of fluorescence intensities was required to obtain the superlinear operation for nanodiamonds [59], while a triple excitation process under sufficient excitation power is essential for quantum dots [60]. By contrast, lanthanide-doped UCNPs become outstanding due to the simple illumination source and low excitation power for achieving superlinearity [23][67].

The superlinearity of the power-dependent curve of UCNPs comes from the multiple intermediate energy states, which enable photon transfer and cross-relaxation [1][20]. This nonlinear optical response and saturation properties have been reported for sub-diffraction imaging technologies [20][1][68]. Recently, the excitation within the superlinear regime was reported to arouse the photon avalanche effect in a single UCNP, achieving the 26^{th} power of pump intensity scaling with the emission and obtaining a sub-70 nm spatial resolution [19]. In this case, the giant nonlinear optical responses from photon-avalanching nanoparticles necessitate a rather long rising time (hundreds of milliseconds per pixel), which challenges the dynamic imaging applications.

A further solution for a better spatial resolution would be the nonlinear tunability under differential excitation power, which could generate a programmable spatial resolution. Dynamic saturation optical microscopy has demonstrated that higher spatial information can be extracted from the dynamic PSF with variations [69]. Similarly, the STED microscopy also proved the resolution enhancement by modulating the PSF with the

depletion power [58]. However, these modulations need the entire saturation curve of all the pixels at the expense of the overall data collection time [70]. Alternatively, photobleaching imprinting microscopy [71] and stepwise optical saturation microscopy [72] indicate that two or three images with differential saturating degrees are sufficient for a substantial resolution improvement by connecting the corresponding high-order nonlinearity information with the illumination fluence distribution.

In this chapter, we upgrade the resolution of single UCNPs by differentiating the excitation intensity within the superlinear regime of the power-dependent curve. Within this region, small excitation changes will generate substantial emission variations for developing the stepwise algorithm. We first obtain the spatial information encoded raw confocal images under the gradient continuous-wavelength excitation and then decode the buried spatial information by a stepwise algorithm for resolving two adjacent single nanoparticles. This allows an efficient nonlinearity-based method to improve the super-resolution which avoids using complex optical setups and data processing.

2.2 Methods

2.2.1 Super-resolution microscopy system

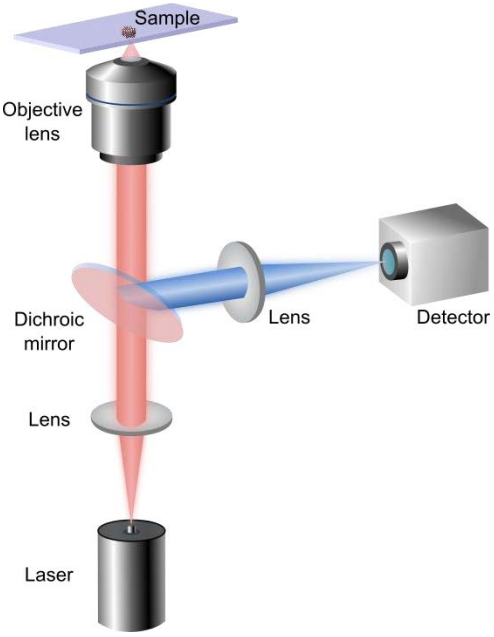

Figure 2-1. Setup of confocal microscopy used in this chapter.

We conduct the experiments and data acquisitions using a typical conventional confocal configuration, as shown in **Figure 2-1**. The 980 nm laser (Thorlabs, BL976-PAG900) gets through the short-pass dichroic mirror (DM1, T875spxrxt-UF1, Chroma) and focuses on the nanoparticles via the objective lens (Olympus, 100x, 1.40 oil). The emission from UCNPs will be collected by the same objective and recorded on an sCMOS after a bandpass filter (BPF, FF01-448/20-25, Semrock) and a tube lens. The laser power is controlled by the half-wave plate and a polarized beam splitter placed before the laser. The confocal images are collected by scanning the nanopiezostage (PI, P-545.3C8H) and the photon counts are recorded by a single-photon avalanche diode (SPAD). All the optical components will be controlled by the homemade LabView programs. All powers are measured at the objective lens's rear aperture. Pixel dwell times are set to 1 millisecond.

2.2.2 **Synthesis of UCNPs**

UCNPs are synthesized according to a typical procedure, which is described in detail in chapter 4.

2.3 Theory and simulation

2.3.1 **Tunable fluorescent nonlinearity**

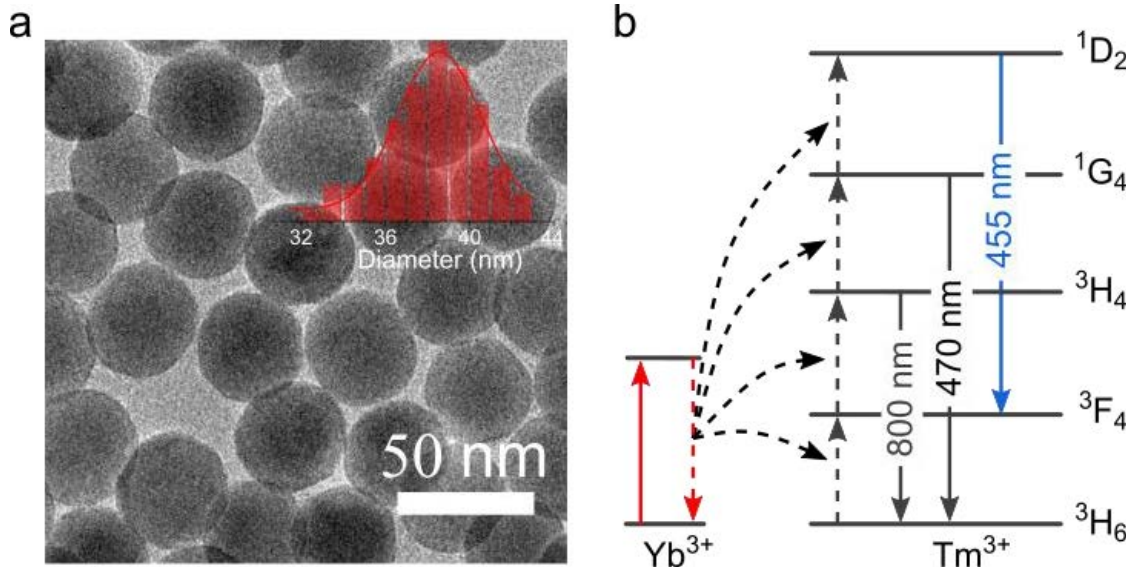

Figure 2-2. Morphology and energy transfer. TEM (**a**) and simplified energy level and upconversion process (**b**) of the nanoparticles $NaYF_4$: 40% Yb^{3+}, 4% Tm^{3+} under 980 nm continuous-wave excitation.

To demonstrate the tunability of the nonlinear optical responses from single UCNPs, we employ a $NaYF_4$ nanocrystal host co-doped with high concentrations of 40% Yb^{3+} sensitizer ions and 4% Tm^{3+} activators ions. The homogeneous structures are displayed in **Figure 2-2(a)**, and the diameter is around 38.5 nm. Under the excitation of 980 nm, the sensitized photons on Yb^{3+} ions stepwise transfer to the energy levels of Tm^{3+} emitters. The population of photons on different energy levels is affected by the multiple long-lived intermediates and metastable electronic levels (**Figure 2-2(b)**). The nonlinear upconversion emission is generated after complex processes, such as dissipation, excited-state absorption, photon avalanche and cross-relaxation. Emission from different excited energy levels can be used to predict the number of multiplexed photons for determining the excitation power within the superlinear regime.

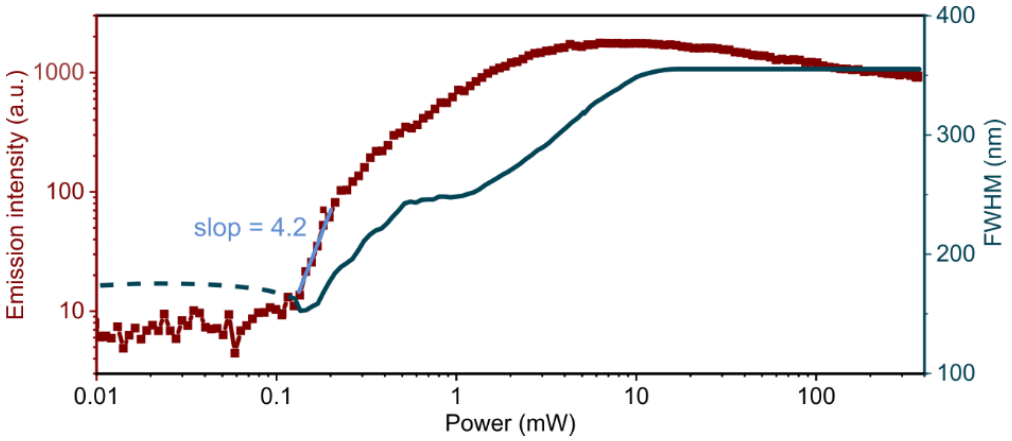

Figure 2-3. The power-dependent curve (red dot) using the $NaYF_4$: 40% Yb^{3+}, 4% Tm^{3+} and 455 bandpass filter. The superlinear regime locates where the curve with the largest slope. Corresponding simulated full width at half maximum (FWHM) of single nanoparticle images at 455 nm emissions function of excitation intensity (cyan line).

To obtain the superlinear regime, we collect the five-photon upconversion emission from a single 4% Tm-doped UCNP using the 455 nm bandpass filter (**Figure 2-3**). The weak emission signal is buried in the noise and background when the excitation power density is less than 0.1 mW, while it increases significantly when the excitation power locates between 0.1 and 0.3 mW. The steep curve with the largest slope response is resulted from the five-photon transmission (450 nm, $^1D_2 \rightarrow {}^3F_4$). The slope of the curve declines from the excitation power of 0.3 mW due to the dynamic saturation of photon carriers. Conventionally, this superlinear regime allows the best resolution of a single nanoparticle image on confocal configurations [19][67]. The improved resolution within the superlinear regime can be interpreted by the point spread functions of the emission, $\Delta r = \frac{\lambda}{2NA\sqrt{N}}$ [33], here λ is the emission wavelength, NA is the objective numerical aperture, and N is the number of relevant photons, e.g., nonlinearity. Obviously, the resolution is scaled inversely with the square root of the order of nonlinearity. The adjustment of the nonlinearity of UCNPs allows the full width at half maximum (FWHM) of the emission PSFs related to the excitation intensities (**Figure 2-3** cyan line). In particular, the resolution is affected significantly within the superlinear regime, up to sub-200 nm theoretically. It should be noted that the spatial resolution based on the superlinearity of UCNPs can reach sub-70 nm using a 1064 nm laser as the excitation source [19].

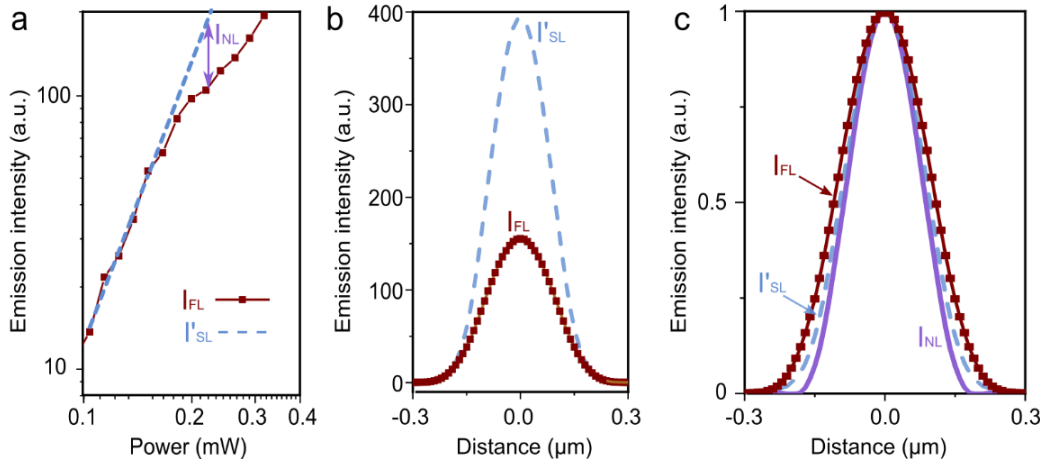

Figure 2-4. Extracting the higher-order nonlinear information. (a) Power-dependent curve of emission acquired under the gradient excitation powers. Dotted line represents the predicted emission according to the five-photon emission. (b) Comparison of super-linear and saturated emission distribution in the laser focus. (c) Extracting the nonlinear information provides a narrower PSF.

The resolution enhancement by the nonlinearity can be also explained by the PSF variations. Generally, the fluorescence nonlinearity of UCNPs is produced from the estimated linear fluorescence and the measured fluorescence intensities [73]. In our case, the nonlinearity is the difference between the 5-photon upconversion emission and the measured emission intensities (**Figure 2-4a**). This refers to the corresponding energy transfer from different energy levels, as the 5-photon emission is from $^{1}D_2 \rightarrow {}^{3}F_4$ while the measured emission results from the mixture of multiphoton transferring processes. Under the differential excitation, the measured PSF profiles will be reduced from the 5-photon emission PSF that would be achieved in the absence of any other photon transfer processes (**Figure 2-4b**). Therefore, the PSF based on the nonlinear component will be narrower, representing higher resolution (**Figure 2-4c**).

2.3.2 **Stepwise algorithm for UCNPs**

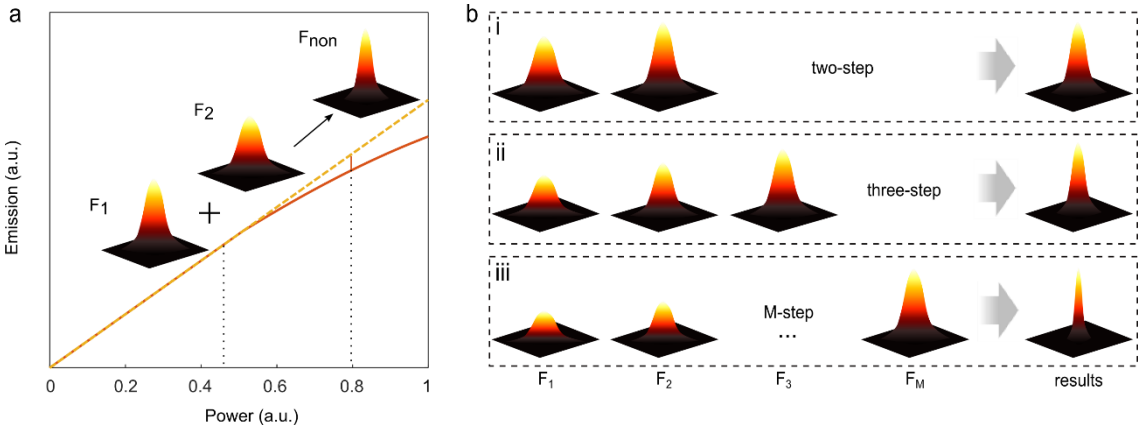

Figure 2-5. Schematic of the stepwise algorithm. (a) Scheme of the nonlinear power-dependent curve and three PSFs from raw images under three different excitation powers. (b) Sketch map of two-step (i), three-step (ii) and M-step (iii).

The stepwise algorithm is based on the combination of reasonable mathematic derivation and nonlinearity of UCNPs. The superlinear regime can be considered as weak saturation, so it means the slope of the power-dependent curve decreases gradually under gradient excitation powers. As shown in **Figure 2-5a**, we record the confocal image with a typical PSF shape (noted as F1) under the unsaturated power, while the second image with the corresponding PSF (noted as F2) under the weak saturated power. Via the mathematically linear combination of F1 and F2, we can finally obtain the nonlinear fluorescence intensity (F_{non}), denoting the difference between the real and the predicted intensities from the curve slope at the former power. This process is called Stepwise strategy and the rationality will be introduced in the 2.3.3 part. The nonlinear part from the stepwise algorithm has the narrower PSF, meaning high resolution. More than that, we can further shrink the PSF of the confocal image by recording three and even more images under gradient excitation power (**Figure 2-5b**). Theoretically, the steps can be infinite as long as the signal to noise is enough to distinguish.

2.3.3 **Mechanism**

We mathematically demonstrate the proposed concept to alleviate the frequency deficiency in the higher-order spatial information using the tunable superlinear emission responses in UCNPs. We simplify this dual-doped Yb^{3+}-Tm^{3+} ions system as a six-energy-level model and build rate equations to describe this model (**Figure 2-6**). It is

composed of two energy levels corresponding to the sensitizer Yb^{3+} and six energy levels corresponding to the activator Tm^{3+}. $^2F_{7/2}$ and $^2F_{5/2}$, $^3H_6$, $^3H_5/^3F_4$, $^3F_{2,3}/^3H_4$, $^1G_4$, and $^1D_2$ represented as s_1, s_2, 1, 2, 3, 4, 5 respectively. n_i is the population of photons on the energy level. c_i (i=1,2,3,4) is the energy transfer ratio between the excited level of Yb^{3+} on the ground and the intermediate levels of Tm^{3+}. k_{ij} is the cross-relaxation coefficient between the state i and j. a_{ij} is the branching ratio from energy level i to j. w_i is the intrinsic decay rate of Tm^{3+} on level i. P_{980} is the pumping rate of Yb^{3+}.

$$\frac{dn_1}{dt} = -c_1 n_1 n_{S2} + a_{21} w_1 n_2 + a_{31} w_2 n_3 + a_{41} w_3 n_4 + a_{51} w_4 n_5 - k_{31} n_1 n_3 - k_{41} n_1 n_4 - k_{51} n_1 n_5 \quad (2-1)$$

$$\frac{dn_2}{dt} = c_1 n_1 n_{S2} - c_2 n_2 n_{S2} - a_{21} w_1 n_2 + a_{32} w_2 n_3 + a_{42} w_3 n_4 + a_{52} w_4 n_5 + k_{41} n_1 n_4 + 2k_{31} n_1 n_3 \quad (2-2)$$

$$\frac{dn_3}{dt} = c_2 n_2 n_{S2} - c_3 n_3 n_{S2} - (a_{31} + a_{32}) w_2 n_3 + a_{43} w_3 n_4 + a_{53} w_4 n_5 + 2k_{51} n_5 n_1 + k_{41} n_4 n_1 - k_{31} n_3 n_1 \quad (2-3)$$

$$\frac{dn_4}{dt} = c_3 n_3 n_{S2} - c_4 n_4 n_{S2} - (a_{43} + a_{42} + a_{41}) w_3 n_4 + a_{54} w_4 n_5 - k_{41} n_1 n_4 \quad (2-4)$$

$$\frac{dn_5}{dt} = c_4 n_4 n_{S2} - (a_{54} + a_{53} + a_{52} + a_{51}) w_4 n_5 - k_{51} n_1 n_5 \quad (2-5)$$

$$\frac{dn_{S2}}{dt} = P_{980} n_{S1} - w_S n_{S2} - (c_1 n_1 + c_2 n_2 + c_3 n_3 + c_4 n_4) n_{S2} \quad (2-6)$$

To comprehend the slope of the emission curve in the superlinear region, five energy level rate equations with a nonlinear response excitation process were constructed. The parameters utilized in the full rate equations are listed in **Table 1-1**. Due to the greater obsecration cross-section of Yb^{3+} at 980 nm, the excitation photons are absorbed by Yb^{3+} solely and subsequently transferred to Tm^{3+} during the excitation process. According to the established rate equations, the ground state has the most populations of the carriers at the beginning. By transferring the pumping energy from Yb^{3+} to the ground state of Tm^{3+}, the new distribution of the carriers will be built starting from the ground state to the excited states of Tm^{3+} in order of energy levels. The photon upconversion process is a

sequential absorption process, with photon energy linearly absorbed by Yb^{3+} in the UCNPs. Rather than via a virtual intermediate excited state, the activator ions have multiple long-lived real intermediate states to facilitate multiphoton upconversion emission.

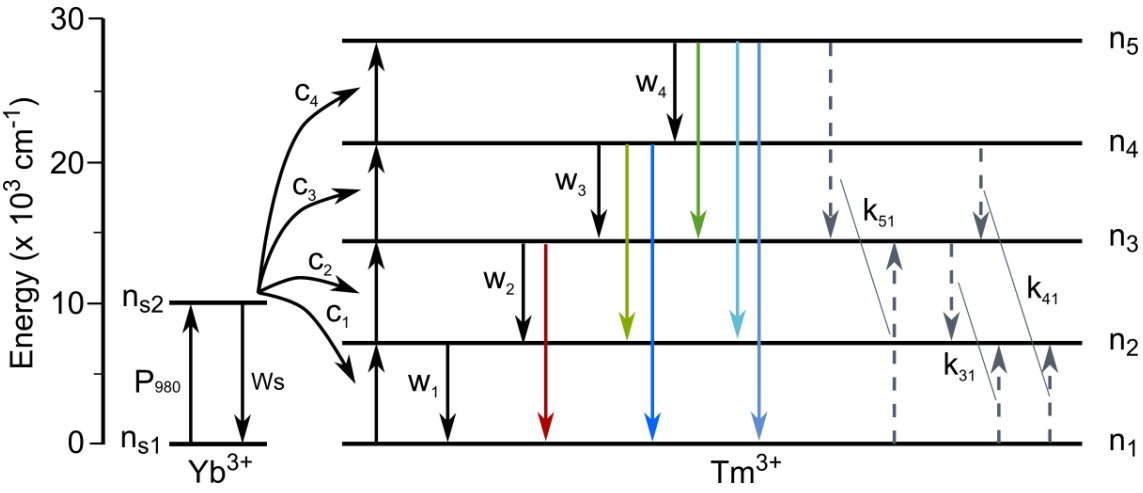

Figure 2-6. Simplified energy level diagram of Tm^{3+} and Yb^{3+} doped UCNP.

Table 2-1. Parameters in the internal transition.

Spontaneous radiation probability Tm and Yb				
w_4 (s^{-1})	w_3 (s^{-1})	w_2 (s^{-1})	w_1 (s^{-1})	w_s (s^{-1})
3.2×10^3	1.4×10^4	1.8×10^4	6.4×10^3	7.6×10^3
Branching ratio from energy level i to j				
a_{51}	a_{52}	a_{53}	a_{54}	a_{21}
0.24	0.23	0.2	0.33	0
a_{41}	a_{42}	a_{43}	a_{31}	a_{32}
0.18	0.24	0.58	0.27	0.73
Energy transfer rates				
c_1 (s^{-1})	c_2 (s^{-1})	c_3 (s^{-1})	c_4 (s^{-1})	
6.3×10^4	5×10^4	7×10^4	5×10^3	
Cross-relaxation coefficients				
k_{51} (s^{-1})	k_{41} (s^{-1})	k_{31} (s^{-1})	P_{980} (s^{-1})	
4.8×10^5	1.75×10^5	1.5×10^5	2.8×10^5	

Although the overall 455 nm emission band involves various energy redistribution mechanisms, we find that the emission at low excitation irradiance is similar to a

conventional multiphoton (five-photon) phenomenon. Due to the superlinear emission property in UCNPs, the low excitation intensity would minimize resolution loss and enable Taylor series analysis in this work. Following a similarly reported derivation [72], we can express the fluorescence intensities of the i-th step $F_i(x)$ as a sum of linear and nonlinear components.

$$F_i(x) = KN_0(aI_{0i}^N g^N(x) - a^2 I_{0i}^{2N} g^{2N}(x) + a^3 I_{0i}^{3N} g^{3N}(x) - \cdots) \qquad (2-7)$$

Where $K = \frac{\psi_F}{\tau}$, N_0 is the concentration of the fluorophore, $a = \tau\sigma_N \left(\frac{\lambda}{hc}\right)^N$, σ_N is the cross-section for N-photon excitation, λ is the excitation wavelength, h is Planck's constant, c is the velocity of light, I_{0i} is the focal irradiance of the i-th step, $g(x) = \exp\left(-\frac{2x^2}{\omega_0^2}\right)$. Notably, the higher power of $g(x)$ represents components of the higher spatial information, which means $g^N(x)$ is the diffraction-limited component. According to the derivated equation, the lowest power of $g^N(x)$ dominates the spatial resolution of $F_i(x)$. Thus, the image processing strategy is to eliminate the lowest M-1 powers of $g^N(x)$. By linearly combining M steps of confocal images captured with varied illumination intensities, we can generate an image with $\sqrt{M}$-fold higher resolution. For example, combining two fluorescence images yields a super-resolution image with $\sqrt{2}$-fold increase in spatial resolution, while $\sqrt{3}$-fold enhancement for three images.

2.3.4 **Simulation**

Generation of simulated data

This section describes the underlying algorithms and performs theoretical simulations to assess the performance in nanoscopy. The details of the system and the imaging procedure for the point-scanning microscopy have been described in our recent work [74]. Briefly, the emission is collected by an objective lens with a high numerical aperture (NA = 1.4) and focused by the tube lens onto the single-photon detector, so that the effective PSF ($h_{em}(x, y)$ can be described as:

$$\begin{cases} h_{eff}(x,y) = h_{em}(x,y) \times h_c(x,y) \\ h_{em}(x,y) = \eta(i) \times h_{exc}(x,y) \end{cases} \qquad (2\text{-}8)$$

Here $h_{em}(x,y)$ is the PSF of emission; $h_c(x,y)$ is the PSF of the confocal collection system; $h_{exc}(x,y)$ is the PSF of the excitation beam (Gaussian beam); $\eta(i)$ is the excitation power dependent emission intensity curve; The full width at half-maximum (FWHM) of the intensity in PSF ($h_{exp}(x,y)$) represents the nanoscopy resolution. The experimentally measured intensity distribution PSF ($h_{exp}(x,y)$) on the image plane in our system is the convolution between the $h_{eff}(x,y)$ and the spatial distribution profile ($h_{UCNP}(x,y)$) of nanoparticle as below:

$$h_{exp}(x,y) = h_{eff}(x,y) * h_{UCNP}(x,y) \qquad (2\text{-}9)$$

Simulation result

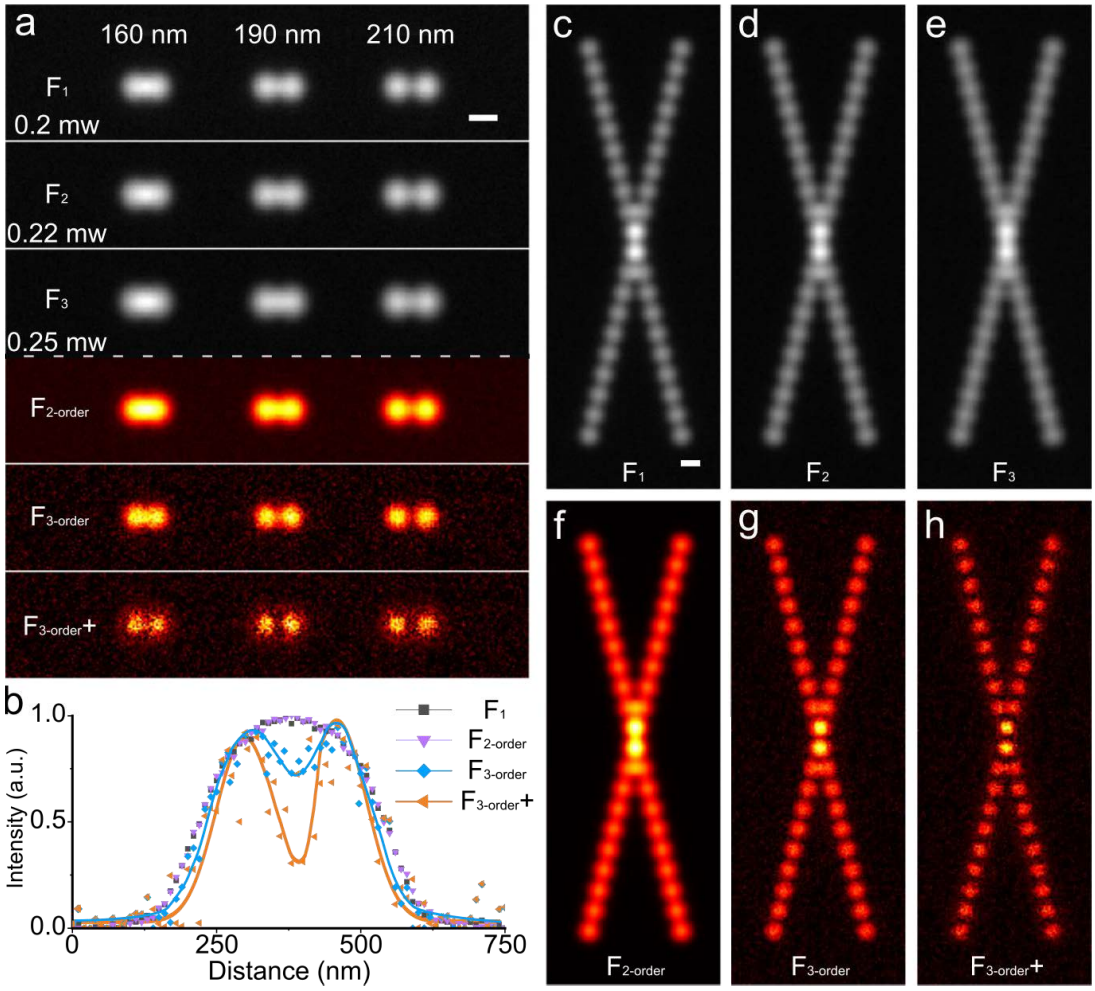

Figure 2-7. Simulation for resolving adjacent nanoparticles and X-bars. (a) Simulated fluorescent imaging (Grey) of two adjacent emitters with a distance from 160 nm to 210 nm under differential excitation

intensity. Super-resolution imaging (Hot) results from two or three stepwise algorithms for comparison. FM represents the Fourier modulation process based on the results of 3-step. Scale bar is 200 nm. (b) The cross-section profiles of the simulated images of the nanoparticles with 160 nm distance in (a). (c-h) The simulation of the X-bar cross line shape structure with sparse UCNPs. Scale bars are 200 nm.

Next, we use the above differential excitation techniques to extract higher-order nonlinear information from superlinear images to simulate resolving adjacent nanoparticles (**Figure 2-7a**). The fluorescent images of two emitters with a distance from 160 to 210 nm are simulated under different excitation powers at 0.2 mW, 0.22 mW, and 0.25 mW, respectively. The fluorescence wavelength is 455 nm, which is the same as the UCNPs used in the later experiments. We input the full set of simulated images with the superlinear approach (0.2 mW, 0.22 mW, and 0.25 mW) and differential excitation algorithms for comparison. In addition, we employ Fourier modulation (FM) based on the results from the stepwise method to extract higher orders of fluorescence response components and increase resolution[75]. From the cross-section profiles in **Figure 2-7b**, Fourier modulation provides the highest ability to resolve two adjacent emitters with FWHM at 130 nm compared to the original value at 190 nm. The discrepancy between these values and the theoretical values of 1.4 and 1.7 is due first to the noise and second to the third-order polynomial function being only a rough approximation of the entire Taylor series. We also perform the simulation of the X-bar design labeled the emitters as the continuing crossline structures (**Figure 2-7 c-h**). In this case, Fourier modulation locates the lines down to ~130 nm in position and illustrates the contour profile precisely, indicating its capability in resolving line structures in optical nanoscopy.

2.4 Resolution enhanced by stepwise

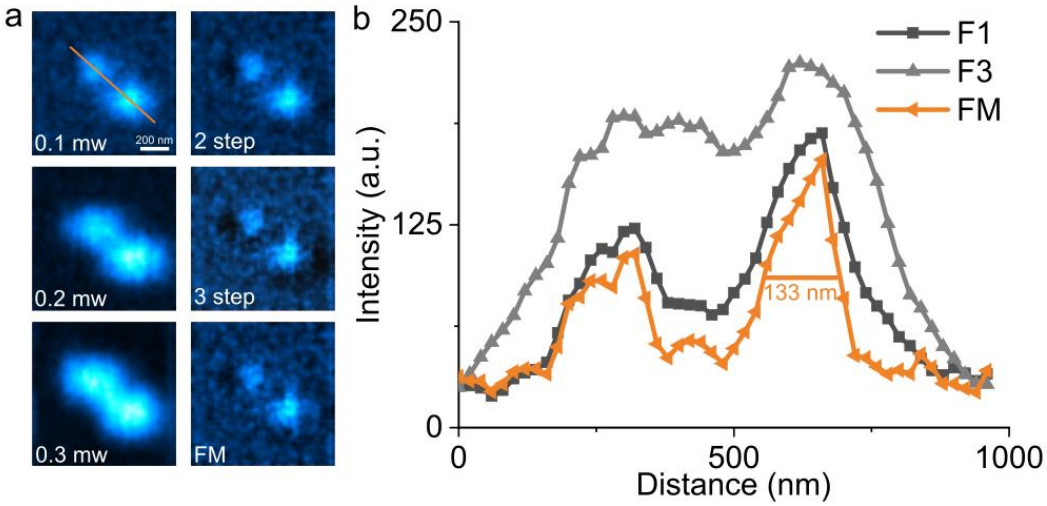

Figure 2-8. Resolving the signal UCNPs in sub-diffraction volume. (a) The 455 nm emission band image of UCNPs under a 980 nm excitation (0.1 mW, 0.2 mW, 0.3 mW) and their corresponding results with differential excitation multiple steps. (b) Line profiles of two nearby UCNPs from (a). Pixel dwell time, 1 ms. Pixel size, 20 nm. The scale bar is 200 nm.

To experimentally confirm the stepwise algorithm for UCNPs, we resolve two adjacent nanoparticles. We first record the images of UCNPs under three different excitation powers (**Figure 2-8a**). We can see the progressive resolution with the decreasing excitation power from 0.3 mW to 0.1 mW, as the two single UCNPs are connected under 0.3 mW while they are almost discrete under 0.1 mW. This resolution enhancement is attributed to the super linearity of UCNPs. Based on this, we employ the stepwise algorithm to obtain 2-step and 3-step results, respectively. Apparently, the two UCNPs are separated after a 2-step treatment. Analyzing the line profiles, we can get the best resolution of 220 nm before any stepwise treatments, which is further enhanced by 3-step treatment to 133 nm, respectively (**Figure 2-8b**). This further enhancement of resolution is close to 1.14 and 1.73-fold of the best resolution of UCNPs within the super linear regime. It should be noted that the resolution can be further improved if employing more gradient excitation power, which will be restricted by the signal-to-noise ratio.

2.5 Conclusion

In conclusion, we upgrade the super-resolution leveraging the nonlinear optical response of UCNPs under the gradient excitation powers. We collect the series of super-resolution images (*M* raw images) using confocal microscopy. The dynamic variable PSFs provide

the higher-frequency spatial information for employing the stepwise operation, which improves the resolution by $\sqrt{M}$ fold. Instead of the complete saturation curve of all the detected pixels[70], our method shows that two or three images with differential saturating degrees are sufficient to offer a substantial improvement in a resolution under ultra-low excitation intensity. It is theoretically possible to further compress the PSF by decreasing the excitation power (e.g., 4-step), however, it is hard to achieve this experimentally owing to the deteriorating signal-to-noise ratio.

This work employs highly dual-doped ions (Yb^{3+} and Tm^{3+}) nanoparticles as fluorescent probes to produce a nonlinear dependency of the emission intensity on the excitation power under the continuous-wave laser. This slope can be further increased by optimizing the activator/sensitizer concentration or designing a core-shell structure, implying an enormous scope for the materials science community to improve the resolution. Our technique can directly utilize the giant nonlinear response induced by the photo-avalanching effect in UCNPs [19], but we need to address imaging speed. Moreover, by taking advantage of the heterochromatic nonlinear responses [74], we can circumvent multiple image acquisition procedures under differential excitation powers. It will be fascinating to verify this notion with the design of the optimized probe in the upcoming work to simultaneously get a series of multi-colour images at differential saturating degrees via the parallel detection channels.

Chapter 3 Improve the force sensitivity of optical tweezers to aN level combining astigmatism and machine learning

Nanoscale sensing and detecting optical force is of great significance for the local viscosity, temperature and pH value of the surrounding media. The sensibility of force requires nanoprobes with smaller sizes, however, the resultant lower magnitude of scattering challenges the measuring method. Here we report the measurement of 3D trapping force from optically trapped lanthanide-doped nanoparticles. We developed an optical astigmatism video tracking (OA-VT) method empowered by a deep neural network (DNN). We find the trained model using the lateral and axial locations of the trapped nanoparticles from astigmatism-modified PSF patterns can allow lateral force sensitivity up to 600 aN and axial force sensitivity of 450 aN, more than 5-fold lower than the reported value by the power spectrum method[76]. This work offers a more efficient measurement of the trap stiffness of low refractive index nanoparticles, achieving single-molecule-level force sensitivity.

Part content of this chapter is from the paper:

X. Shan†, **L. Ding**† (co-first), S. Wen, J. Lu, J. Chennupati, D. Jin* and F. Wang*. Atto-Newton Force Sensitivity of Machine Learning Empowered Astigmatism Optical Tweezers. (*to be submitted*)

3.1 Challenge of force sensing for current strategies

Optical force requires sufficient sensitivity for sensing and detecting local variations of the microenvironment, such as local viscosity [77], temperature [78], and pH value [79] of the surrounding media. It is also used to evaluate the biological interaction force of the DNA string [80] and the traction of kinesin motor protein along the microtubule [81]. An optical tweezer is a powerful tool to sense, characterize, and manipulate particles [49]. It can map the surrounding geometrical information [82], rotate the connected bio-structures and assemble particles into micro/nanostructures [83], due to the manipulation of the sensitive optical force. The trapped particle is usually considered as the ball inside

a harmonic potential well, the movement (i.e., optical force) of which can be described by Langevin equation [84]. In the harmonic potential well, any perturbation induced particle offset from its balance position will generate a restoring force opposite to the offset direction. Hence the offset value of optical tweezers can be used to measure the continuous perturbation force acted on the trapped particle. For detecting a tiny perturbation, optical tweezers need a better sensitivity, which necessitates the smaller nanoprobes.

Trap stiffness describing the optical force has primarily been detected by analysing the scattering intensity variations of the trapping laser. The scattering intensity can be directly transferred to the displacement between the particle and the laser beam [85], in which the trap stiffness is calculated from the statistic of displacement through the equipartition theorem. The trap stiffness can also be extracted from the time-correlated intensity variations through either the power spectrum transferring or the auto-correlation approach [49]. The exact trapping force can be thus calculated by the momentum change, resulting from the scattering intensity distribution. However, nanoparticles with smaller sizes have feeble scattering, as the Rayleigh scattering cross-section is proportionable to the size by a power of six. This poses challenges in both measuring and extracting the scattering signal of nanoprobes from the high laser background, leading to a sufficient sensitivity. Consequently, to the best of our knowledge, the current highest force sensitivity is 2.4 femtoNewtons (fN) [76] by using an 80 nm gold nanoparticle.

Alternatively, several strategies have been explored to measure trap stiffness from optical tweezers. Using the hydrodynamic drag method, Lu et al. extracted the trap stiffness from the displacement of a trapped nanoparticle away from its equilibrium position [86]. This method necessitates moving the trapping environment or the trapping beam, limiting the high spatial resolution in-situ measurement and the force sensing in the vertical direction (laser propagation direction). The digital video microscopy method [87] enables to calculate the trapping stiffness from the nanoparticle trajectory by recording the trapped particle via a high-speed video camera. Based on this, Shan et al. applied fluorescence digital video tracking to characterize the lateral trap stiffness of the ion-resonance enhanced upconversion nanoparticles [88]. However, measuring the axial trap stiffness remains challenging due to the failure of detecting the nanometre shift of the axial position of the trapped particles by two-dimensional (2D) images.

In this chapter, we develop a deep neural network empowered optical astigmatism video tracking method to measure 3D force of optically trapped nanoparticles. The deep neural network distinguishes the difference among the 2D image features of a trapped nanoparticle recorded at different axial positions. The optical astigmatism features and axial position enables the trained images with both lateral and axial information. We can thus obtain the precise axial force measurement. After further optimization, such as the recorded image number, laser power, and home-designed nanoparticles, we achieve the best lateral force sensitivity of 600 aN and axial force sensitivity of 450 aN. We envision the efficient force measurement with the supersensitivity to provide potential in sensing the tiny perturbation for living cells and the quantum interaction.

3.2 Methods

3.2.1 Optical astigmatism-enhanced optical tweezers

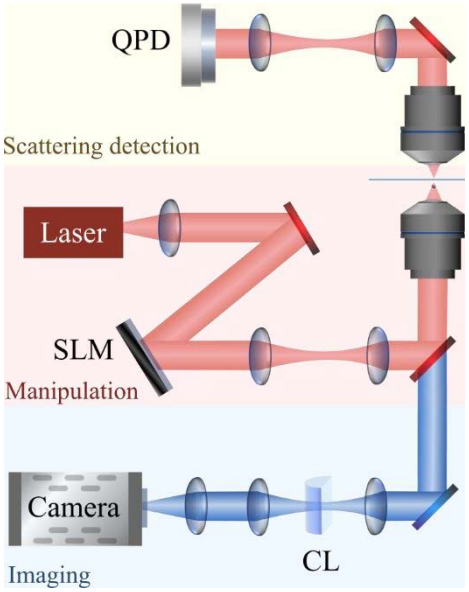

Figure 3-1. Schematic of optical astigmatism-enhanced optical tweezers.

The far-field optical tweezer system (**Figure 3-1**) is composed of three parts - trapping beam manipulation, optical imaging and scattering detection. For the manipulation part, the beam pattern from a 980 nm diode laser is modulated by a SLM. It is very important for detecting the axial force since we can record the 2D images under different z positions by adjusting SLM. In the imaging path, a cylinder lens (CL) is installed for introducing optical astigmatism to measure the axial force. For the scattering detection part, a QPD is

used to detect the position information of trapped nanoparticles. Compared with the conventional optical tweezers system, we add the cylinder lens to obtain optical astigmatism for the axial force detection integrating with the deep learning algorithm, which will be introduced later.

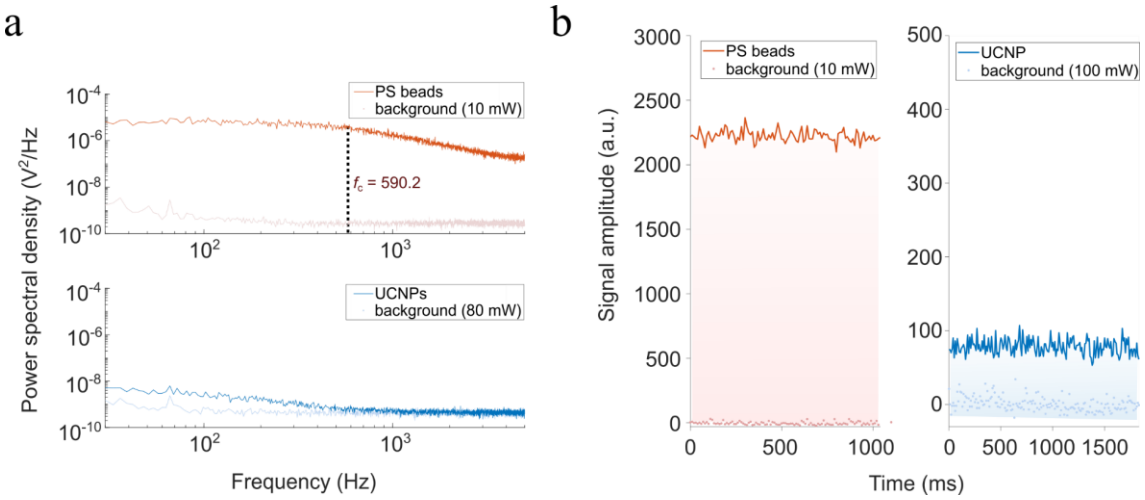

Figure 3-2. Measurement for lateral trap stiffness. (a) QPD method for measuring the lateral trap stiffness of 1 mm PS bead and 58 nm UCNP ($NaYF_4$,20%Yb,2%Er). *f*c is the corner frequency. (b) Comparison of signals from the QPD method and video tracking method.

To measure the lateral trap stiffness, the most popular method is fitting the light scattering curve detected by the power spectrum using the Lorentzian function (**Figure 3-2a**) [49]. This method works well for large particles, i.e., 1μm polystyrene sphere (PS, **Figure 3-2a** upper). However, detecting the scattering signal for nanoparticles is more challenging, as the scattering cross-section decreases with the radius of the particle in the power of six according to Rayleigh scattering [89]. Consequently, the obtained power spectrum from a trapped 57 nm nanoparticle is weak and noisy so the fitting cannot be conducted (**Figure 3-2a** bottom). Digital video tracking of the trapped fluorescent particle is another method to obtain trap stiffness. Therefore, for nanoparticles that are small enough, the best method for trap stiffness is to record imaging videos. It should be noted that PS can be excited by a 980 nm laser and produce two-photon fluorescence, while UCNP can produce multi-photon upconversion fluorescence. The anti-Stokes fluorescence for both PS and UCNNP provides low background and a much higher signal-to-background ratio compared with that for scattering intensity. **Figure 3-2b** shows the signal and background of the trapped PS and UCNP.

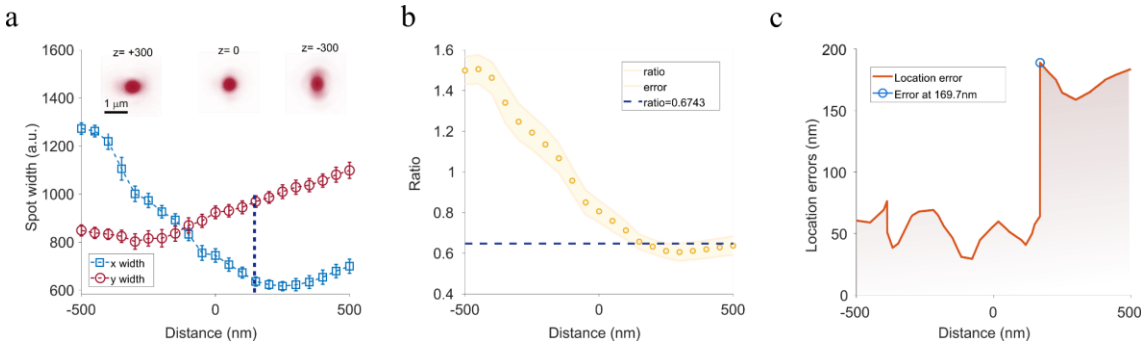

Figure 3-3. Engineered PSF with astigmatism induced from cylindrical lens under different z position. (a) Lateral variations of PSF width of single trapped UCNP under different z positions. Insets are the images of the particle with astigmatism. (b) The x-y ratio of PSF width varying with the z position. (c) Location errors of the x-y ratio method.

The axial trap stiffness remains challenging for either spectrum or video trapping methods. To encode the axial position information into the 2D image, we integrate a cylinder lens into the imaging path for introducing optical astigmatism. The cylinder lens will add a parabolic phase in the horizontal direction of the image that shifts the horizontal focus and modifies emitters' point spread function to an "elliptical" shape when the emitters are out of focus (**Figure 3-3a**). Typically, the pre-characterized PSF waist sizes (on both x and y axises) are used to deduce emitters' axial position [42]. However, it works not efficiently for optical tweezers due to the position variation (Gaussian distribution) of the trapped nanoparticle in a 3D harmonic potential well. The resulted centre of the Gaussian distribution, especially in the axial direction, will lead to a large error on the PSF waist. The error substantially reduces the localisation accuracy and the force sensitivity. It should be noted that the error cannot be circumvented by fixing the particle on the trapping chamber bottom, as the abnormal trapping height (typical trapping height is between 10 to 50 μm above the chamber bottom) generates huge spherical aberration on the emission PSF. We evaluate the possibility of obtaining the axial information using the x-y ratio of PSF waist (**Figure 3-3b**). Obviously, the ratio curve shows a dropping trend between the z positions from -500 to 100 nm with a rough 800 nm error (**Figure 3-3c**). For higher z positions (above 100 nm), the ratio method is not reliable anymore as the location error suddenly increases to 1400 nm. Therefore, a more powerful and convenient strategy is needed.

3.2.2 Deep neural network empowered optical astigmatism video tracking (DNN-OA-VT)

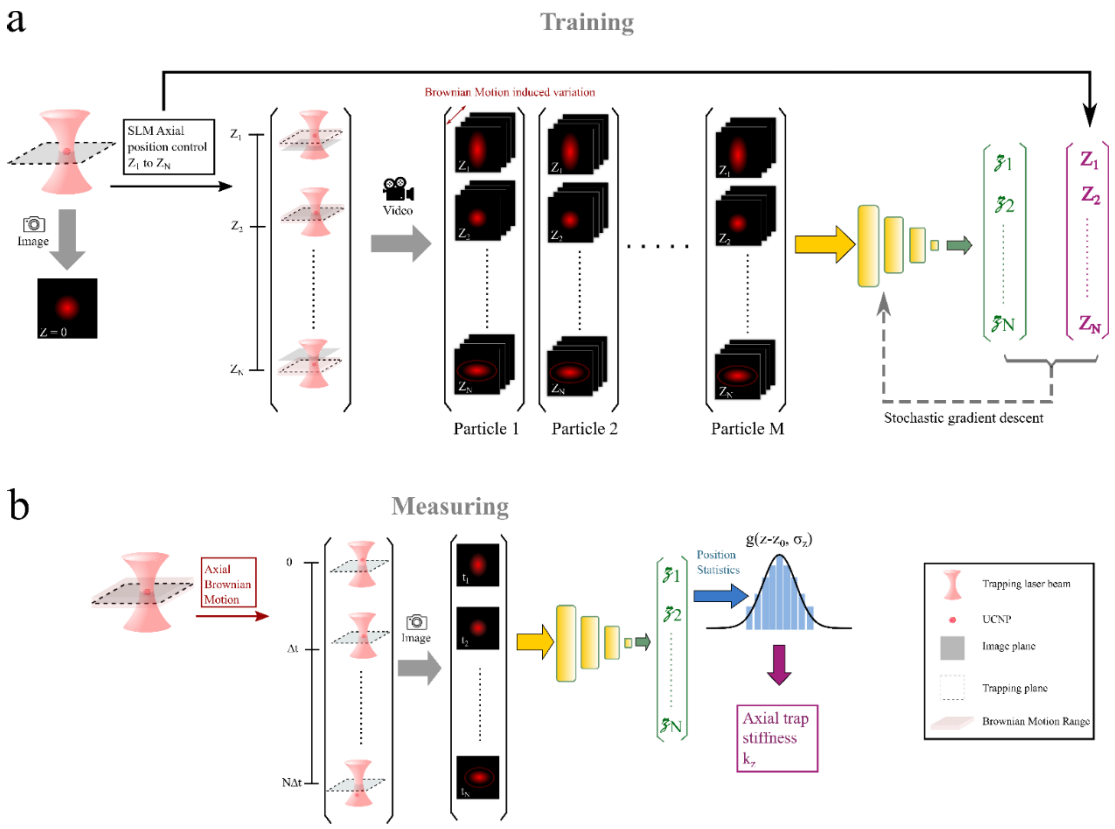

Figure 3-4. Schematic diagram of astigmatism-empowered machine learning strategy. (**a**) The model obtained by recording the videos of the trapped nanoparticles under different z positions and recognising the features of PSF. (**b**) For z-position-unknown video, the trap stiffness can measure by position distribution fitting with Gaussian.

Table 3-1. The parameters of four kinds of UCNPs ($NaYF_4$,20%Yb,2%Er) used for building DNN-OA-VT model.

Sample	1	2	3	4
Diameter (nm)	16.5	30.9	46.4	48.3
Diameter std (nm)	3.1	1.7	1.8	1.3
Height (nm)	16.5	30.9	31.9	35
Height std (nm)	3.1	1.7	1	1.1

Considering much location information including lateral and axial direction, we develop a deep learning algorithm to deal with the 2D image. This could recognize the 2D images' features and resolve their axial (z-axis) position, circumventing the considerable

localization error on the characterization map by the aspect ratio method. In recent years, deep neual network with multiple-nets structure has been proved for recognizing the weeny signatures in images [50]. DNN with some level of complexity (≥ two layers) processes data in complex ways by employing sophisticated math modeling. By capitalizing on the artificial neural network component, DNN works so well at improving a model—because each node in the hidden layer makes both associations and grades importance of the input to determining the output. Therefore, we designed a DNN-OA-VT method for extracting the axial position of the optically trapped nanoparticle from astigmatism-modified PSFs, enabling the measurement of axial trap stiffness. DNN-OA-VT (**Figure 3-4a**) requires building a model with lateral and axial location information via training a series of 2D images acquired at different z positions. Typically, the single nanoparticle is initially trapped at z=0 position (e.g., 20μm away from the trapping chamber bottom). The trapped centre/laser centre of this nanoparticle is then actively moved along the axial positions from Z_1 to Z_N through modulating SLM, while the imaging plane is still fixed on the position of z=0. The recorded 2D images thus carry the position information of Brownian motion at each z position. All the details of the images are trained by deep learning to alleviate the influence caused by Brownian motion and result in a higher accuracy of position, compared with the aspect ratio method. In this chapter, the trapping images of several types of UCNPs with different sizes (**Table 3-1**) [88] will be recorded and trained for comprehensive and completed location information. In general, for each axial trapping position (e.g., Z_1), a video is taken to record a series of PSF images (e.g., *K* images). After the independent measurement on *M* nanoparticles, a number *K*M* of images is grouped up to characterize one axial position. Together with other groups of images at different axial positions (*N*), a total number of *K*N*M* images are input into DNN to identify the characteristic image features for different axial positions. The biases of real and labelled (modulated axial position) positions caused by Brownian motion are equally distributed on both sides of labelled positions. It should be noted that more training data will minimize the impact of Brownian motion to an extreme. Therefore, the model is built to predict the real position of the trapped nanoparticles.

In the applying stage (**Figure 3-4b**), a single nanoparticle is trapped at z=0 position, while its instant position varies within a small range with time. Taking a video of the emission pattern for 100s will generate a series of images (e.g., 10000 slides), and the trained DNN

model can convert each of them into an axial position value. The statistic of axial positions can be fitted into equation (3-3) to extract the axial trap stiffness. The lateral trap stiffness can be extracted from these images through conventional Gaussian fitting [42].

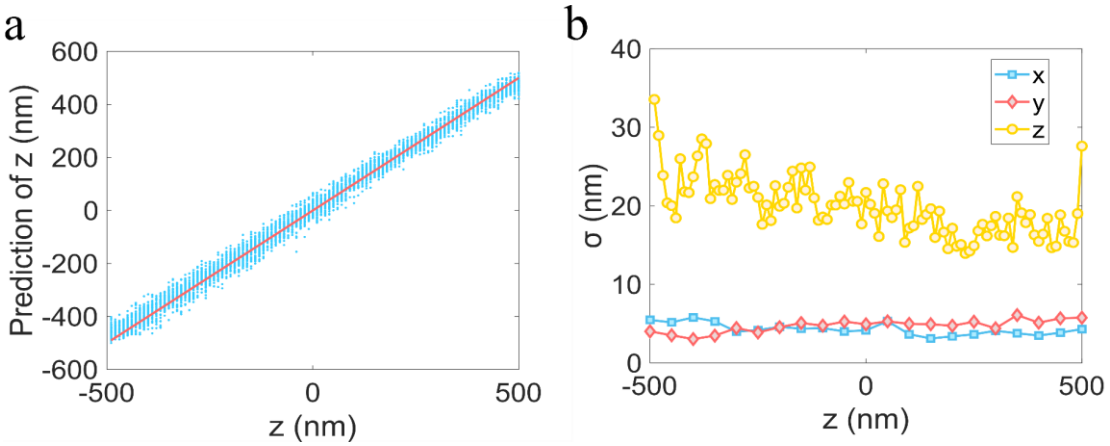

Figure 3-5. Position localisation accuracy. (a) Red line and dots represent the evaluation of predicted value and truth value. (b) 3D localisation accuracy of x-, y- and z-axis. The nanoparticle is NaYF4,20%Yb,2%Er, the diameter is 58nm.

To verify the measurement method, we obtain the accuracy of both lateral and axial force by calculating the standard deviation of the 2D pattern centre position from a series of images. We test 25 groups of the trapped nanoparticles with the size between 30 and 60 nm under the z position from -500 to 500 nm. It should be noted that the accuracy of lateral force only depends on the 2D image localization instead of the deep learning training. This has been demonstrated in our previous work [88]. The accuracies for the lateral force of the x-axis and y-axis are close and stable (both are around 5 nm). By contrast, the accuracy for axial force is around 20 nm (**Figure 3-5c**) after improvement by deep learning. The lateral force accuracy is produced from hundreds and thousands of position spots resulting from the Brownian motion, while the axial force accuracy is from modulating SLM for z positions from -500 nm to 500 nm signifying 100 position spots. The uniformity between prediction and truth of the z position demonstrates the reliability of this measurement (**Figure 3-5c**). Besides, we can also notice the large fluctuations of z-axis accuracy at the edges (-500 nm and 500 nm). We attribute this to the cutting range of the training, as the lower position is limited to -500 nm and the higher position is 500 nm. The test results thus validate the DNN-OA-VT for both the lateral and axial force sensing.

3.3 Results and discussion

3.3.1 3D trap by DNN-OA-VT

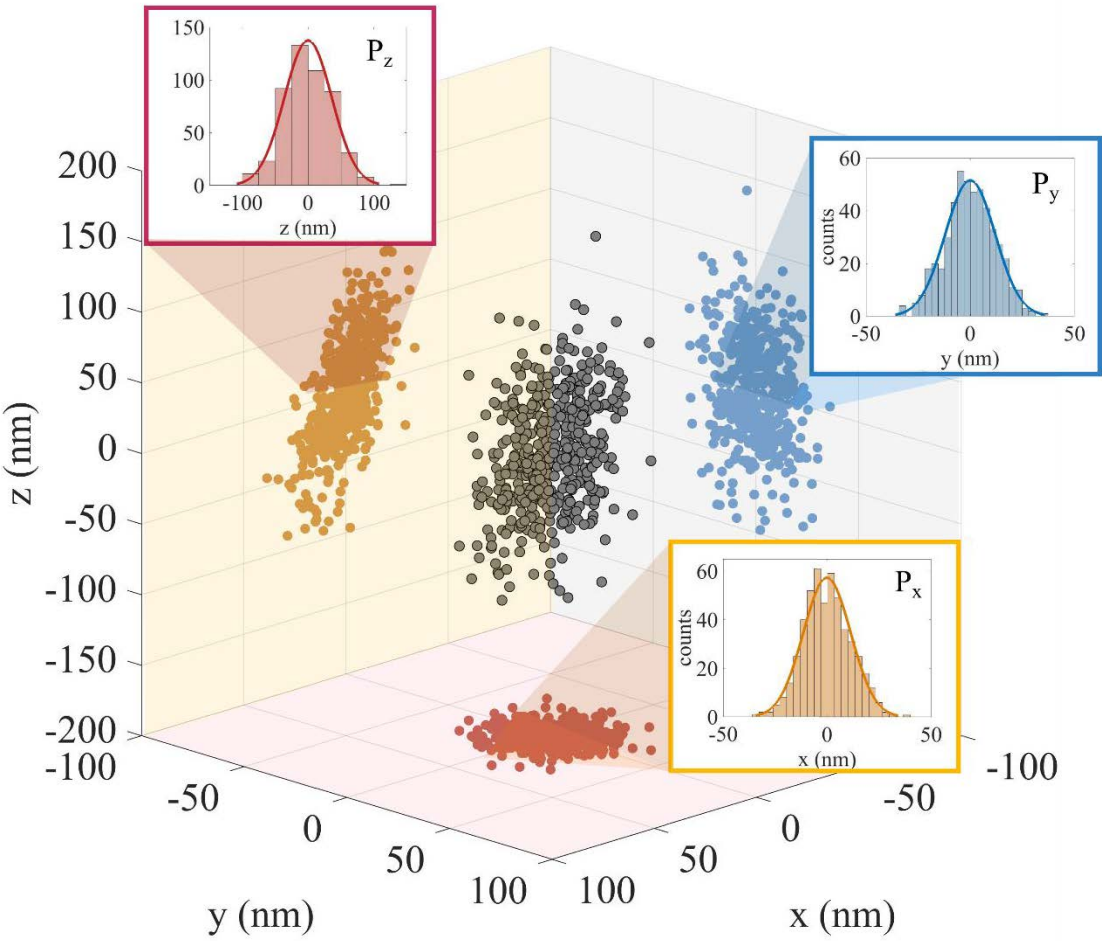

Figure 3-6. Three-dimensional scatter plot of positions for a trapped nanoparticle.

We further investigate the 3D trap stiffness of a single UCNP by the DNN-OA-VT. To our best knowledge, the axial trap stiffness of UCNPs has never been measured due to the lack of an efficient method. **Figure 3-6a** shows the position distribution of an optically trapped 60 nm UCNP by the DNN-OA-VT, with a trapping laser of 244.7 mW (980 nm laser). By fitting the position histogram into Gaussian functions, we achieve the 3D trap stiffnesses are 1.79, 4.9 and 0.93 pN/μm for the x-, y- and z-axis, respectively. Here the z trap stiffness is always smaller than the x- and y-axis trap stiffness. The unsymmetrical potential well in the axial direction only provides weaker confinement for the trapped particle denoting larger spot position distribution, while the lateral force makes a tight

spot distribution. Besides, the tightly focused linearly polarized beam provides more gradient perpendicular to the polarized direction (y). Therefore, this polarize-induced unsymmetrical lateral beam spot enables the x-axis trap stiffness slightly larger than the y-axis trap stiffness. These results match with the theoretical prediction by Alexander Rohrbach [90].

3.3.2 **Force sensitivity analysis**

Then, we will display the function of this DNN-OA-VT strategy to achieve the force sensitivity on three axises. To do that, we first build the relationship between the trap stiffness and the position of the single trapped UCNP in both lateral and axial directions. The formula of force sensitivity is derived as the following analytical interpretation:

According to the Langevin equation [91], under thermal equilibrium conditions, the position (probability distribution) of a Brownian particle within a liquid solution follows the Maxwell-Boltzmann distribution, as shown:

$$\mathrm{P(x)} \propto \exp\left(-\frac{U(x)}{k_B T}\right) \qquad (3-1)$$

where $U(x)$ is the potential energy, k_B is the Boltzmann's constant, T is the experiment temperature. Approximately, an optical trap could be treated as a harmonic potential well which has potential energy as:

$$U(x) = \frac{1}{2}k(x)^2 \qquad (3-2)$$

here k is the trap stiffness, and the central position of the harmonic potential well is x=0. Hence the position distribution of the trapped particle is a Gaussian distribution:

$$\mathrm{P(x)} \propto \exp\left(-\frac{k(x)^2}{2k_B T}\right) \qquad (3-3)$$

The instant trapping force can be expressed as $F = kx$ when the particle is inside the laser beam spot. This position distribution will shift from the central position when a constant external force is acted on the particle, with the expression as:

$$\mathrm{P(x)} \propto \exp\left(-\frac{k\left(x-\delta_{eq}\right)^2}{2k_B T}\right) \qquad (3-4)$$

Here δ_{eq} is the position shift from the equilibrium position, and results in a restoring force $F_{ex} = k\delta_{eq}$ to balance the constant external force. Therefore, the external force can be measured by the distribution shift. This technology has been called as Photonic Force Microscope [92][93]. The force sensitivity depends on the localisation accuracy of the δ_{eq}, with $\Delta F_{ex} = kSD_{eq}$. Here SD_{eq} is the standard deviation of the detected distribution shifts (δ_{eq}). The δ_{eq} arises from the statistic result with a limited sampling number. The highest reported sensitivity is 2.4 femtonewtons by Zensen et al.[76]. In this work, we use the video tracking method to detect distribution shifts, which generates a better signal-to-background ratio.

We first estimate the possibility of a measured position by our imaging method. According to the equipartition theory (equation 3-3) the possibility of the particle in location x_i is $\mathrm{P}_k(x_i) \propto \exp\left(-\frac{{x_i}^2}{2{\sigma_k}^2}\right)$, with $\sigma_k = \sqrt{\frac{k_B T}{k}}$ is the variance. A single nanoscale emitter's location is a Gaussian distribution with a variance of σ_p that is called localisation accuracy as well. Hence the possibility for the particle (located at x_i) is detected at position x is $\mathrm{P}_{det}(x) \propto \exp\left(-\frac{(x-x_i)^2}{2{\sigma_p}^2}\right)$. Therefore, the possibility of a particle being located at position x is by adding all the detecting possibilities for particles located in a different position, as $\mathrm{P} \propto \sum_i P_k P_{det}$. One could also understand it as the possibilities multiplying is a convolution process. The integration format of possibility is:

$$\mathrm{P(x)} \propto \int_{-\infty}^{+\infty} \exp\left(-\frac{(x-x_i)^2}{2{\sigma_p}^2}\right) \exp\left(-\frac{{x_i}^2}{2{\sigma_k}^2}\right) dx_i \qquad (3-5)$$

$$= \int_{-\infty}^{+\infty} \left[e^{-\left(\frac{1}{2\sigma_p^2}+\frac{1}{2\sigma_k^2}\right)x_i^2} + \frac{x x_i}{\sigma_p^2} - \frac{x^2}{2\sigma_p^2} \right] dx_i \qquad (3-6)$$

Applying the mathematic formula of $\int_{-\infty}^{+\infty} e^{-ax^2+bx+c} dx = \sqrt{\frac{\pi}{a}} e^{\frac{b^2}{4a}+c}$, equation (3-6) can be simplified as:

$$\mathrm{P(x)} \propto \exp\left(-\frac{x^2}{2\left({\sigma_p}^2 + {\sigma_k}^2\right)}\right) \qquad (3-7)$$

With this detected position distribution, the localization accuracy can be calculated by the statistics method. Similar to deriving the localisation accuracy for single-molecule localization microscopy [42], the position shift measuring accuracy consists of two parts, with the formula shown:

$$SD_{eq}{}^2 = \langle \delta_{eq}{}^2 \rangle = \frac{\sigma_p{}^2 + \sigma_k{}^2}{N} + \frac{\frac{a^2}{12}}{N} \qquad (3-8)$$

where the first term comes from the distribution or possibility of the detected position. For *N* times of measurement, the statistical centre localisation accuracy is $(\sigma_p{}^2 + \sigma_k{}^2)/N$. The second term comes from the uncertainty of where the statistic point locates. *a* is the size of the unit of the grid axis for the statistic histogram, and $\frac{a^2}{12}$ is the variance of a top-hat distribution that matches the grid axis. Note that, the histogram here is the position trajectory rather than photon counts, hence we don't have a background noise term for the position shift measuring accuracy. Substituting $\sigma_k = \sqrt{\frac{k_B T}{k}}$ into equation (3-8), the targeting accuracy can be expressed as:

$$SD_{eq} = \sqrt{\frac{\sigma_p{}^2 + \frac{k_B T}{k} + \frac{a^2}{12}}{N}} \qquad (3-9)$$

During the post-analysing process, the *a* is about $\frac{6 \times SD_{eq}}{N_h}$. Here 6 is to cover all the efficient statistical points, according To Gaussian distribution. N_h is the axis grid number, we are using 30 in our experiment. Hence, we could further derive equation (3-9) into:

$$SD_{eq}{}^2 = \frac{\sigma_p{}^2 + k_B T/k}{N} + \frac{3}{N \cdot N_h{}^2} SD_{eq}{}^2 \qquad (3-10)$$

$$SD_{eq} = \sqrt{\frac{\sigma_p{}^2 + k_B T/k}{N - 3/N_h{}^2}} \qquad (3-11)$$

Finally, we obtained the equation for the force sensitivity as:

$$\Delta F_{ex} = k SD_{eq} = \sqrt{\frac{(k\sigma_p)^2 + (k_B T)k}{N - 3/N_h{}^2}} \qquad (3-12)$$

For most cases, the sampling number N is much larger than $3/{N_h}^2$. So the equation can be simplified as:

$$\Delta F_{ex} = \sqrt{\frac{(k\sigma_p)^2 + (k_B T)k}{N}} \qquad (3-13)$$

where k is the trap stiffness, σ_p is the imaging localisation accuracy, k_B is the Boltzmann's constant, T is the experimental temperature, N is the total scatters' number and N_h is the binning number for a histogram. Finally, we build the relationship between the force sensitivity with the imaging localisation and the sampling number.

3.3.3 aN-level force sensitivity simulation using Monte Carlo

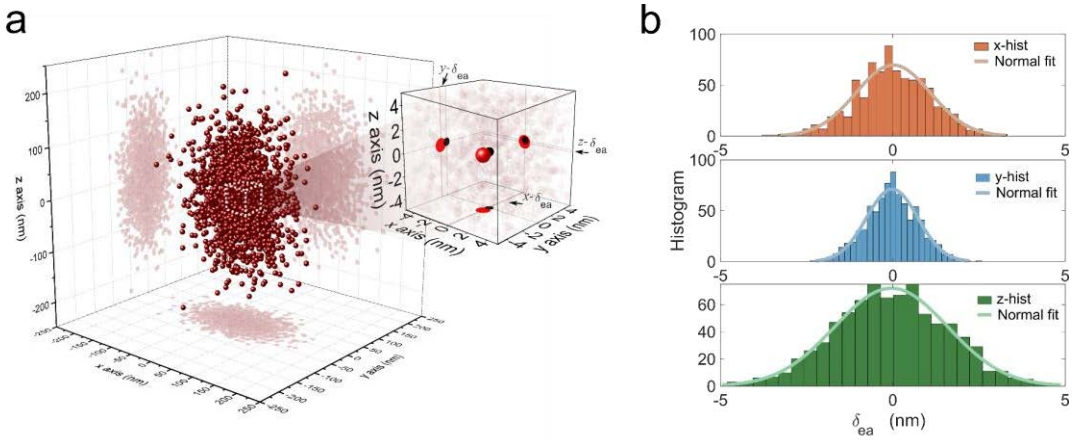

Figure 3-7. Simulation of the optically trapped nanoparticle. (a) 3D positions plot for a single trapped nanoparticle and its projection. (b) 3D position distribution. laser power is 35.8mW, trap stiffnesses are 0.05, 0.137 and 0.026 pN/um/mW for x-, y- and z-axis, respectively. The scattering point is 1610. Data number Nr=1678.5, SD_{eq} is 1.0859, 0.7429, and 1.6386 for x-, y- and z-axis, respectively.

We further use Monte Carlo trapping simulation to verify the developed formula and investigate the best sensitivity. **Figure 3-7a** shows the simulated position distribution of the optically trapped nanoparticle with the trapping centre at the origin (black dot at the insert), while the averaged position centre (red dot at the insert) shows offsets at the x, y and z-axis. Repeating the centre measuring 800 times, the histogram of offsets (**Figure 3-7b**) indicates a Gaussian distribution with a standard deviation SD_{eq}. Similar to the localisation accuracy for single-molecule localization microscopy [42], the SD_{eq} is calculated by considering the error introduced by distribution possibility and the uncertainty of the statistic points. Here the possibility of one nanoparticle shown at the

detected position is a convolution between the trapping potential well induced position distribution and the emitter's detecting location distribution. The uncertainty of the statistic stands for the unit grid length of the histogram.

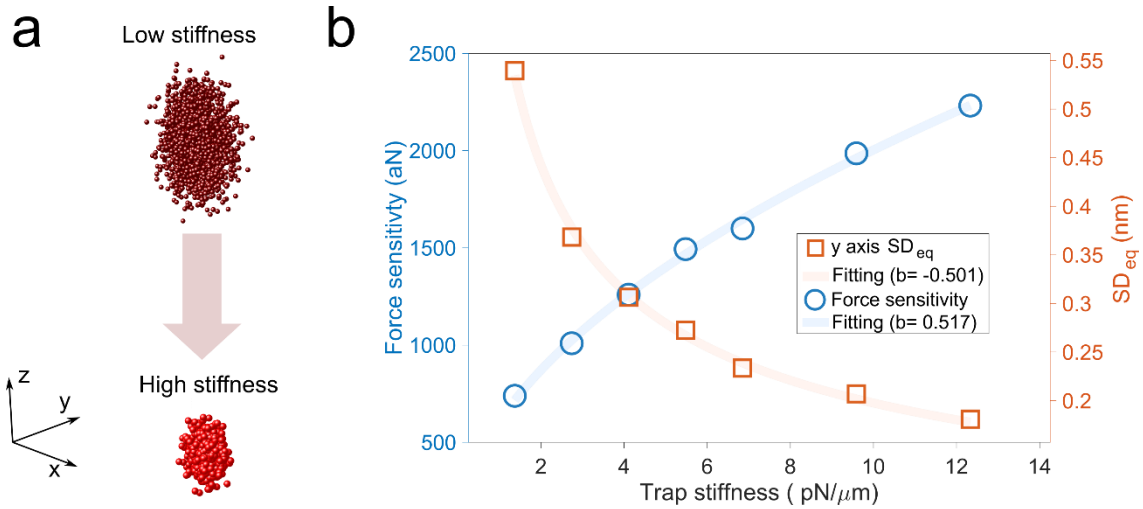

Figure 3-8. The effect of force sensitivity on trap stiffness. (a) Scheme of the trapped nanoparticle moves under low and high stiffness. (b) Force sensitivity and position shift accuracy varying with trap stiffness. Assume $\sigma_p$is 0. Data number Nr is 10000, laser power is from 10 to 90mW, stiffnesses are 0.05, 0.137 and 0.026 pN/um/mW for x-, y- and z-axis, respectively.

According to equation (3-13), the force sensitivity can be optimized by tuning the parameters. To obtain the impact of trap stiffness to sensitivity (**Figure 3-8a**), we assume the imaging localisation is absolutely accurate (σ_p=0). The measured SD_{eq} show the power of -1/2 relation with trap stiffness, as shown in **Figure 3-8b** orange square, matching with the prediction. While the minimum sensible force increases with the trap stiffness with a power of 1/2 (labelled by blue circles), which indicates that the smallest trapping stiffness should be used to obtain the highest sensitivity. To this end, the force in the axial direction will have a better sensitivity than that in the lateral direction, due to the smaller stiffness. For the conventional lateral force, the force sensitivity for the x-axis also shows better than that for the y-axis. Experimentally, the minimal trap stiffness for a stable long time trapping a single 60 nm UCNP is 1.79, 4.9 and 0.93 pN/μm for the x-, y- and z-axis, respectively. Therefore, we can obtain the highest force sensitivity on the z-axis, followed by the x-axis and y-axis.

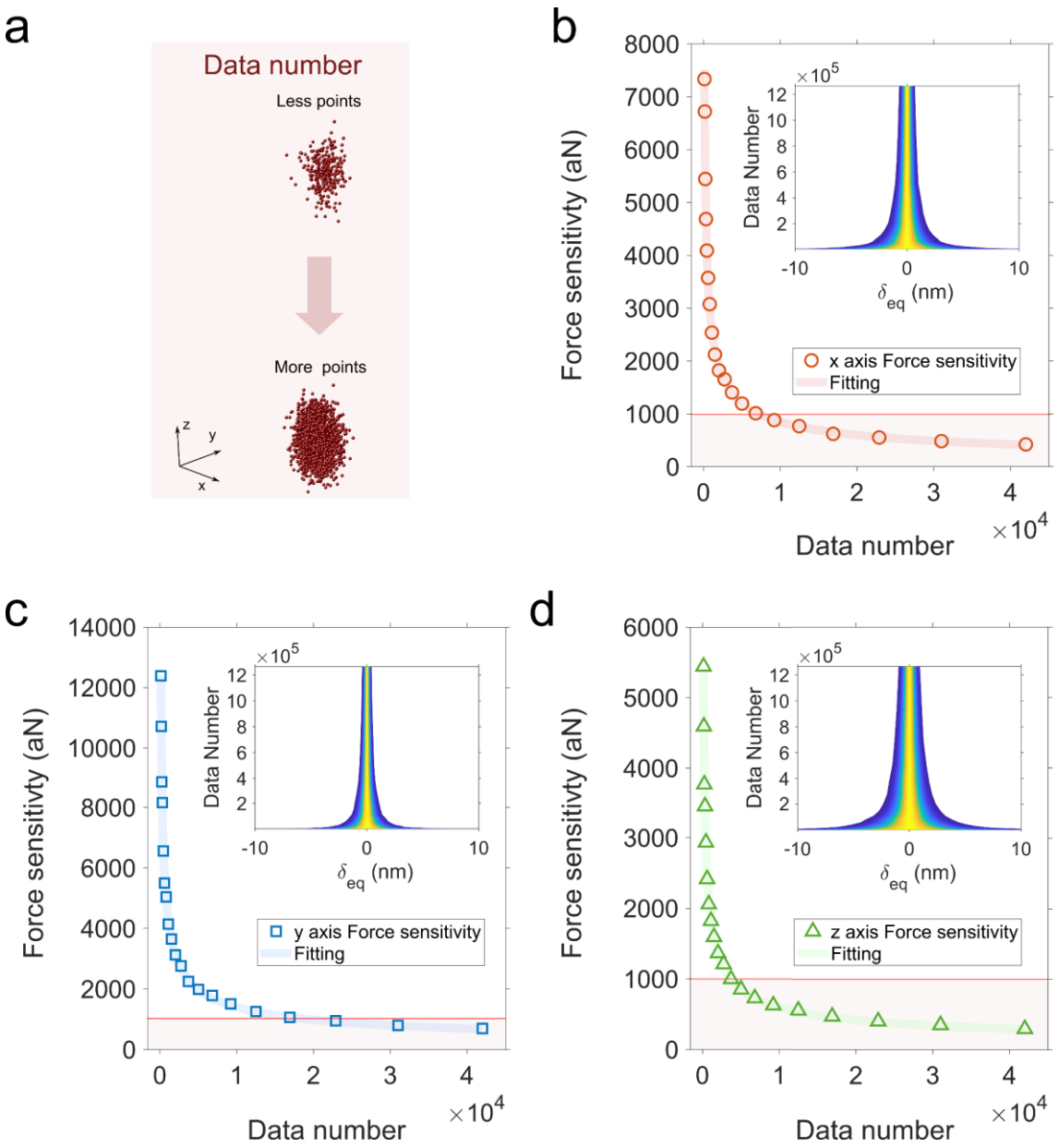

Figure 3-9. The effect of force sensitivity on data number. (a) Scheme of the trapped nanoparticle obtained with less and more points. (b) Force sensitivity varying with the data number for the x-, y- and z-axis. Assume $\sigma_p$is 0. Laser power is 35.8 mW.

The force sensitivity is also affected by the sampling number according to equation (3-13). We evaluate the sensitivity performance under different data numbers. **Figure 3-9** shows that a larger data number narrows down the histogram (insert), with SD_{eq} hyperbolically decreases. Here we set the trap stiffness as the minimal experimental value σ_p=0, then the sensitivity can the highest. In this condition, the simulated sensitivity values for the x, y and z-axis (**Figure 3-9 b-d**) decrease with data number with the power

of -1/2, consistent with the simplified equation $\Delta F_{ex} = \sqrt{k_B T k / N}$. This result suggests that minimum data numbers of 7000, 20000, and 3400 are required for achieving a force sensitivity below 1fN for the x-, y- and z-axis, respectively. Consequently, considering the minimal experimental σ_p, we can obtain the 3D force sensitivity with aN level using the data number of 20,000.

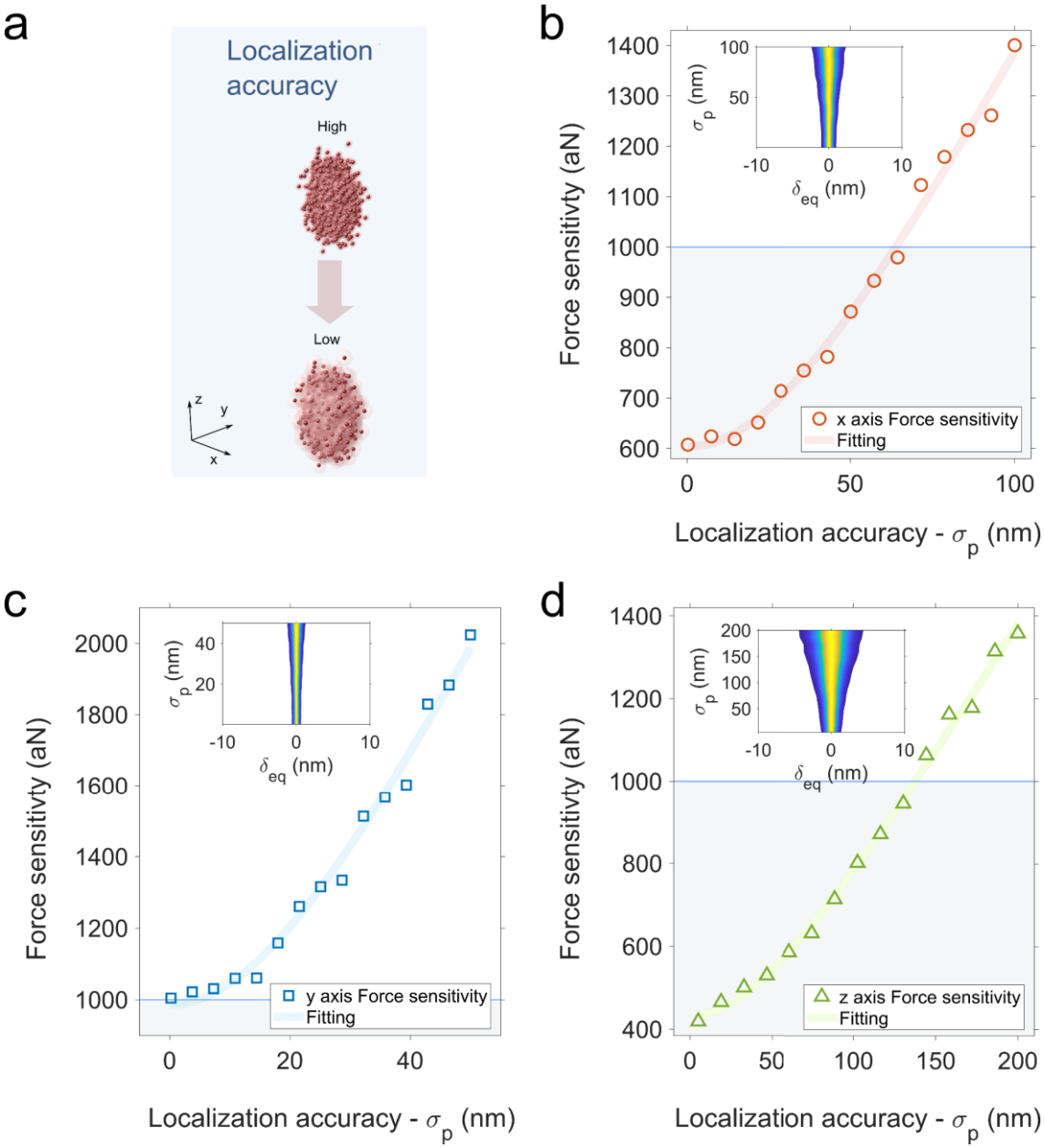

Figure 3-10. The effect of force sensitivity on localization accuracy. (a) Scheme of the trapped nanoparticle obtained with high and low accuracy. (b) Force sensitivity varying with localization accuracy for the x-, y- and z-axis. Laser power is 35.8 mW and the data number is 20000.

Localization accuracy of the image is another factor to affect the force sensitivity. We simulate the evolution of force sensitivity under different localization accuracies (**Figure 3-10a**). Obviously, smaller σ_p (higher localization accuracy) offers smaller SD_{eq} (**Figure 4e**, insert), resulting in better force sensitivities (**Figures 3-10 b-d**). For achieving the aN-level force sensitivity from three directions, we should get the localization accuracy higher than 64, 4 and 137 nm for the x-, y- and z-axis respectively. In this work, our DNN-OA-VT method can experimentally offer localization accuracy up to 5, 5, and 20 nm for the x-, y- and z-axis, respectively. This enables the best force sensitivity of 600, 1000 and 450 aN for the x-, y- and z-axis, respectively. Notably, equation (3-13) is also valid for force sensing with other position detection methods e.g., scattering intensity detecting.

3.4 Conclusion

In this chapter, we develop a novel and efficient measurement for 3D trap stiffness of optical tweezers (DNN-OA-VT). Based on the powerful deep learning for training/identifying tiny features from a large set of data, we introduce optical astigmatism using the cylindrical lens in the 2D images of the trapped nanoparticles under different axial positions. After a reasonable experimental setup and force sensitivity analysis, we obtain the aN-level 3D force sensitivity. We use the Monte Carlo simulation to achieve the highest force sensitivity of 600, 1000, and 450 aN for the x-, y- and z-axis, respectively. To this goal, the selection of UCNP is one of keys, as the lanthanide ions doped in the nanoparticle produce the larger resonance for enhancing optical force. The homogenous single nanoparticle and stable upconversion fluorescence enable us to realize long-time trapping of single nanoparticles. We wish this work can inspire the exploration of 3D force sensing with ultrahigh sensitivity, in particular axial force sensitivity, and give more chance to detect the tiny disturbance, such as the variations of the membrane potential of the living cell.

Chapter 4 Engineer Rayleigh scattering of nanoparticles via doping lanthanide ions

Light scattering from nanoparticles is significant in nanoscale imaging, photon confinement and biosensing. However, engineering the scattering spectrum, traditionally by modifying the geometric shape of nanoparticles, requires synthesis and fabrication with nanometer accuracy. Here we report that doping the lanthanide ions can engineer the scattering properties of lanthanide ion-doped nanoparticles. When the excitation wavelength matches the ion resonance of lanthanide ions, the polarizability and the resulting scattering cross-section of nanoparticles are dramatically enhanced. We further demonstrate that these purposely engineered nanoparticles can be used for iSCAT microscopy. Conceptually, we further develop multiplexed iSCAT microscopy for the identification of different types of nanoparticles in living HeLa cells. Our work provides insight into engineering the scattering features by doping elements in nanomaterials, further inspiring us to explore the geometry-independent method for scattering modulation.

Part content of this chapter is from the paper:

L. Ding†, X. Shan†, P. Reece, I. Aharonovich and F. Wang. Controlling Rayleigh scattering from lanthanide ion-doped nanoparticles. (*under review*)

4.1 Limitation of engineering scattering for current strategies

Rayleigh scattering, deviating a light from its straight trajectory, is one of the most important natures of nanoscale objects [94]. It reflects the charge distribution and electric polarizability of the nano-objects under electromagnetic radiation. This intrinsic nature enables the scattering signal to be intense and quenching-free compared with the fluorescence signal, thus facilitating broad applications. The Resonance Rayleigh Scattering (RRS) of metallic nanoparticles has been used for biosensing analytes, including proteins, metal ions, nucleic acids, and insecticides [95]. The scattering saturation of gold nanoparticles provided a fluorescent-free super-resolution microscopy

method [96]. Interferometric scattering microscopy offers a way to track biological transportation events with ultrafast speed (e.g., 66000 fps) [54]. Controlling the random scattering results in an optical cavity for random lasers [97]. Detecting scattering fields from semiconductor nanoparticles have been used to measure its time-resolved carrier dynamics by differential reflectance spectroscopy [98][99][100].

Scattering spectrum features from nanoparticles are generally governed by the electron resonance interaction. Within metallic materials, according to the Drude model[101][102], the excitation beam will trigger the oscillation of free electrons and the resultant plasmon resonance. The resonance frequency and amplitude depend on plasmon resonance mode, electron's effective mass and concentration [101]. In dielectric materials, the electrons are bonded to matrixed ions, and the polarisation of material induced a classic Rayleigh scattering where the scattering cross-section is proportional to the wavelength with the power of -4 ($\sim\lambda^{-4}$).

Recently, tunning scattering spectrum features and intensity from particles show great potential in either nanophotonics or biophotonics, revolutionising the way we confined light. Bound states in the continuum (BICs) have been used to trap and confine the scattered light with a particle size cavity and realised in photonic crystals [103][104], quantum dots [105], and topological insulators [106][107]. Metasurfaces [108] and nanoresonator arrays engineer the scattering by modifying individual repetitive units, benefiting the photonic applications in fundamental physics, lasers, sensors and filters. Controlling the scattering feature from the nanoscale particle is attractive, as the nanoscale size benefits intracellular application. However, according to the plasmon and dielectric resonance theory, the current methods to modify the Rayleigh scattering spectrum for nanoparticles are limited to the morphology controlling [109][110] which complexes the fabrication process. It is highly desirable to find a robust, morphology-uncorrelated method to harness the scattering spectrum from nanoparticles.

The most appealing method to modulate the scattering features is achieved by introducing photo-generated carrier scattering in semiconductor materials. Photon-generated electron-hole pairs in a single nanoparticle could modify the complex refractive index, which in turn changes the scattering spectrum [111]. This modified scattering spectrum has been used to inspect the band structure dynamics in semiconductor nanomaterials [112][99]. The method has recently been used to track the exciton and charge transport in

semiconductors[57]. However, the drawback of the method in turning scattering features is obvious. The modulated scattering signal is considerably smaller than semiconductor nanoparticles' natural scattered signal due to their high refractive index. Methods such as differential reflectance spectroscope [113] and interference are required to extract the modulated scattering feature. Besides, the spectrum modulation range of semiconductors is intrinsically limited to the electronic band structures.

In this chapter, we report a new concept of engineering the scattering features of Rayleigh regime particles by doping the lanthanide element ions in the nanocrystal. The highly doped lanthanide ions can significantly enhance the susceptibility and the consequent polarizability of nanocrystal for the scattering strength under resonant laser illumination [88]. Based on the enhanced resonance, we experimentally demonstrate the feasibility to modulate the scattering features for different types of dopants in nanocrystals, such as Yb^{3+}, Er^{3+} and Nd^{3+}. We develop the interferometric scattering microscopy to record the scattering and further construct the multiplexed iSCAT microscopy for identifying the nanocrystals in living HeLa cells for the first time. Such an efficient biocompatible nanoprobe would benefit scattering-based microscopy methods with the scatting feature immune to changing and aggregation and the biological applications combing the multimodalities of fluorescence [114] and scattering.

4.2 Methods

4.2.1 Sample preparation

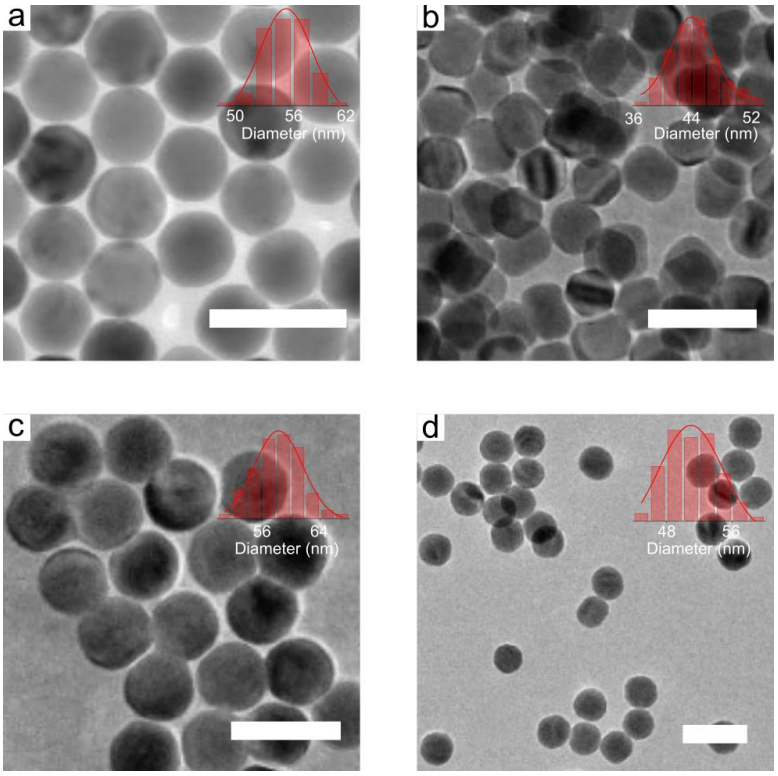

Figure 4-1. TEM images of the Yb-NCs (a), Er-NCs (b), Nd-NCs (c) and Tm-NCs (d). The scale bars are 100 nm.

Synthesis of lanthanide ions doped nanoparticles. Ln-NCs can be synthesised with uniform doping concentration and size. Ln-NCs were synthesized according to the reported method [20]. Typically, 1 mmol $RECl_3 \cdot 6H_2O$ (RE = Y, Yb, Er, and Tm) with the desired molar ratio were added to a flask containing 6 mL OA and 15 mL ODE. The mixture was heated to 160 °C under argon flow for 30 min to obtain a clear solution and then cooled down to about 50 °C, followed by the addition of 5 mL methanol solution of NH_4F (4 mmol) and NaOH (2.5 mmol). After stirring for 30 min, the solution was heated to 80 °C under argon flow for 20 min to expel methanol, and then the solution was further heated to 310 °C for another 90 min. Finally, the reaction solution was cooled down to room temperature. The products were precipitated by ethanol and centrifuged (9000 rpm for 5 min), then washed three times with cyclohexane, ethanol and methanol to get the core nanoparticles. To control the size, nanoparticles grow epitaxially layer-by-layer. The precursors were prepared similarly to the method above. The difference is that the

precursor solution was obtained after keeping for 20 min at 150°C, instead of further heating to 300 °C to trigger nanocrystal growth. For epitaxial growth, 0.15 mmol as prepared core nanoparticles were added to a three-neck flask containing 6 ml oleic acid (OA) and 6 ml 1-octadecene (ODE). The mixture was heated to 170 °C under argon for 30 min, and then further heated to 300 °C. Next, 0.25 ml of prepared shell precursors were injected into the reaction mixture and ripened at 300 °C for 4 min, followed by the same injection and ripening cycles several times to get the nanocrystals with the desired size. Finally, the slurry was cooled down to room temperature and the formed nanoparticles were purified according to the same procedure used for the core nanoparticles. In the work, we synthesized four kinds of Ln-NCs, Yb-NCs ($NaYF_4$: 60%Yb, 2%Er, diameter is 53 nm), Er-NCs ($NaYF_4$: 20%Er@ $NaYF_4$: 20%Er@ $NaYF_4$: 20%Er, diameter is 45 nm), Nd-NCs ($NaYF_4$: 60%Yb, 20%Nd@ $NaYF_4$: 20%Yb, 2%Er@ $NaYF_4$: 40%Nd, diameter is 62 nm) and Tm-NCs ($NaYF_4$: 60%Yb, 2%Tm, diameter is 53 nm).

HeLa cells stained by Ln-NCs.

(1). Ln-NCs were modified with $POEGMEA_{13}$-*b*-$PMEAP_7$ di-block copolymers[115]**.** 10 mg Ln-NCs (Er-NCs and Tm-NCs) and 10 mg $POEGMEA_{13}$-*b*-$PMEAP_7$ di-block copolymers were dissolved in 1 mL THF and then shaken at room temperature overnight. Next, the Ln-NCs coated with di-block copolymers (Ln-NCs@copolymer) were washed with THF three times and then washed with Milli-Q water twice. Finally, the Ln-NCs@copolymer was dispersed in 500 μL Milli-Q water.

(2). Cell culture and staining. The HeLa cells were cultured in Dulbecco's Modified Eagle Medium (DMEM) with supplementation of 10% v/v FBS and 1% v/v penicillin-streptomycin at 37°C and seeded on the fluoro-dish (35 mm) culturing for 24 h. For treatment with Ln-NCs@copolymer, the cells were washed with pre-warmed PBS three times and incubated with Ln-NCs (50 μg/ mL, 1 mL) for 1 h. After 1 h, the cells were washed with pre-warmed PBS. Then 2 mL CO_2-independent medium was added to the dish. Finally, the cell suspension was prepared for iSCAT analysis.

4.2.2 **iSCAT microscopy**

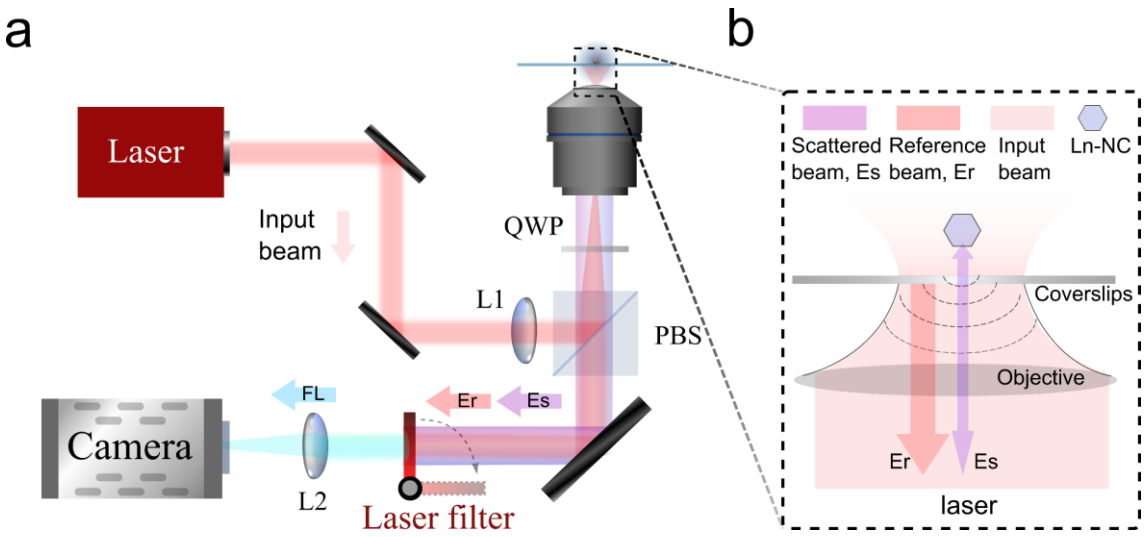

Figure 4-2. (a) Sketch of the iSCAT microscopy system. **(b)** Schematics of iSCAT signal generation.

The iSCAT images of Ln-NCs were recorded by conventional iSCAT microscopy. **Figure 4-2a** shows the experimental setup of the iSCAT microscopy, where the beam from either Ti:sapphire laser or Thorlabs 980 nm laser is focused on the back aperture of the objective lens (×100, NA=1.4) via a polarising beam splitter (PBS, 50/50, Thorlabs) and a quarter-wave plate. The reflected input beam by the coverslip is the reference beam (E_r), and the scattered input beam by the nanoparticle is the scattered beam (E_s). Those two beams will overlap at the camera to create the interference image via the PBS again. The fluorescence mode is controlled by the flip filter before the camera.

4.2.3 **Multiplexed iSCAT (M-iSCAT) microscopy**

Setup of the system.

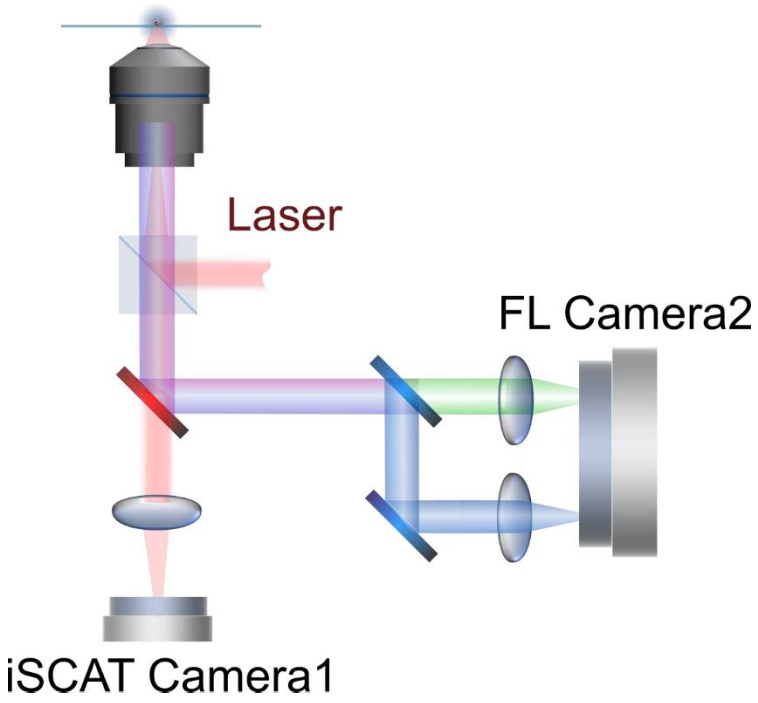

Figure 4-3. Schematic diagram of three-channel M-iSCAT microscopy. The objective lens (×60, NA=1.3, silicon oil) is used.

Figure 4-3 depicts the system setup of the multiplexed iSCAT microscopy. On the typical setup of iSCAT microscopy, we add one dichroic mirror (FF875-Di01-25x36, Semrock) to separate the scattering light and fluorescence light, the two colours (400 to 514 nm for the Tm-fluorescence channel, and 514 to 785 nm for the Er-fluorescence channel) of which from two kinds of Ln-NCs will be further extracted by the second dichroic mirror (Di02-R514-25x36, Semrock). Therefore, we can obtain the images with three-channel information, which benefits the identification of different types of Ln-NCs. It should be noted that the iSCAT channel can be operated under super-fast speed (for example, 66000 fps was reported in the literature [54]) if an ultrahigh-fast camera was used. By contrast, the speed of the FL mode is restricted by the brightness of Ln-NCs, which generally need sub-second level exposure time.

Data acquisition and processing

The conventional iSCAT images of fixed Ln-NCs were obtained by removing the background of raw iSCAT images. The exposure time is 0.1s for FL mode and 0.001s for iSCAT mode (in some cases the exposure time will change according to the brightness and neutral-density filter).

The multiplexed iSCAT data were recorded simultaneously using FL mode and iSCAT mode. For achieving bright enough images, we set the exposure time is 0.1s for FL mode and 0.001s for iSCAT mode. The corresponding frame per second is 10 Hz for FL mode and 240 Hz for iSCAT mode, respectively. The processing method for dynamic iSCAT data was referred to in the literature [52][55].

Calibration of system.

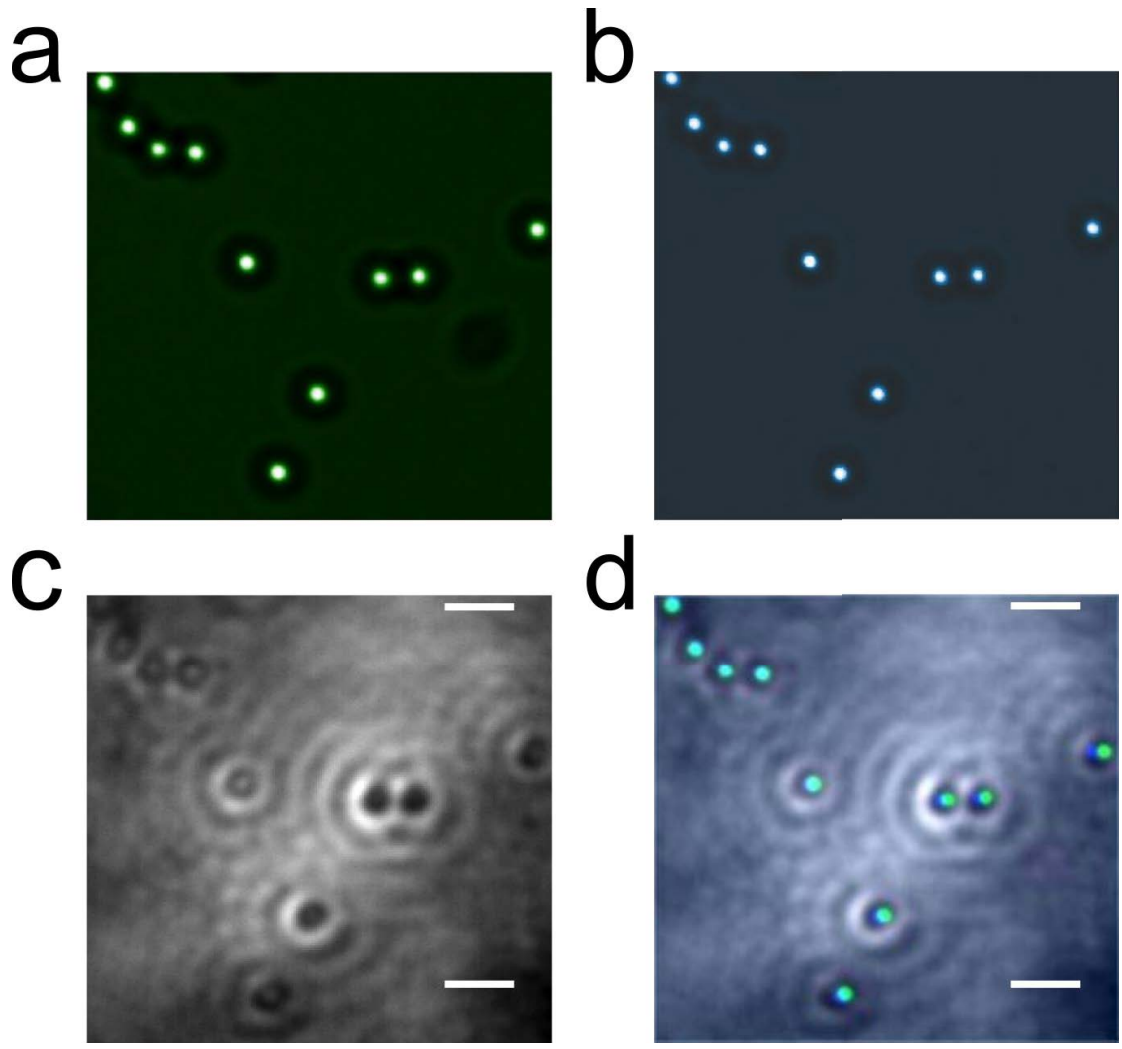

Figure 4-4. Calibration for M-iSCAT system using 1 μm polystyrene sphere. (a) The green-channel image. **(b)** The blue-channel image. **(c)** The iSCAT image. **(d)** The merge of green-channel, blue-channel and iSCAT channel.

We calibrate the coordinates of iSCAT and two-colour FL images by imaging 1μm polystyrene spheres. We first take the image with green-channel (**Figure 4-4a**) and blue-channel (**Figure 4-4b**) information under FL mode, at the same time we record the iSCAT

image (**Figure 4-4c**). And then, we try to match the green channel and blue channel according to the measured ruler (for pixel size). Finally, we overlap the matched FL images with the iSCAT image (**Figure 4-4d**). As shown in Figure 4-4, the three-channel images match well for the following experiments.

Extracting scattering amplitude from iSCAT.

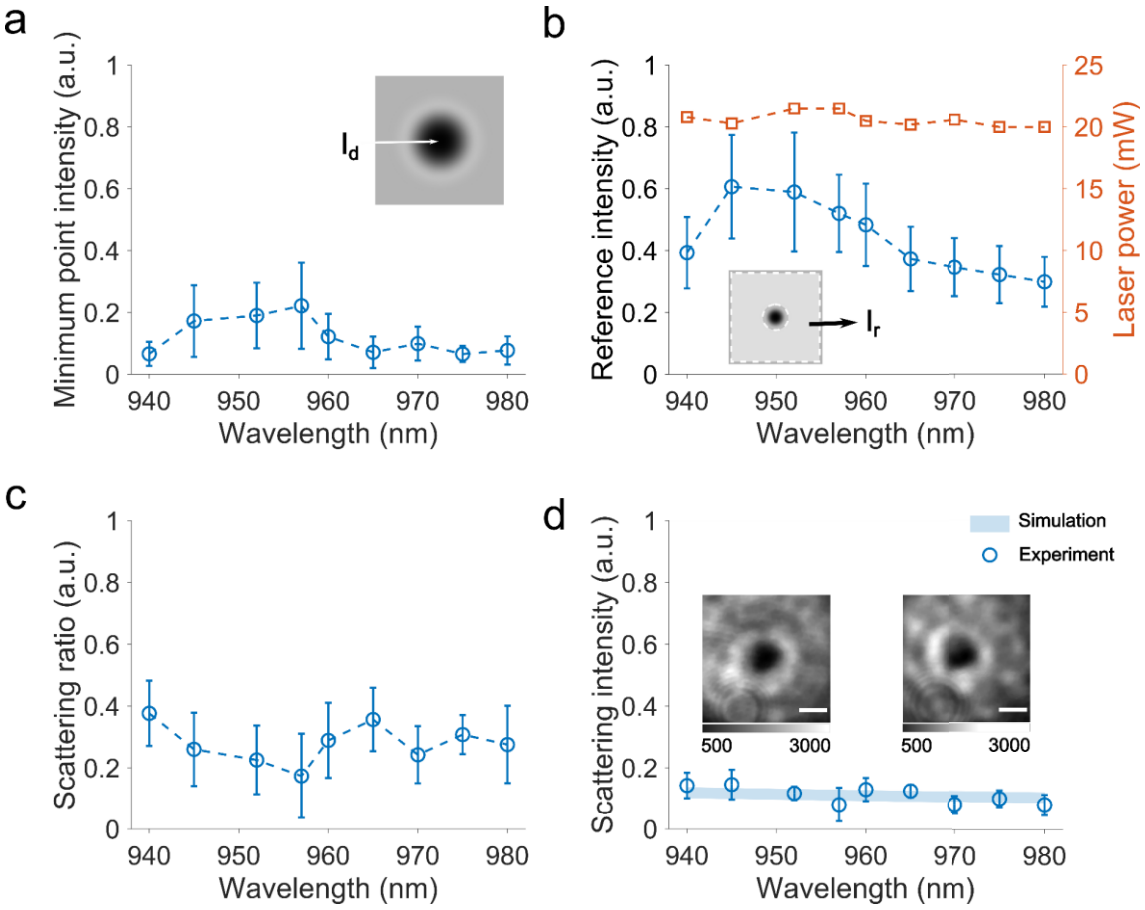

Figure 4-5. Extracting scattering profile from iSCAT images. (a) The normalized detected signal of commercial polystyrene nanosphere with a low refractive index. **(b)** The selection of reference light to calculate the scattering spectrum under different illumination wavelengths. **(c)** The evaluation of scattering ratio (scattering to reference). **(d)** The scattering spectrum of polystyrene nanoparticles. Inset, the background-free images of polystyrene sphere under 940 nm (left) and 980 nm (right) where the background is measured by moving away nanoparticles. The scale bar in the figure is 1 μm.

We demonstrate that the scattering spectrum of nanoparticles can be extracted from a series of iSCAT images with different illumination wavelengths. The detected intensity

(I_d) of the centre of nanoparticles in iSCAT is the interference between the reflected beam ($I_r = {E_r}^2$) and the scattered beam ($I_s = {E_s}^2$), expressed as:

$$I_d(\lambda) = I_r(\lambda) + I_s(\lambda) + 2\sqrt{I_r I_s}cos\varphi \qquad (4-1)$$

where φ is the phase difference between E_r and E_s, consisting of the Gouy phase accumulation, particle-induced phase change and the particle's axial position induced phase change. **Figure 4-5a** shows the experimental measured I_d of a 300 nm polystyrene sphere with excitation wavelength from 940 to 980 nm. Defining the scattering ratio as $\sqrt{I_s/I_r} = C_m$, the equation (4-1) can be solved as:

$$C_m = \pm\sqrt{cos\varphi^2 - (1 - I_d/I_r)} - cos\varphi \qquad (4-2)$$

Figure 4-5b expresses the selection of the $I_r(\lambda)$. In an ideal system that only considers the reflection from the coverslips, the laser power (orange line in Figure 4-5b) would linearly change with $I_r(\lambda)$. However, in a real-world system, the $I_r(\lambda)$ consists of reflections from multiple surfaces (e.g., lens and PBS), which modifies the intensity for different wavelengths according to the phase change. Hence, we integrate and normalise the intensity of each point on the iSCAT image except the particles' region (Figure 3b, inset), to represent the $I_r(\lambda)$. The sum of intensity (blue line in **Figure 4-5b**) shows fluctuation though the input powers are similar for different wavelengths. Here we simplify the $cos\varphi$ to -1, as we make a complete destructive interference by experimental tunning the I_d to the minimum value. This makes the interference most distinct and simultaneously simplifies the data processing. In the case of the scatting signal is smaller than the reflected signal ($I_s < I_r$), the most common cases [116][57][117] in iSCAT, a negative sign should be used in equation (4-2), and the solved scattering ratio is shown in Figure 4-5c. The scattering strength (blue circle in **Figure 4-5d**) is calculated by using C_m to multiple I_r, which is matching with the simulated result by Mie scattering theory (blue shadow in **Figure 3d**). The typical iSCAT images at wavelengths of 940 and 980 nm are shown at the left and right insert figures of Figure 4-5d, respectively, with similar imaging contrast.

4.3 Results and discussion

4.3.1 Simulation for ion resonance enhanced scattering

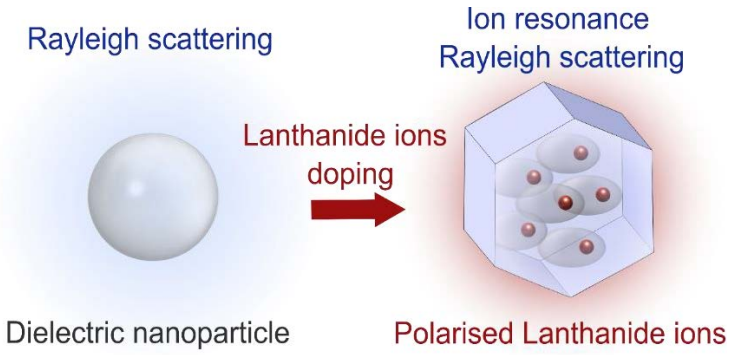

Figure 4-6. Diagram of the resonance effect induced by lanthanide ions doped in nanoparticles under external illumination.

We simulate the scattering process for standard SiO_2 dielectric nanoparticles and lanthanide ions-doped nanocrystals (Ln-NCs) [118][14][119]. Here we select Ln-NC as the model to conduct the ion resonance scattering, as the crystalline host $NaYF_4$ of Ln-NC can be embedded with hundreds of thousands of trivalent lanthanide ions, of which the unique 4f electronic configurations are partially filled and shielded by the outer 5s and 5p electrons, providing a rich energy-level pattern with the adjustable electron-photon interaction and the atomic orbital shielding effect [120]. Under the electromagnetic field of light illumination, these lanthanide ions almost serve as the individual dipoles to interact with incident photons in terms of the optical response and can maintain their atomic resonance (with host crystal field-induced stark levels splitting). This resonance effect in nanoparticles has been used to enhance the trap-stiffness in optical tweezers [88]. The resonance-induced scattering from thousands of ions also increases the nanoparticles' Rayleigh scattering strength when the illumination wavelength matches the resonance of lanthanide ions (**Figure 4-6**). Previous methods to modify the Rayleigh scattering spectrum depend on either morphology modification or carrier generation. To the best of our knowledge, applying ion resonance to modify the Rayleigh scattering spectrum of nanoparticles has not been reported.

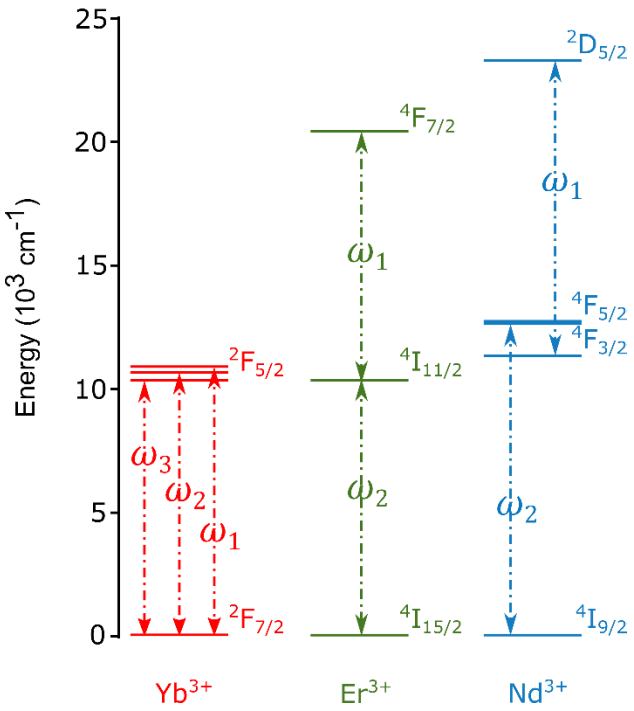

Figure 4-7. Energy level diagrams of Yb^{3+}, Er^{3+} and Nd^{3+} ions in $NaYF_4$ nanocrystal host, where ω *is* the dipole resonance angular frequencies.

The main energy levels of Yb^{3+}, Er^{3+} and Nd^{3+} in the $NaYF_4$ crystals are shown in **Figure 4-7**, which are converted according to nanocrystals' room-temperature absorption curves [121][122][123]. One energy level corresponds to a certain resonance frequency with an energy gap $E_{gap}=\hbar\omega$. The resonance strength is proportional to the population of carriers which are transitioning between the energy gaps.

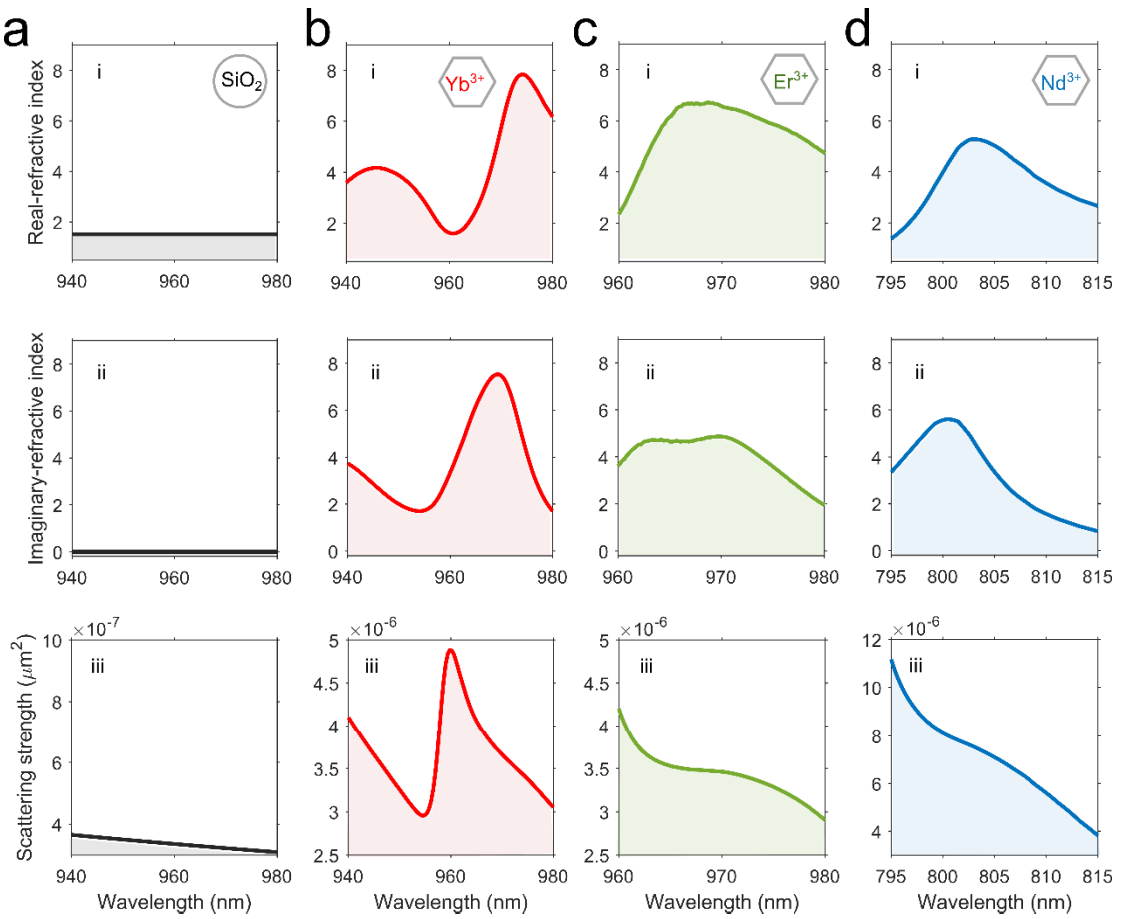

Figure 4-8. Ytterbium, erbium and neodymium doping for enhancing the optical scattering. The numerical modeling of the real part **(i)** and imaginary part **(ii)** of the refractive index, and the scattering cross-section strength **(iii)** for SiO_2 sphere **(c)**, Yb^{3+} **(d)**, Er^{3+} **(e)**, and Nd^{3+} **(f)** doped nanoparticles. The nanoparticles in the simulation are treated as spheres with a radius of 25 nm. The concentration of resonator ions is set as 1.5 nm^{-3} for all three types of Ln-NCs. The surrounding media is air.

According to the Rayleigh approximation [56], the scattering cross-section of a nanoparticle can be expressed as:

$$\boldsymbol{C}_{scat}(\lambda) = \frac{8}{3}\pi k_m^4 a^6 \left|\frac{\varepsilon_p - \varepsilon_m}{\varepsilon_p + 2\cdot\varepsilon_m}\right|^2 \qquad (4-3)$$

where $k_m = 2\pi/\lambda\, n_{\mathrm{m}}$ is the wavenumber within the surrounding medium; n_m is the refractive index of the surrounding medium; a is the radius of the particle; ε_p and ε_m are the permittivity of the particle and the surrounding medium, respectively. The resonance in stark levels of lanthanide ions will provide extra susceptibility beyond the host material, then the ε_p for ions with n stark levels can be expressed as:

$$\varepsilon_p = \varepsilon_0 {n_0}^2 + \sum_{i=1}^{n} \frac{e^2 N}{m(\omega_{0\_i}^2 - \omega^2 + j\sigma_i \omega)} \qquad (4-4)$$

where $\sigma_i = \Delta\nu \cdot 2\pi$ is the damping coefficient, $\omega = 2\pi c/\lambda$ is the excitation angular frequency, ω_{0_i} is the atom resonance angular frequency for level i, ε_0 is the permittivity of free space, m is the effective mass of an electron, N is the number of resonance charges per unit volume, n_0 is the refractive index of the surrounding medium. Hence the real part and imaginary part of the refractive index of the nanoparticle can be calculated by $n_p = real(\sqrt{\varepsilon_p})$ and $k_p = imag(\sqrt{\varepsilon_p})$, respectively. For nanoparticles without nondegenerate energy levels, the N is zero, such as SiO_2 shows a lower refractive index (**Figures 4-8a (i)** and **(ii)**). Benefiting from the ion resonance effect, both the simulated real part (**Figures 4-8 b-d (i)**) and imagery part (**Figure 4-8 b-d (ii)**) of the refractive index from Ln-NCs indicate a much larger amplitude compared with that for SiO_2, though the refractive index of the nanocrystal host $NaYF_4$ is smaller than that for SiO_2. The three adjacent stark levels for Yb^{3+} ions lead to a larger variation with excitation wavelengths. Both Er^{3+} and Nd^{3+} ions have efficient excited-state absorption with transition angular frequency (ω_1) nearly matching with the ground state's transition angular frequency (ω_2), which in turn results in single peaks in their refractive index response.

Substituting equation (4-4) into (4-3) produces the modified scattering cross-section for Ln-NCs. The cross-section can also be represented by the refractive index as:

$$\boldsymbol{C}_{scat}(\lambda) = \frac{8}{3}\pi k_m^4 a^6 \left| \frac{{n_p}^2 - {k_p}^2 - 2ink - {n_m}^2}{{n_p}^2 - {k_p}^2 - 2ink + 2{n_m}^2} \right|^2 \qquad (4-5)$$

$$= \frac{8}{3}\pi k_m^4 a^6 \frac{\left({n_p}^2 + {k_p}^2\right)^2 - 2\left({n_p}^2 - {k_p}^2\right){n_m}^2 + {n_m}^4}{\left({n_p}^2 + {k_p}^2\right)^2 + 2\left({n_p}^2 - {k_p}^2\right){n_m}^2 + 4{n_m}^4} \qquad (4-6)$$

According to equation (4-6), interestingly, the scattering would be stronger when the refractive index (both the real and imaginary parts) is larger, and the amplitude would be even larger when the real part is equal to the imaginary part ($n_p = k_p$). The simulated scattering cross-sections for Ln-NCs (Figure 4-8 e-g(iii)) show that this effect induces strong fluctuation, especially for the Yb^{3+} doped nanoparticles. The ion resonance-enhanced scattering cross-section shows a much larger than the scattering strength of SiO_2 spheres, around 300 times.

4.3.2 **Scattering spectrum of lanthanide-doped nanoparticles**

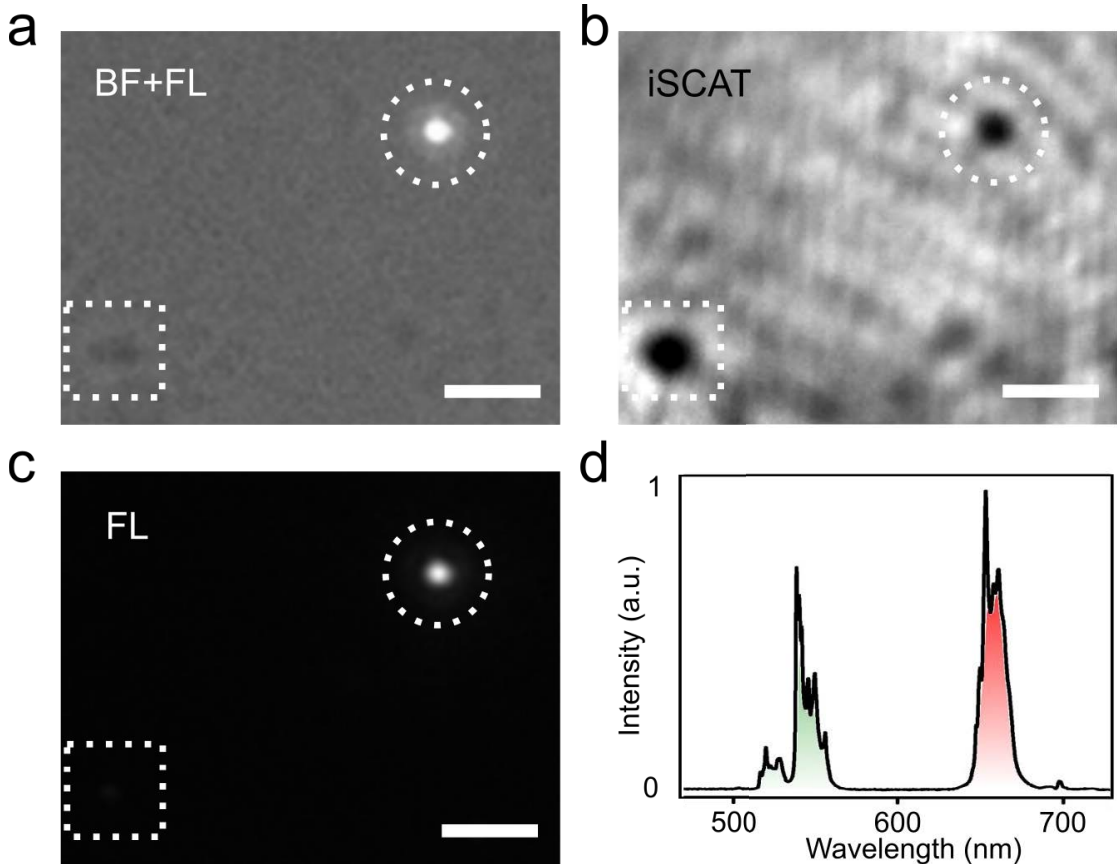

Figure 4-9. Comparison of iSCAT and FL images. (a) The bright-field (BF) image (merged with fluorescence image) of Yb-NCs and impurities. **(b)** The iSCAT images of Yb-NCs and impurities. (**c)** The corresponding fluorescence image (FL). The dotted rectangle points to impurities while the dotted circle represents Yb-NCs. The scale bars are 2 μm. **(d)** The fluorescence spectrum of Yb-NCs under the illumination wavelength of 980 nm.

To estimate the scattering strength of Ln-NCs, we employ an iSCAT microscopy combined with wide-field fluorescence microscopy. The iSCAT microscopy is a fast, label-free imaging technology that has been widely explored in tracking nanoparticles of proteins [117][54][55][52], virus [124][125], cell ingredients [126][127][128], electrode particle [129] and gold nanoparticles [109], and energy flow [57]. In this experiment, we use Yb-NCs which have the typical emission spectrum (for Yb-NCs, Yb^{3+} is the sensitizer while the co-doped Er^{3+} serves as the emitter) as shown in **Figure 4-9d**. **Figure 4-9b** demonstrates a typical iSCAT image of Yb-NCs and impurities that are shown as black dots. Higher contrast of the image (or darker of the black dots) indicates higher scattering strength. We use the in-situ fluorescence mode image (**Figure 4-9c**) to confirm the

location of the Yb-NCs, which is also verified by the merge of bright field and fluorescence images (**Figure 4-9a**).

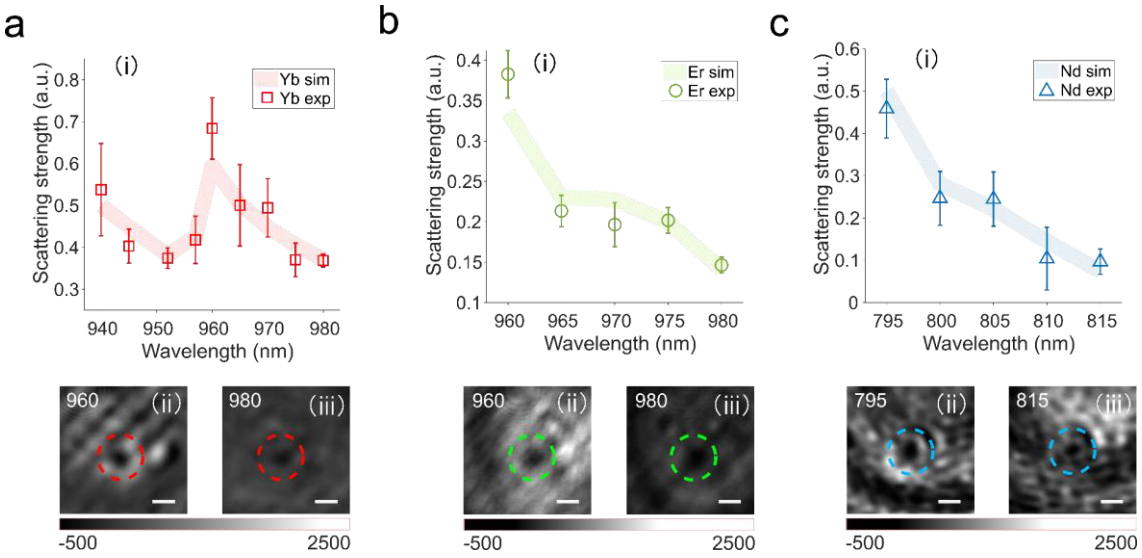

Figure 4-10. Scattering spectrum of Ln-NCs. The scattering features of Yb-NCs (**a-i**), Er-NCs (**b-i**) and Nd-NCs (**c-i**), respectively. The square, circle and triangle with error bars represent the experiment data averaged from at least five measurements. The shadow lines suggest the simulated results. Typical iSCAT images of Ln-NCs under different excitation wavelengths are shown below the corresponding spectrum figure. The Yb-NCs, Er-NCs, and Nd-NCs are labelled by red, green, and blue dotted circles, respectively. The scale bars are 1μm.

To verify the effect of the ion resonant scattering, we extract the scattering spectra of nanoparticles from a series of iSCAT images with different illumination wavelengths. Applying the scattering extraction method, we obtain the ion resonance-enhanced Rayleigh scattering for nanoparticles doped with Yb^{3+}, Er^{3+} and Nd^{3+} ions, respectively. According to **Figure 4-8**, the scattering spectra of Ln-NCs should have distinct fluctuation with respect to the spectrum of polystyrene spheres, as the ion resonance modulates the refractive index. The data points labelled as the square, circle and triangle in **Figures 4-10 a(i)** to **c(i)** are normalized scattering spectra for Yb-NCs, Er-NCs and Nd-NCs, respectively. These spectra are generally matching with the theoretical simulation (shadow lines in **Figures 4-10 a(i)** to **c(i)**), much distinguishable from the scattering feature of low-refractive-index particles such as that for 300 nm polystyrene sphere (**Figure 4-8a**). The amplitude mismatches are attributed to the multi-reflection induced intensity fluctuation. The scattering strength can be directly observed from the visible change in the iSCAT images with a higher signal-to-noise ratio representing stronger scattering strength, though the image background intensity varies with

wavelengths. The iSCAT image of Yb-NCs (**Figure 4-10a(ii)** black dots labelled by red circles) under 960 nm has higher visibility than that under 980 nm (**Figure 4-10 a(iii)**), which indicates a higher scattering strength at 960 nm. Similarly, the iSCAT images of Er-NCs and Nd-NCs show higher visibility at 960 (**Figure 4-10 b(ii)**) and 795 nm (**Figure 4-10 c(ii)**), respectively, than that at 980 (**Figure 4-10 b(iii)**) and 815 nm (**Figure 4-10 c(iii)**). Hence Er^{3+} and Nd^{3+} have higher scattering strength at 960 nm and 795 nm. These iSCAT results match the simulation calculated by equation (4-5). The measurement confirms that changing the dopant of a nanocrystal could effectively engineer its scattering spectrum, and its iSCAT image can be adjusted by changing the illumination wavelength.

4.3.3 Multiplexed iSCAT microscopy for the identification of nanoparticles in living cells

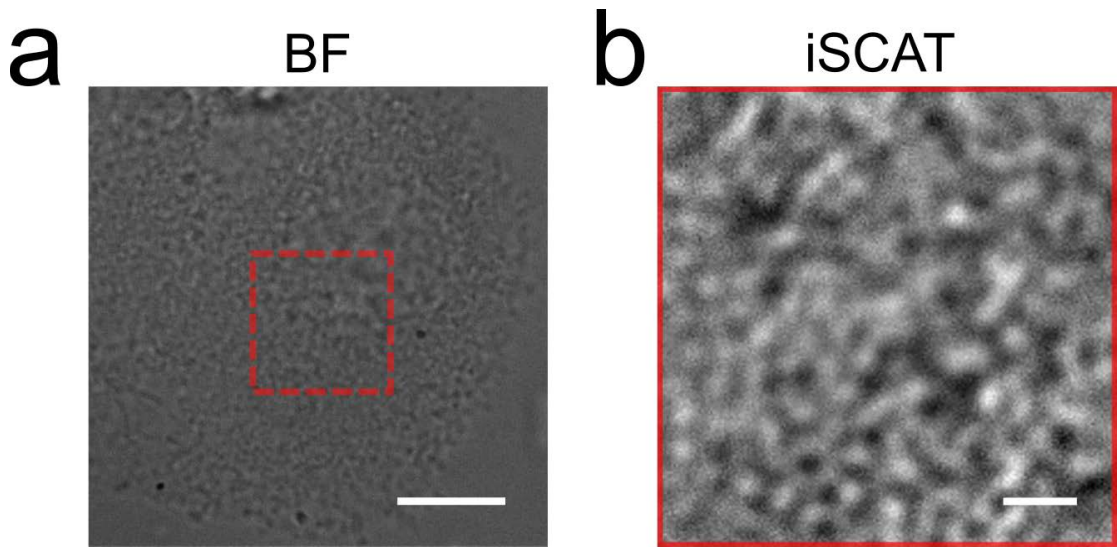

Figure 4-11. Bright field of living HeLa cell (**a**) and the iSCAT image of the red rectangle region in the BF image of HeLa cell (**b**). The scale bars are 10 mm (a) and 2 mm (b), respectively.

This resonance-enhanced scattering of Ln-NCs together with its emission properties could benefit intracellular iSCAT imaging that has challenges in distinguishing different types of particles (e.g., distinguishing nanoprobes with respect to vesica). Indeed, the abundant cellular structures and ingredients significantly increase the difficulties of extracting scattering images of targeting multi-kind particles in living cells. To show the applicability of Ln-NCs as the iSCAT probes, we further demonstrate a multiplexed iSCAT (M-iSCAT) imaging by combining the iSCAT channel with two fluorescence

channels. **Figure 4-3** depicts the system setup of the multiplexed iSCAT microscopy, where Camera 1 and Camera 2 record the conventional iSCAT image and the fluorescence images (FL), respectively. A dual-viewing optical path splits the fluorescence image into blue light (400 to 514 nm for the Tm-fluorescence channel) and green light (wavelength between 514 and 785 nm for the Er-fluorescence channel) on Camera 2. We calibrate the coordinates of iSCAT and two-colour FL images by imaging 1μm polystyrene spheres, which results in images overlapping (**Figure 4-4d**). Thereby, the FL channels can facilitate locating different types of probes on iSCAT images. The method enables multiplexed intracellular iSCAT imaging. The intracellular structures (**Figure 4-11a**) of living cells often generate many background reference points [126] on iSCAT image (**Figure 4-11b**), because of either organelles or localised morphology-induced phase change, which challenges the intracellular particle identification and classification.

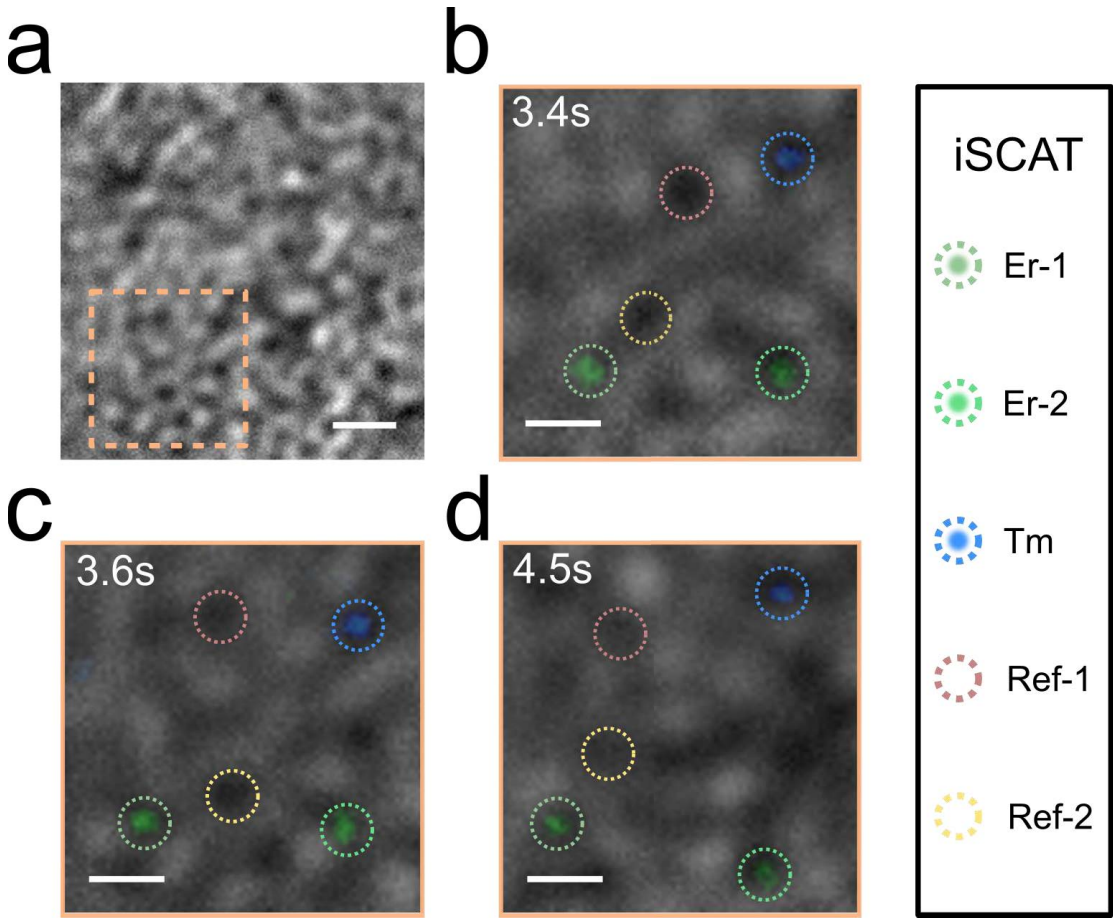

Figure 4-12. (a) iSCAT image of HeLa cell. **(b-d)** M-iSCAT images of the orange square region at 3.4 **(b)**, 3.6 **(c)** and 4.5 **(d)** seconds, in which colorful circles represent different particles as labelled. The Ln-NCs (Er-1, Er-2 and Tm) can be distinguished from reference particles (Ref-1 and Ref-2) by merged fluorescence colors. The scale bars are 2 mm (a) and 1 mm (b-d) respectively.

For instance, Ln-NCs inside a living HeLa cell (**Figure 4-12a**) cannot be distinguished by the conventional iSCAT microscopy. Figure 4-12 b-d shows the M-iSCAT images of the squared area in **Figure 4-12a**, where the Ln-NCs (Er-1, Er-2 and Tm) can be directly visualised and distinguished from biological particles (e.g., Ref 1 and Ref 2) since Tm^{3+} and Er^{3+} doped nanoparticles have blue wavelength band and green wavelength band emission, respectively. The M-iSCAT images at 3.4, 3.6 and 4.5 seconds during dynamic tracking (**Figures 4-12 b-d**) indicate a recognisable position moving of the Ln-NCs.

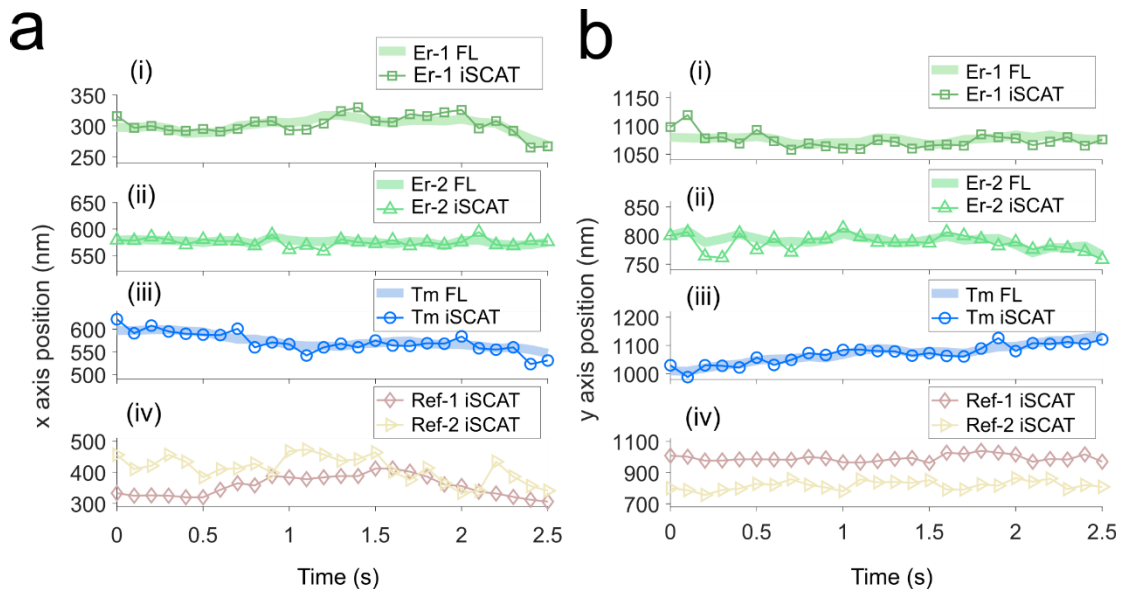

Figure 4-13. Dependency of fluorescence and iSCAT trajectories of five particles within 2.5 seconds on horizontal (**a**) and vertical axises (**b**).

The iSCAT trajectories on both x and y-axis of Ln-NCs (Er-1 iSCAT, Er-2 iSCAT and Tm iSCAT) generally match the FL trajectories, as shown in **Figure 4-13a** and **b**. The offset between the iSCAT and FL trajectories would be due to the different imaging frame rates. The iSCAT imaging frame rate is 240 Hz, while the FL imaging rate is 10 Hz, limited by the fluorescence intensity of nanoparticles. Hence, the FL tends to display accumulated positions. Two reference iSCAT points (Ref-1 and Ref-2 in **Figure 4-12**) reveal significant different trajectories (**Figures 4-13a** and **b**) with Ln-NCs, indicating the dynamics of Ln-NCs are not from large area structural movement.

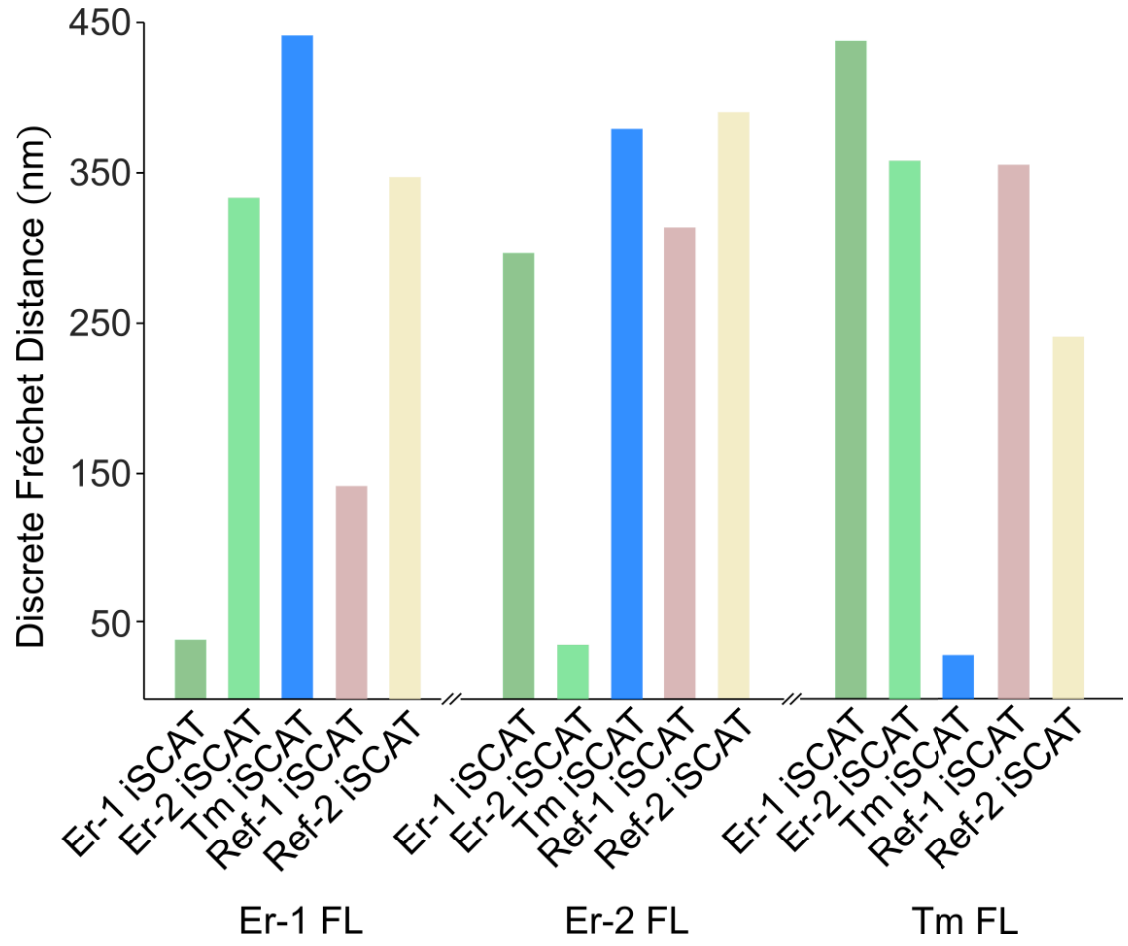

Figure 4-14. Dependency valuation of fluorescence and iSCAT trajectories via Fréchet distance, the radial distance of which is calculated considering both x and y positions.

To quantify the correlation between iSCAT and FL trajectories, we calculate the Fréchet distance [130][131] as shown in **Figure 4-14**, in which a shorter distance means a stronger correlation. The correlation between Er-1 FL and Er-1 iSCAT trajectory shows a Fréchet distance as small as 39 nm, proving that the fluorescence image is from Er-1 in iSCAT image rather than other points. Similarly, the Fréchet distance for Er-2 FL and iSCAT trajectory and Tm FL and iSCAT trajectories are 36 and 29 nm, respectively, indicating the fluorescence positions are well connected with the iSCAT positions.

4.4 Conclusion

We demonstrate a method to engineer the scattering spectrum of nanoparticles by doping the lanthanide ions. We develop the theory to interpret the engineering mechanism and investigate the extraction method of scattering strength from the iSCAT images. Highly doped lanthanide ions benefit the scattering strength of Ln-NC under resonant laser

illumination by enhancing the susceptibility and the consequent polarizability of the particles. Due to the variation of resonant transition from the types of lanthanide ions, we modulate the scattering features of Ln-NCs by changing the dopants. The consistency of experimental and simulated results validates the concept of engineering nanoscale objects' scattering strength.

This method provides a novel geometry-independent path to modulate the scattering features, as most current methods need to modify the shape or size of particles, such as gold nanoparticles, dielectric particles, and semiconductors. Besides, it circumvents the requirement of the second pump laser to excite the particles since the laser serves as both scattering and excitation source in our system. Combining the ion resonance scattering with geometrical resonance engineering, including photonic cavities [103][104] and nanoresonator [132][133][134], may further enrich the freedom of scattering modulation. To our knowledge, for the first time, we demonstrated a multiplexed iSCAT microscopy for intracellular visualising and classifying nanoparticles in living cells. The abundant cellular structures and ingredients significantly increase the difficulties of extracting scattering images of targeting multi-kind particles in living cells. Some progress may be achieved if the experimental condition is further optimized, but it is out of our main purpose in this work. For instance, the imaging frame rate of M-iSCAT can be further improved by using brighter Ln-NCs and a faster camera, together with advanced data processing method to correlate the FL position with iSCAT positions. The imaging channels of M-iSCAT can be further extended by using different types of Ln-NCs. In addition, a scattering based (without the need for an FL image) multiplexed iSCAT could be achieved by using different wavelengths of scattering laser simultaneously since the scattering efficiencies for different types of nanoparticles are different (Figure 4-10). We wish this work could open the door to apply powerful chemical synthesis method for the modification of Rayleigh scattering and the exploration of new probes for scattering based microscopy technologies.

Chapter 5 Break oxygen quenching of triplet-triplet annihilation upconversion in electrode medium

Triplet fusion upconversion (also called triplet-triplet annihilation, TTA) arouses much attention due to its potential in the fields of biological imaging, optogenetics, and light-harvesting. However, the oxygen quenching remains challenging ahead to restrict their applications in aqueous media. Previous efforts to realise the aqueous TTA with oxygen resistance have been focused on the core-shell structures and self-assembly, but tedious processes and complicated chemical modification are required. Here, we report a direct and efficient strategy to realize aqueous TTA by controlling the ionic equilibrium of the TTA dyad. We find that the ionized organic dyad in physiological buffers and electrolyte-based media show natural aerotolerance without any complicated structure engineering. In particular, the upconversion intensity of this aqueous TTA in Tris buffer under air-saturated conditions is more than twice that under the deaerated condition. We further demonstrate the TTA system for potential applications in pH and temperature sensing with reversible and sensitive performance. We anticipate this facile approach to inspire the development of practical aqueous TTA and broad applications in biological science.

Part content of this chapter is from the paper:

L. Ding, J. Zhou*, Q. Fu, G. Bao, Y. Liu and D. Jin. Triplet-fusion Upconversion with Oxygen Resistance in Aqueous Media. Anal. Chem., 2021, 93, 4641–4646.

L. Ding*, Q. Fu*, I. Aharonovich and F. Wang*. Breaking Oxygen Quenching of Triplet–Triplet Annihilation Upconversion by Multidimensional Structures. (to be submitted)

5.1 Challenge of oxygen quenching for TTA

Triplet fusion of organic molecules triggers numerous interests in catalysis [7], bioimaging [135], and light-harvesting [136][137] due to the spectral conversion feature from low to high energy frequencies. It enables low power excitation condition [138], high upconversion efficiency [139][140], and flexible design of plat-forms [141][142][143][144][145] based on organic TTA dyad, donor and acceptor. But the

solution-based TTA systems are restricted to organic solvents without oxygen molecules because of the intrinsic hydrophobicity of organic dyad and oxygen quenching, although the applications in aqueous media are attractive.

The dioxygen with a triplet ground state consumes the energy of the donor triplets to become singlet oxygen, which will further damage the organic TTA dyad by oxidation. Additional treatments are thus required to isolate them with ambient oxygen molecules in aqueous media. Nano/micro-capsules and self-assembly [146][147] are common strategies to overcome this challenge. The component, such as surfactant[148][149], polymer [150][151], silica [152][153], and bovine serum albumin (BSA) [3], envelopes TTA dyads to form a dispersible and oxygen-resistant core-shell structure or a tight network in aqueous solutions. Besides, small molecules of antioxidant additive [154] and specific acceptors [26] with lower triplet energy than oxygen are also leveraged to suppress the quenching effect of oxygen. However, these indirect strategies induce tedious engineering steps for wrapping and complicated modification.

Here we describe a facile and direct method that can brighten the dark TTA in aqueous media with oxygen. We realize the water-soluble TTA by controlling the ionic equilibrium of the TTA dyad. We find that this TTA system, instead of forming nano/micro-capsule, can remain the upconversion luminescence in air-saturated aqueous media. Moreover, in selective physiological buffers, the TTA upconversion outperforms that under oxygen-deprived conditions. We further explore the potential of this TTA system as a pH and temperature sensor. Our work represents a record situation that realizes stable TTA in an aqueous solution where oxygen is inevitable and sensitive sensing is achievable.

5.2 Methods

5.2.1 Synthesis of Pd(II) meso-Tetra(4-carboxyphenyl)porphine (PdTCPP)

Synthesis of H_2TCPP.

H_2TCPP was synthesized according to the previous paper with modified[155]. H_2TMPP (420 mg, 0.496 mmol) was dissolved in the mixture solvent of THF (20 mL) and methanol (20 mL), followed by adding 20 mL of aqueous KOH (1.35 g). After refluxing for 24 h, the mixture was cooled to room temperature. Before evaporating THF and MeOH, the mixture was filtered with a filter paper. Additional water was added and filtered by the

filter paper again. Then the solution was acidified with 1 M HCl until pH 2 (could be more). After washing with water, aqueous KOH was added to dissolve the precipitate, followed by pH adjusting. And then the precipitate was washed, collected by centrifugation, and dried under vacuum. ^{1}H NMR (500MHz, DMSO-d_6): δ 13.27 (s, 4H), 8.86 (s, 8H), 8.38 (ddd, 16H), -2.95 (s, 2H)

Synthesis of PdTCPP.

PdTCPP was synthesized according to the previous paper with modified [156]. H_2TCPP (200 mg, 0.253 mmol) and palladium chloride (83.75 mg, 0.572 mmol) were refluxed in the mixture of dimethyl formamide (DMF) (20 ml) and ethanol (5 mL) overnight. The purification of PdTCPP was performed by repeated recrystallization and precipitation from DMF/H_2O solutions. ^{1}H NMR spectrum (500MHz, DMSO-d_6): δ 13.27 (s, 4H), δ 8.80 (s, 8H), δ 8.32 (ddd, 16H).

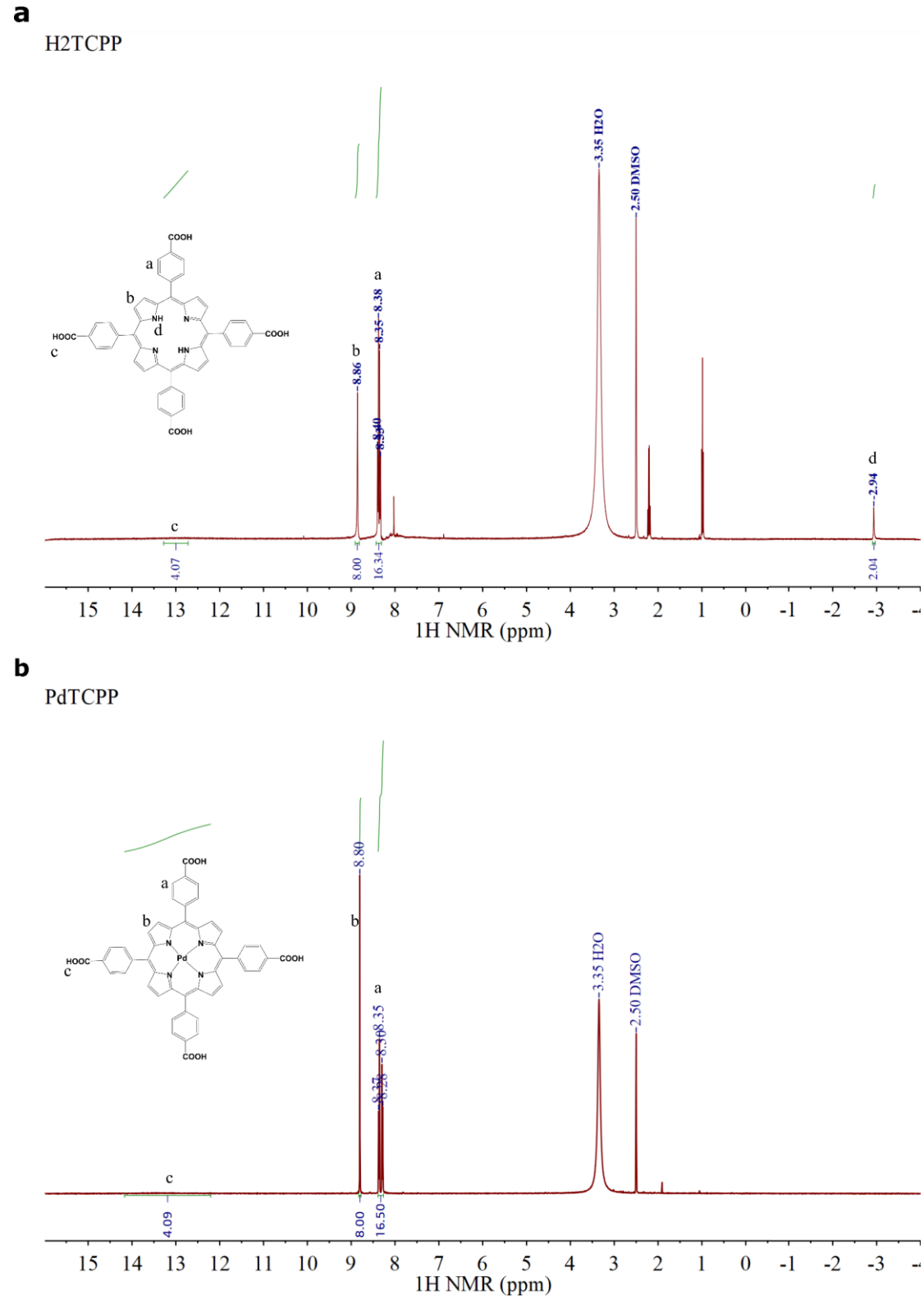

Figure 5-1. ^{1}H NMR of (a) H_2TCPP and (b) PdTCPP.

5.2.2 **Upconversion sample information**

Table 5-1. Feeding ratio of different aqueous/organic TTA samples.

Sample	PdTCPP stock/uL	QCDPA stock/uL	solvent	
			name	Volume/uL
TTA-201	20	40	Mili Q water	940
TTA-501	20	100	Mili Q water	880
TTA-1001	20	200	Mili Q water	780
TTA-501:1M KOH	20	100	1M KOH	880
TTA-501:2M KOH	20	100	2M KOH	880
TTA-501:PBS	20	100	PBS	880
TTA-501:Tris	20	100	TRIS	880
TTA-506	20	100	PBS-KH_2PO_4[a]	880
TTA-507	20	100	PBS-Na_2HPO_4[b]	880
TTA-508	20	100	PBS-NaCl[c]	880
TTA-509	20	100	KCl	880
TTA-5010	20	100	NH_4Cl	880
TTA-21’	20	2	DMF	978
TTA-23’	20	40		940
TTA-24’	20	100		880
TTA-25’	20	200		780
TTA-26’	20	400		580

Superscripts of a, b and c represent the concentration of individuals equaling to that in PBS, 1.06 mM, 2.97 mM and 155.17 mM, respectively.

Table 5-2. Aqueous TTA samples with different kinds of electrolytes.

Electrolytes	Sample	PdTCPP stock/uL	QCDPA stock/uL	Solvent	
				name	Volume/uL
Basic salt	TTA-5061	20	100	KH_2PO_4-0.5M	880
	TTA-5062	20	100	KH_2PO_4-0.1M	880
	TTA-5063	20	100	KH_2PO_4-10mM	880
	TTA-5065	20	100	KH_2PO_4-0.1mM	880
Acid salt	TTA-50101	20	100	NH_4Cl-0.5M	880
	TTA-50102	20	100	NH_4Cl-0.1mM	880
	TTA-50103	20	100	NH_4Cl-10mM	880
	TTA-50105	20	100	NH_4Cl-0.1mM	880
Neutral salt	TTA-5081	20	100	NaCl-1M	880
	TTA-5082	20	100	NaCl-0.5M	880
	TTA-5083	20	100	NaCl-0.1mM	880
	TTA-5084	20	100	NaCl-10mM	880
	TTA-5085	20	100	NaCl-0.1mM	880

5.2.3 **Spectral characterization**

Absorption spectra were measured with an Agilent Cary 60 UV−vis spectrophotometer. pH is determined by an Oakton pH 700 benchtop meter. Fluorescence spectra were recorded on a Shimadzu RF 6000 fluorimeter with a xenon lamp. Upconversion fluorescence spectra were measured with a home-built optical system. A fibre-coupled 532 nm (Germ 532 with control software) diode laser worked as the excitation source. The emission spectra of the sample were measured by a commercial spectrometer

(Shamrock 193i, Andor) with an EMCCD (iXon Ultra 888, Andor) as the detector. Besides, the emission signal was filtered by a 532 short-pass filter (BSP01-532R-25 532 nm EdgeBasic, Semrock) or 561 nm long-pass filter (BLP02-561R-25 561 nm EdgeBasic, Semrock). The sample is in a cuvette (i-Quip, 45 mm × 12.5 mm × 12.5 mm, light length of 10 mm, light width of 5 mm) sealed with N2.

5.3 Results and discussion

5.3.1 TTA upconversion from organic solvent to water

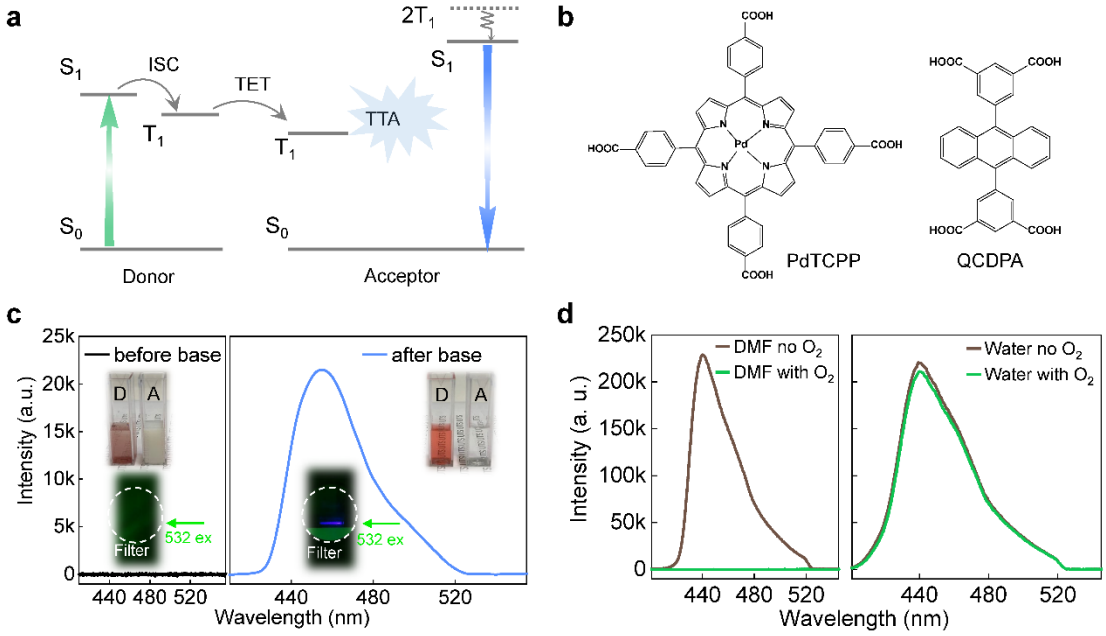

Figure 5-2. TTA upconversion mechanism and TTA generation with oxygen resistance in aqueous media. (a) The energy level diagram showing the triplet fusion upconversion followed by the intersystem crossing (ISC) and triplet energy transfer (TET) processes in the pair of donor and acceptor. (b) The molecular structure of PdTCPP (donor) and QCDPA (acceptor). (c) The upconversion spectra of the TTA before (left) and after (right) adding base upon 532 nm laser excitation (52 mW cm^{-2}). Insets show the insoluble and soluble statues of the donor and acceptor molecules in water, and the snapshots behind the 532 nm short-pass edge filter (BSP01-532R-25, Semrock) under excitation of a 532 nm laser pen. D means donor, and A represents acceptor. (d) The spectra of TTA in DMF (left) and water (right), the concentrations of acceptor and donor are 5 mM and 0.1 mM, respectively. The excitation power density is 61 mW cm^{-2}.

We take Pd(II) meso-Tetra(4-carboxyphenyl)porphine (PdTCPP) as the donor and 5,5'-(9,10-anthracenediyl)diisophthalic acid (QCDPA) as the acceptor (**Figure 5-1** and **Figure 5-2**). Figure 5-2a shows the energy transfer mechanism of triplet fusion, in which the donor transfers the triplet energy to an acceptor on the ground state after light stimulation (532 nm) and intersystem crossing (ISC) [7]. The collision of the excited acceptor triplets produces upconverted blue emission in higher energy wavelengths. In organic solvents,

e.g., DMF, the high solubility makes a quick molecule diffusion of donor and acceptor, resulting in the high intensity of upconverting luminescence (**Figure 5-2d**). But it fails to produce upconversion in water due to the hydrophobicity of the dyad, in which precipitate and turbid solution are observed for the donor and acceptor in water (**Figure 5-2c**, left). After adding the base, both the donor and acceptor solutions became soluble and transparent. The corresponding mixture results in blue upconversion emission centred at 455 nm upon the 532 nm laser excitation (**Figure 5-2c**, right). This base-induced property transformation is modulated *via* ionic equilibrium of the carboxyl groups on TTA dyad.

To quantify the effect of the solution-phase transfer on TTA, we compare the upconversion emission intensities in DMF and water. When the oxygen has purposely been removed from the solution, the upconversion intensity in water is comparable to that in DMF (**Figure 5-2d**). Strikingly, at the atmospheric environment with oxygen, the water-soluble TTA displays neglectable quenching, indicating the strong oxygen resistance of the ionized TTA dyad (**Figure 5-2d**, right), while completely quenching is observed in the air-saturated DMF (**Figure 5-2d**, left). As a simple TTA dyad that can realize high retention of upconversion emission with an oxygen atmosphere but not rely on micro/nano-capsules, it provides the potential of applicable media, such as biological buffers and media with electrolytes.

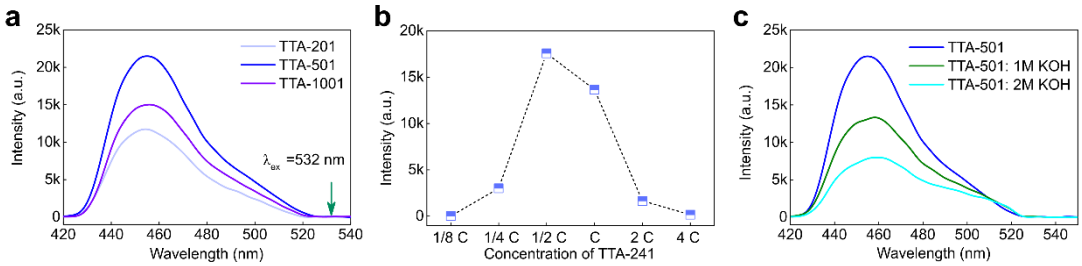

Figure 5-3. (**a**) The upconversion intensity varying with the concentration of TTA-501 in water. The concentration of 1C means 0.1 mM for the donor and 5 mM for the acceptor. (**b**) The upconversion intensity varying with the concentration of TTA-501 in water. The concentration of 1C means 0.1 mM for the donor and 5 mM for the acceptor. (**c**) Upconversion emission intensity changes with the concentration of KOH.

We then optimize the experimental conditions by regulating the ratios of the donor to the acceptor (**Figure 5-3a**). Obviously, the increasing amount of donor can benefit the upconversion process from the ratio of 1:100 to 1:50. But too much donor has an adverse effect on the upconversion luminescence due to the concentration quenching (1:20). The concentrations of dyads (**Figure 5-3b**) and base concentration used for the sample

(**Figure 5-3c**) also affect the TTA upconversion as the luminescence intensity increases with the decrease of base concentration.

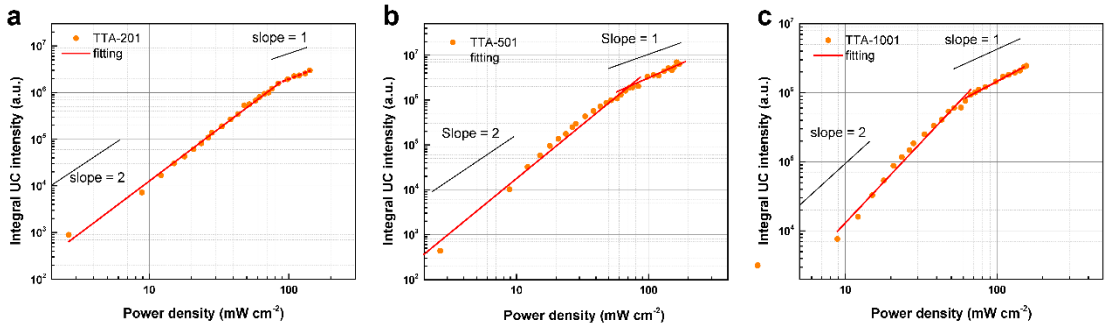

Figure 5-4. Double log plot of the power-dependent emission intensity of the TTA systems with low (a), medium (b) and high (c) mole ratio of the donor and acceptor showing the slope change from quadratic to linear.

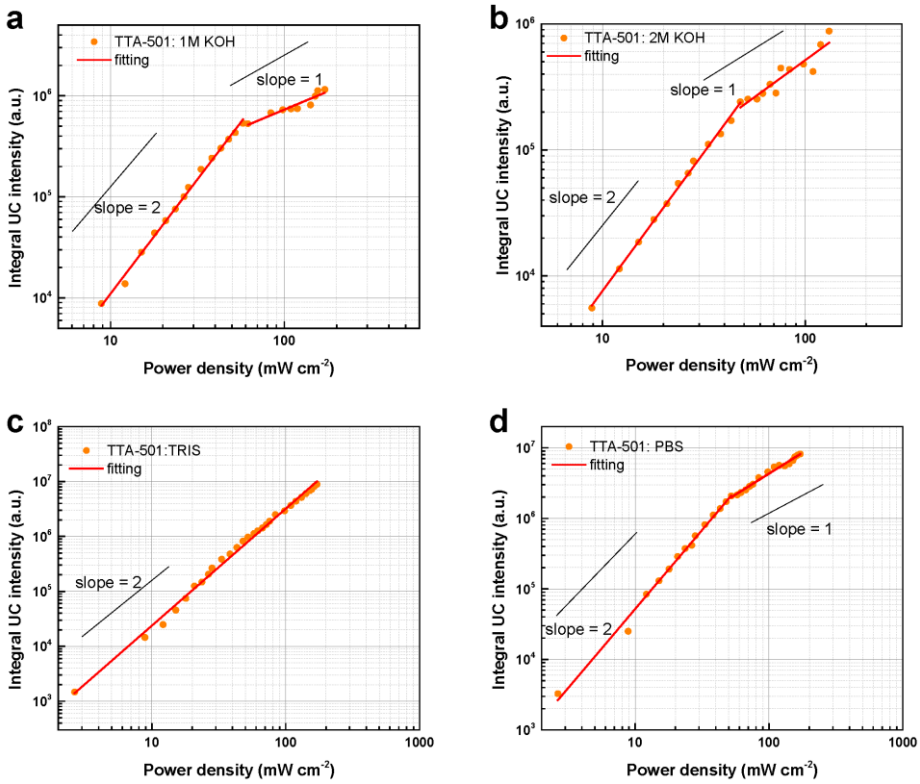

Figure 5-5. Double log plot of the power-dependent emission intensity of the samples in different media of 1 M KOH (a), 2 M KOH (b), TRIS (c) and PBS (d), respectively.

To demonstrate the TTA process of our sample, we measure the relationship between upconversion emission and excitation power. The remarkable feature of TTA kinetics as a function of excitation power density confirms the nonlinear process of this aqueous TTA (**Figures 5-4** and **5-5**), which shows an initial quadratic dependence before

saturation [3][157]. This relationship is also valid for the TTA systems in the buffer solution.

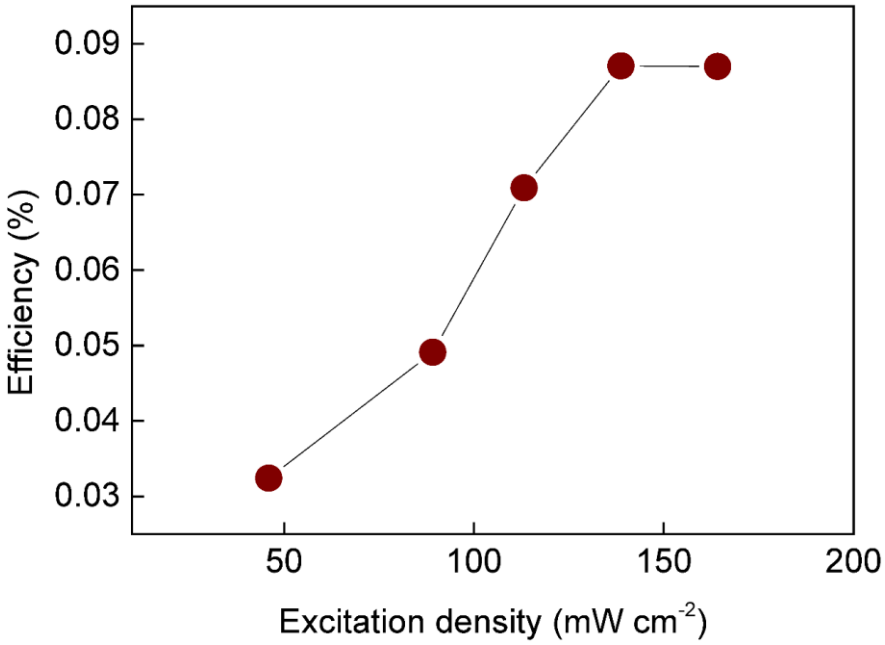

Figure 5-6. Upconversion efficiency under different excitation power densities. $Ru(bpy)_3Cl_2$ in water was used as a standard reference (absolute quantum efficiency $\Phi = 0.042$ in aerated H_2O)[158]. The TTA-UC quantum efficiency (Φ_{UC}) was calculated with the equation $\Phi_{UC} = 2\Phi_{UC}(A_{Ref}/A)(I/I_{Ref})(\eta/\eta_{Ref})$, where A is the absorption at 532 nm, I is the emission intensity, η is the refraction of the medium. The multiplicative factor of 2 was reflected to represent the TTA mechanism (bimolecular process).

We measure the TTA upconversion efficiency under different excitation power (**Figure 5-6**), the efficiency reaches 0.1% in an aqueous solution at 138.7 mW cm^{-2}. Much higher upconversion efficiency is expected to be achieved from the optimized base and dyad types.

5.3.2 TTA performance in air-saturated media

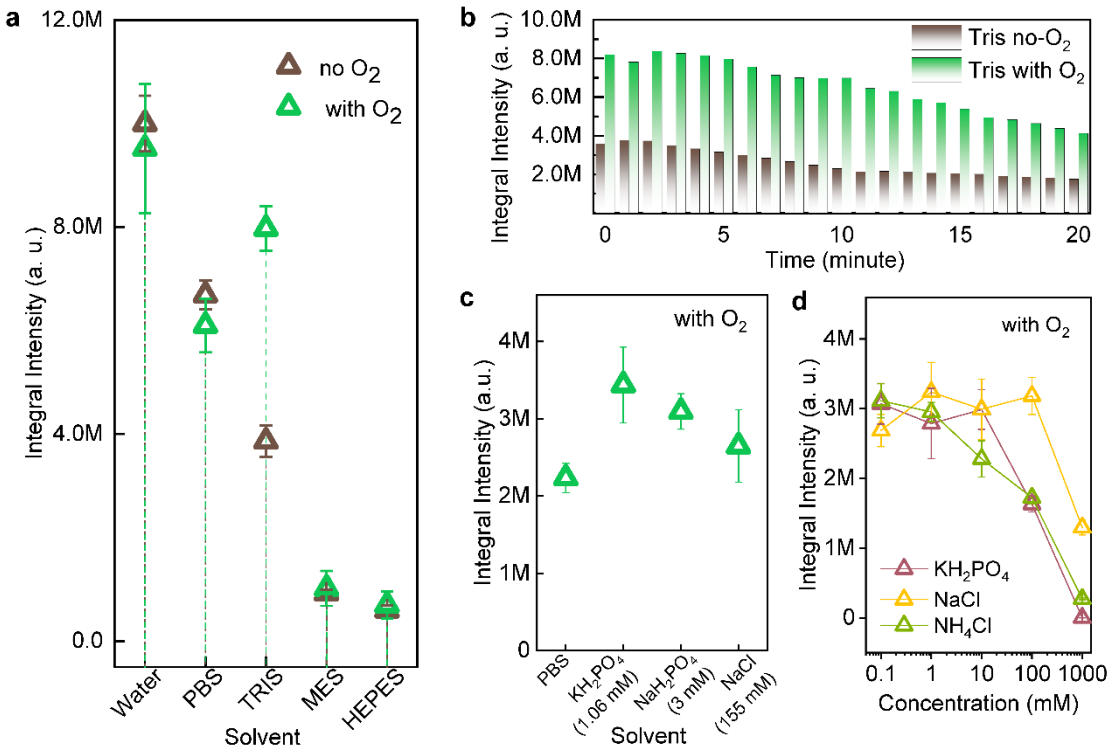

Figure 5-7. TTA performance in aqueous media. (a) The effect of physiology buffers on the upconversion emission. (b) The durability of TTA in Tris buffer with and without oxygen under 532 nm laser irradiation. (c) The evolution of upconversion intensity in a single-electrolyte medium corresponding to PBS components. (d) The influence of electrolyte concentration on TTA process in the air-saturated conditions. The concentrations of acceptor and donor are 5 mM and 0.1 mM, respectively. The excitation power density is 61 mW cm^{-2}.

To broaden the range of applicable media, we test the performance of this aqueous TTA in physiological buffers. Taking the optimized acceptor-donor ratio of 501 as an example, we observe large variations of upconversion intensities in four types of commonly used physiological buffers (**Figure 5-7a**). In Tris buffer, we surprisingly find that the oxygen facilitates the upconverting process by showing enhanced intensity up to twice that in deaerated conditions, as well as the appreciable photostability (**Figure 5-7b**). By contrast, in PBS, MES and HEPES, the oxygen barely affects the upconversion performance. It can be concluded that the buffer ingredients determine the upconversion intensity, as a different degree of quenching is observed in these buffers under deaerated conditions. The nearly complete quenching in MES and HEPES is due to the significantly suppressed solubility of TTA dyad by the sulfonic acid group from the buffer ingredients.

The influence from the buffer ingredients inspires us to further investigate the upconversion evolution by placing the TTA in electrolyte media, which serve as typical components of a buffer. We prepare single-electrolyte-based media with the concentration corresponding to the ingredients of PBS. As the multi-component buffer involves complex ionization equilibrium, the resultant ions will interfere with the dissolution of TTA dyad and consequently damage the overall upconverting process. In **Figure 5-7c**, we find that TTA in a single-electrolyte-based medium outperforms that in PBS buffer.

The tradeoff between the dissolution of TTA dyads and the quenching effect is related to the amount of hydroxyl ions and determines the upconversion process, which is controlled by the ionization equilibrium in a medium. Therefore, careful selection of electrolytes and their concentrations is highly recommended when applying the TTA system in a buffer environment. Here we quantify the ionization effect by tuning the concentration of three representative kinds of electrolytes, basic salt (KH_2PO_4), neutral salt (NaCl) and acid salt (NH_4Cl) (**Figure 5-7d**).

The results show that dilute concentrations of all the salts make the upconversion intensity stable while high concentration conditions quench the luminescence. The concentration thresholds for KH_2PO_4, NaCl, NH_4Cl are 10 mM, 100 mM, and 1 mM, respectively in our experimental condition. We find the products of electrolysis in a solution play a key role in determining the TTA upconversion performance. For neutral salt, NaCl can ionize completely into Na^+ and Cl^-. By contrast, for both basic salt and acid salt, their electrolyzations depend on concentration, according to the following equations (5-1) to (5-5):

$$KH_2PO_4 \rightleftharpoons K^- + H_2PO_4^- \quad (5-1)$$

$$H_2PO_4^- + OH^- \rightleftharpoons HPO_4^{2-} + H_2O \quad (5-2)$$

$$HPO_4^{2-} + OH^- \rightleftharpoons PO_4^{3-} + H_2O \quad (5-3)$$

$$NH_4Cl \rightleftharpoons Cl^- + NH_4^+ \quad (5-4)$$

$$NH_4^+ + OH^- \rightleftharpoons NH_3 \cdot H_2O \quad (5-5)$$

Electrolyzation (equations 5-1 and 5-4) firstly facilitate the dissolution of these electrolytes in water. After that, the hydroxyl ions in the solution will be immediately consumed by $H_2PO_4^-$, HPO_4^{2-} and NH_4^+ (equation 5-2, 5-3 and 5-5). In the low concentration regime, the reduction of OH^- quenching for TTA upconversion dominates the contribution over the less dissolution of TTA dyads resulting from the consumption of OH^-. The electrolyte ions accelerate the diffusion of donor and acceptor and benefit the collision probability for stronger TTA upconversion. In the high concentration regime, the dissolution of TTA dayd is suppressed by excessively consuming OH^- (equation 5-2, 5-3 and 5-5), leading to less molecular diffusion of donor and acceptor and resulting in weaker TTA upconversion.

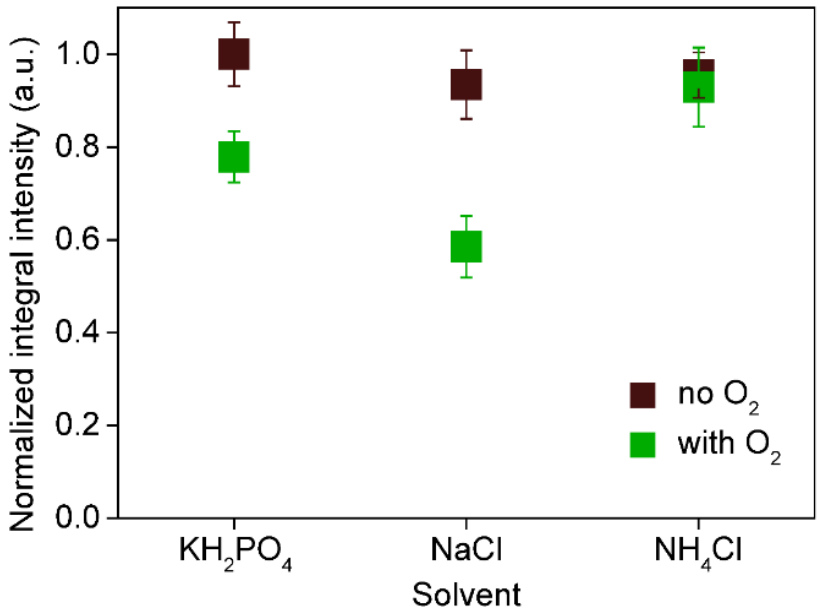

Figure 5-7. Influence of three kinds of electrolyte solutions on the upconversion emission with/without oxygen.

Oxygen has a slightly negative effect on the TTA intensities in the media of electrolytes (**Figure 5-8**). But the decrement of intensity is not as significant as that in DMF (**Figure 5-2d**). In particular, the TTA intensities in deaerated and aerated NH_4Cl solution are the same, indicating strong oxygen resistance.

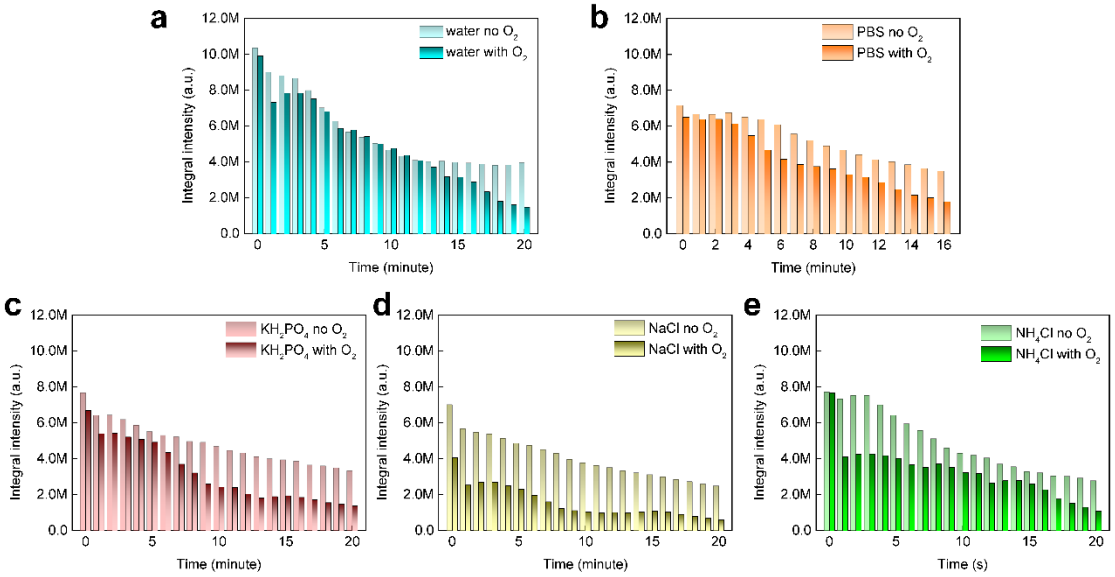

Figure 5-8. The durability of TTA in the solution of (a) water, (b) PBS buffer, (c) KH_2PO_4, (d) NaCl and (e) NH_4Cl with and without oxygen under 532 nm laser irradiation.

We test the photostability in solutions of electrolytes and find that the TTA intensities in the media of water, PBS buffer and electrolytes remain good retention after 20 minutes, especially under the condition without oxygen (**Figure 5-9**).

5.3.3 **Potential in pH and temperature sensing**

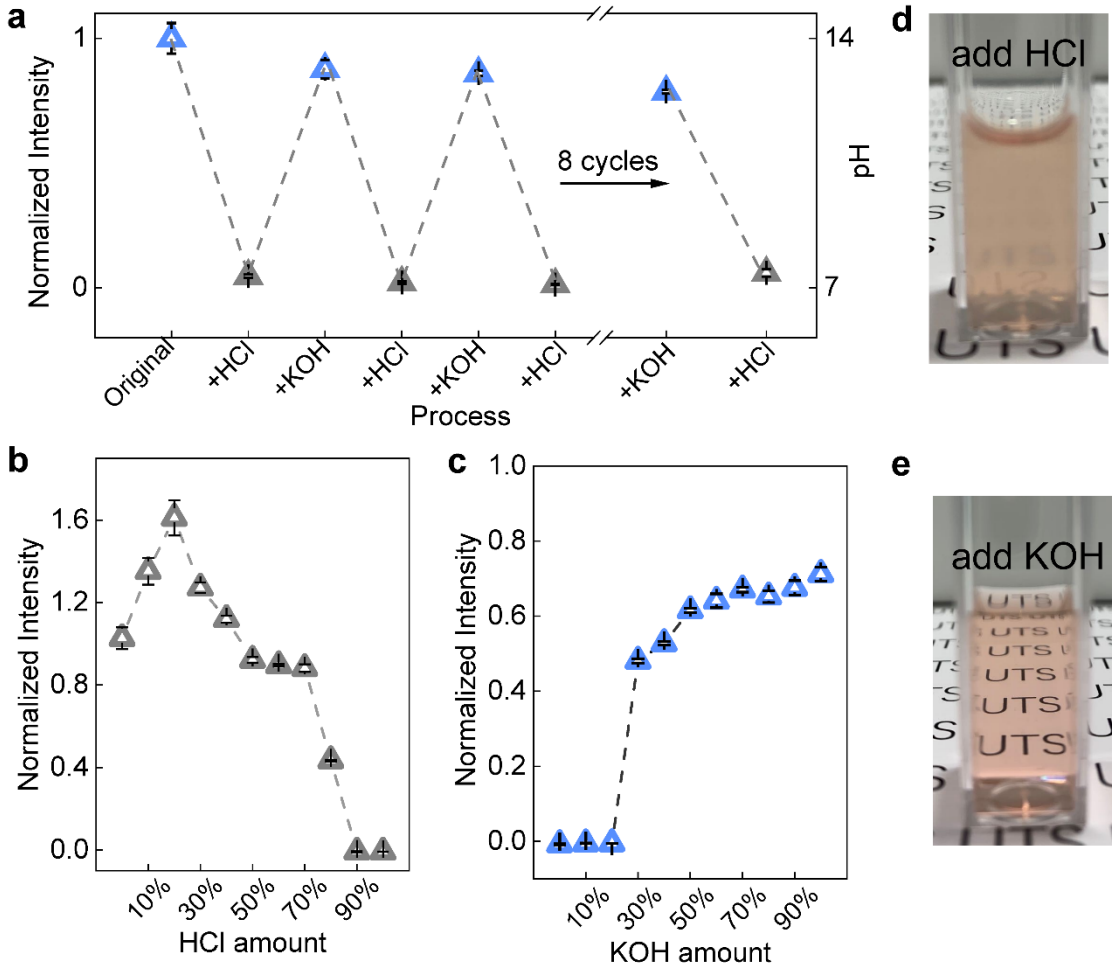

Figure 5-9. Aqueous TTA systems applied as pH sensors. (a) Reversibility of TTA as a pH sensor via adding HCl (1 M) and KOH (1 M) solution. (b) The decreased upconversion emission intensity evolution against the gradient adding of HCl (1 M). (c) The increasing trend of upconversion intensity via gradient adding of KOH (1 M). The error bars in a, b and c indicate the standard deviation of three measurements. The concentrations of acceptor and donor are 5 mM and 0.1 mM, respectively. The samples were tested under air-saturated conditions. The excitation power density is 61 mW cm^{-2}. Digital photos of TTA-501 (1M KOH) with HCl (d) and recovered state by KOH (e).

This upconversion performance is demonstrated to be related to the hydroxyl ions, indicating that the TTA system could be very sensitive to pH. To validate the pH-sensitive property, we design the procedure by alternately adding acid and base into a TTA system to check the possible pH-sensitive property. As shown in **Figure 5-10a**, the upconversion of the alkali TTA system completely disappears after adding HCl, and the pH of the final solution becomes close to 7. The intensity of upconversion almost recovers at the initial adding of KOH, and remains nearly 80% even after 11 cycles, indicating excellent

reversibility. To visualize the dynamic variations of upconversion in a single cycle, we divide and add ten units of acid (**Figure 5-10b**) and base (**Figure 5-10c**) in the TTA systems gradually. The upconversion intensity becomes weak before 7 units of acid adding, followed by a quick reduction until its complete disappearance (**Figure 5-10b**). Compared with the trend of fluorescence quenching by acid adding, the recovery tendency of the upconversion intensity by base adding was almost symmetric (**Figure 5-10c**), accompanied by the solution status changes from being vague and even precipitate to transparent (**Figure 5-10 d** and **e**). Noticeably, the large increase of upconversion in the initial regime of adding acid is speculated to the contribution of diluted concentration of TTA sample (**Figure 5-10b**), as the emission intensity increases with the concentration reducing (**Figure 5-3b**). This implies the transform of TTA dyads forms occurring at the narrow window of acid/base amount.

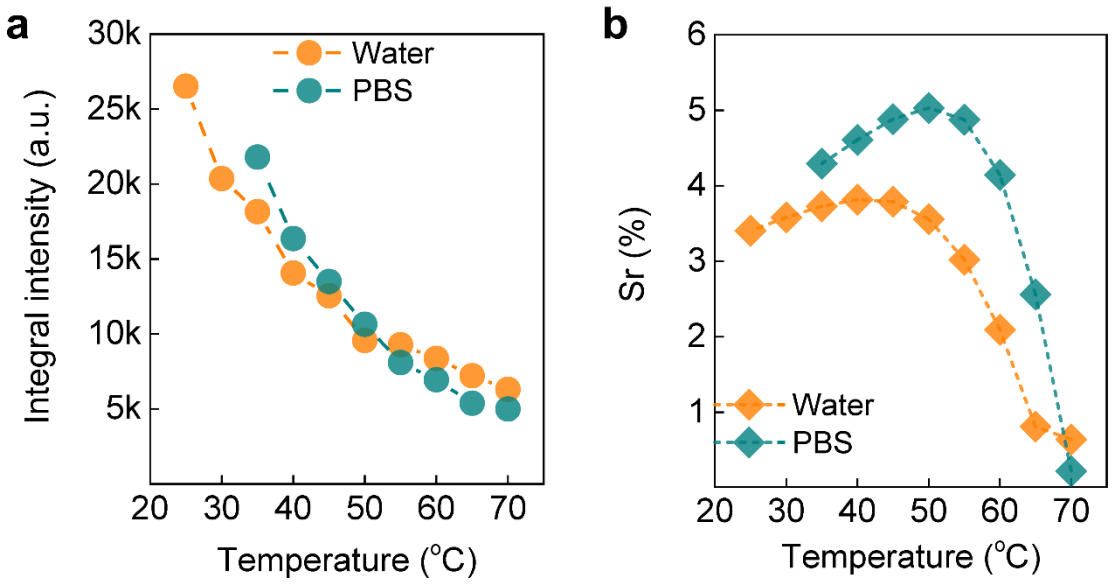

Figure 5-10. Aqueous TTA systems applied as temperature sensors. (d) Temperature-sensitive TTA upconversion in water (orange) and PBS (cyan) with inverse intensity evolution compared with traditional TTA systems. (e) The relative temperature sensing sensitivity calculated from data in (d) according to equation (5-6), $S_r = (\delta Q/\delta T)/Q$ (5-6). Q is the integral upconversion intensity. The error bars in a, b and c indicate the standard deviation of three measurements. The concentrations of acceptor and donor are 5 mM and 0.1 mM, respectively. The samples were tested under air-saturated conditions. The excitation power density is 61 mW cm^{-2}.

We further investigate the capability of TTA systems to sense temperature variations both in water and physiology media (PBS). The upconversion intensity, either in water or PBS, displays a declined tendency with the temperature increase (**Figure 5-11a**), which is

unusual compared with the traditional TTA systems [151][157][159][160][161][162]. We attribute this phenomenon to the TTA dyads dissolution in water, where the electrolytic equilibrium of water, donor/acceptor molecules and the corresponding ions may change with the temperature. Typically, high temperature enables more H^+ and OH^- from the ionization of H_2O [163], which may negatively affect the dissolution of TTA dyads and thus reduce the luminescence intensity. Compared with the properties of temperature sensing in water (from 25 to 70 ºC), the dynamic range of temperature monitored in PBS (from 35 to 70 ºC) is smaller, while the declined trend of temperature is sharper. We speculate these phenomena are related to the multi-electrolytes existing in PBS. This aqueous TTA system displays high sensitivity of temperature sensing, in particular, in PBS, with the maximum sensitivity of 5.03% $^oC^{-1}$ at 50 ºC (**Figure 5-11b**). This is comparable to the highest record of the reported temperature sensing sensitivity from TTA system[3][159].

5.4 Conclusion

We realize the efficient TTA systems in water by modulating the ion equilibrium equation of TTA dyad. The TTA can be applied in many types of aqueous media, especially in physiological buffers and electrolyte-based media. Except for the controllability *via* acceptor-donor ratios, the upconversion intensity of this water-soluble TTA shows apparent dependence of the medium. In these media, the ionized TTA dyad displays strong aerotolerance, resulting in good retention of upconversion emission in air-saturated conditions. Notably, the upconversion intensity in air-saturated Tris buffer is more than two times that in deaerated conditions, mitigating the general issue of oxygen quenching. We also demonstrate the potential of this aqueous TTA system as a pH sensor and a temperature sensor. This simple strategy may have a profound inspiration for exploring aqueous TTA systems, especially considering the possibility in biological applications.

Chapter 6 Conclusion and Outlook

In this chapter, I will give a conclusion of my PhD work and an outlook for future research.

6.1 Conclusion

The core purpose of this dissertation is to fully know, characterize and manipulate upconversion nanoparticles from four aspects, see clearer, detect force more sensitive, engineer Rayleigh scattering more easily and explore new practical probes. Toward this, we develop and further optimize biophotonics technologies of super-resolution microscopy, optical tweezers and interferometric scattering microscopy for better utilization of upconversion nanoparticles. The novelties and outcomes in this dissertation are concluded as follows,

In Chapter 2, we developed a simple but effective strategy to upgrade the nanoscopy by combining the fluorescence nonlinearity of upconversion nanoparticles and conventional confocal microscopy. This strategy avoids constructing expensive setups which are always essential for super-resolution microscopy and spends much time on complex data processing.

In Chapter 3, we optimized the current optical tweezers to measure the axial optical force via analysing the PSF variations under different axial positions by deep learning. This strategy also helps us to realize the attoNewton level force sensitivity, which is based on the unique properties of upconversion nanoparticles, such as super brightness, stability and relatively large optical trapping force compared to other kinds of nanoscale particles.

In Chapter 4, we demonstrated the morphology-immune modulation of Rayleigh scattering at the nanoscale level by doping lanthanide ions in the nanoparticle. The large resonance enhancement of upconversion nanoparticles provides more features of Rayleigh scattering recorded by interferometric scattering microscopy. We also demonstrated the multiplexed iSCAT on distinguishing different types of upconversion nanoparticles in living HeLa cells.

In Chapter 5, we developed the simple but oxygen-resistant TTA system via adjusting ionic equilibrium. We showed the wonderful performance of these TTA systems in

several media with different electrolytes and their potential in pH and temperature sensing.

6.2 Outlook

There is plenty of space for further investigation of upconversion nanoparticles in the directions of fluorescence and scattering, despite the advances displayed above. Here I list some potential research related to this dissertation below.

Single-nanoparticle behaviour

Manipulation for a single nanoparticle is the incomparable advantage of optical tweezers. This provides the potential in investigating the physical and chemical behaviours of single nanoparticles. For example, trapping the catalyst nanoparticle to understand how it works, trapping the nanoparticle with positive/negative charge to observe how it changes in size, fluorescence and aggregation/self-assembly, especially under the external disturbance of light and electromagnetic field.

Scattering-based iSCAT microscopy

In Chapter 4 we obtain the conclusion that Rayleigh scattering of nanoparticles can be enhanced via doping different lanthanide ions. This inspires us to carry out the following projects. Combining the unique property of upconversion nanoparticles, we may realize the multiplexed interferometric scattering microscopy based on scattering fluctuations of different lanthanide-doped nanoparticles. Besides, the resonance enhancement of scattering also provides the chance to develop scattering-based super-resolution microscopy.

Structure-assisted oxygen quenching-free TTA

Based on Chapter 5, the next work will focus on the realization of TTA nanoparticles for practical applications. Some preliminary work has been carried out and demonstrated the feasibility. TTA nanoparticles with dimensional structures show incredible immunity for oxygen quenching in an aqueous solution. This will make TTA nanoparticles applicable in practical biological imaging and sensing.

References

[1] Q. Zhan *et al.*, "Achieving high-efficiency emission depletion nanoscopy by employing cross relaxation in upconversion nanoparticles," *Nat. Commun.*, vol. 8, no. 1, pp. 1–11, 2017, doi: 10.1038/s41467-017-01141-y.

[2] Y. Wang *et al.*, "Nd3+-Sensitized Upconversion Nanophosphors : E ffi cient In Vivo Bioimaging Probes with Minimized Heating E ff ect," *ACS Nano*, vol. 7, no. 8, pp. 7200–7206, 2013.

[3] M. Xu *et al.*, "Ratiometric nanothermometer in vivo based on triplet sensitized upconversion," *Nat. Commun.*, vol. 9, p. 2698, 2018, doi: 10.1038/s41467-018-05160-1.

[4] E. Ortiz-Rivero *et al.*, "Single-Cell Biodetection by Upconverting Microspinners," *Small*, no. 15, p. 1904154, 2019.

[5] D. B. L. Teh *et al.*, "A Flexi-PEGDA Upconversion Implant for Wireless Brain Photodynamic Therapy," *Adv. Mater.*, vol. 32, p. 2001459, 2020.

[6] Q. Liu, B. Wu, M. Li, Y. Huang, and L. Li, "Heterostructures Made of Upconversion Nanoparticles and Metal–Organic Frameworks for Biomedical Applications," *Adv. Sci.*, vol. 9, no. 3, p. 2103911, 2022, doi: 10.1002/advs.202103911.

[7] B. D. Ravetz, A. B. Pun, E. M. Churchill, D. N. Congreve, T. Rovis, and L. M. Campos, "Photoredox catalysis using infrared light via triplet fusion upconversion," *Nature*, vol. 565, no. 7739, pp. 343–346, 2019, doi: 10.1038/s41586-018-0835-2.

[8] B. S. Richards, D. Hudry, D. Busko, A. Turshatov, and I. A. Howard, "Photon Upconversion for Photovoltaics and Photocatalysis: A Critical Review," *Chem. Rev.*, vol. 121, no. 15, pp. 9165–9195, 2021, doi: 10.1021/acs.chemrev.1c00034.

[9] H. X. Mai *et al.*, "High-quality sodium rare-earth fluoride nanocrystals: Controlled synthesis and optical properties," *J. Am. Chem. Soc.*, vol. 128, no. 19, pp. 6426–6436, 2006, doi: 10.1021/ja060212h.

[10] S. Wen *et al.*, "Nanorods with multidimensional optical information beyond the diffraction limit," *Nat. Commun.*, vol. 11, no. 1, p. 6047, 2020, doi: 10.1038/s41467-020-19952-x.

[11] F. Wang *et al.*, "Tuning upconversion through energy migration in core-shell nanoparticles," *Nat. Mater.*, vol. 10, no. 12, pp. 968–973, 2011, doi: 10.1038/nmat3149.

[12] C. Chen *et al.*, "Multi-photon near-infrared emission saturation nanoscopy using upconversion nanoparticles," *Nat. Commun.*, vol. 9, no. 1, pp. 4–9, 2018, doi: 10.1038/s41467-018-05842-w.

[13] J. Zhou, Q. Liu, W. Feng, Y. Sun, and F. Li, "Upconversion luminescent materials: Advances and applications," *Chem. Rev.*, vol. 115, no. 1, pp. 395–465, 2015, doi: 10.1021/cr400478f.

[14] B. Zhou, B. Shi, D. Jin, and X. Liu, "Controlling upconversion nanocrystals for emerging applications," *Nat. Nanotechnol.*, vol. 10, no. 11, pp. 924–936, 2015,

doi: 10.1038/nnano.2015.251.

[15] Y. Wu *et al.*, "Upconversion superburst with sub-2 μs lifetime," *Nat. Nanotechnol.*, vol. 14, no. 12. pp. 1110–1115, 2019, doi: 10.1038/s41565-019-0560-5.

[16] Z. Lei, X. Ling, Q. Mei, S. Fu, J. Zhang, and Y. Zhang, "An Excitation Navigating Energy Migration of Lanthanide Ions in Upconversion Nanoparticles," *Adv. Mater.*, vol. 32, no. 9, p. 1906225, 2020, doi: 10.1002/adma.201906225.

[17] D. Liu *et al.*, "Three-dimensional controlled growth of monodisperse sub-50 nm heterogeneous nanocrystals," *Nat. Commun.*, vol. 7, p. 10254, 2016, doi: 10.1038/ncomms10254.

[18] Y. Wang, K. Zheng, S. Song, D. Fan, H. Zhang, and X. Liu, "Remote manipulation of upconversion luminescence," *Chem. Soc. Rev.*, vol. 47, no. 17, pp. 6473–6485, 2018, doi: 10.1039/c8cs00124c.

[19] C. Lee *et al.*, "Giant nonlinear optical responses from photon-avalanching nanoparticles," *Nature*, vol. 589, no. 7841, pp. 230–235, Jan. 2021, doi: 10.1038/s41586-020-03092-9.

[20] Y. Liu *et al.*, "Amplified stimulated emission in upconversion nanoparticles for super-resolution nanoscopy," *Nature*, vol. 543, no. 7644, pp. 229–233, 2017, doi: 10.1038/nature21366.

[21] Y. Zhang, N. Pasquale, and K. B. Lee, "An upconversion nanoparticle with orthogonal emissions using dual nir excitations for controlled two-way photoswitching," *Angew. Chemie - Int. Ed.*, vol. 53, no. 52, pp. 14419–14423, 2014, doi: 10.1002/anie.201408219.

[22] C. Chen *et al.*, "Heterochromatic Nonlinear Optical Responses in Upconversion Nanoparticles for Super-Resolution Nanoscopy," *Adv. Mater.*, vol. 33, no. 23, p. 2008847, 2021, doi: 10.1002/adma.202008847.

[23] D. Denkova *et al.*, "3D sub-diffraction imaging in a conventional confocal configuration by exploiting super-linear emitters," *Nat. Commun.*, vol. 10, no. 1, p. 3695, 2019, doi: 10.1038/s41467-019-11603-0.

[24] C. Gao *et al.*, "Application of Triplet–Triplet Annihilation Upconversion in Organic Optoelectronic Devices: Advances and Perspectives," *Adv. Mater.*, vol. 33, no. 45, pp. 1–25, 2021, doi: 10.1002/adma.202100704.

[25] L. Huang, T. Le, K. Huang, and G. Han, "Enzymatic enhancing of triplet–triplet annihilation upconversion by breaking oxygen quenching for background-free biological sensing," *Nat. Commun.*, vol. 12, no. 1, p. 1898, 2021, doi: 10.1038/s41467-021-22282-1.

[26] E. M. Gholizadeh *et al.*, "Photochemical upconversion of near-infrared light from below the silicon bandgap," *Nat. Photonics*, vol. 14, no. 9, pp. 585–590, 2020, doi: 10.1038/s41566-020-0664-3.

[27] N. Yanai and N. Kimizuka, "Stimuli-Responsive Molecular Photon Upconversion," *Angew. Chemie - Int. Ed.*, vol. 59, no. 26, pp. 10252–10264, 2020, doi: 10.1002/anie.202001325.

[28] K. Mase, K. Okumura, N. Yanai, and N. Kimizuka, "Triplet sensitization by perovskite nanocrystals for photon upconversion," *Chem. Commun.*, vol. 53, no.

59, pp. 8261–8264, 2017, doi: 10.1039/c7cc03087h.

[29] S. Han *et al.*, “Lanthanide-doped inorganic nanoparticles turn molecular triplet excitons bright,” *Nature*, vol. 587, no. 7835, pp. 594–599, 2020, doi: 10.1038/s41586-020-2932-2.

[30] Frank N. Egerton, “A History of the Ecological Sciences, Part 16: Robert Hooke and the Royal Society of London,” *Bull. Ecol. Soc. Am.*, vol. 86, no. 2, pp. 93–101, 2005.

[31] K. Uluç, G. C. Kujoth, and M. K. Başkaya, “Operating microscopes: Past, present, and future,” *Neurosurg. Focus*, vol. 27, no. 3, pp. 1–8, 2009, doi: 10.3171/2009.6.FOCUS09120.

[32] T. A. Klar, E. Engel, and S. W. Hell, “Breaking Abbe’s diffraction resolution limit in fluorescence microscopy with stimulated emission depletion beams of various shapes,” *Phys. Rev. E - Stat. Physics, Plasmas, Fluids, Relat. Interdiscip. Top.*, vol. 64, no. 6, p. 066613, 2001, doi: 10.1103/PhysRevE.64.066613.

[33] A. Bednarkiewicz, E. M. Chan, A. Kotulska, L. Marciniak, and K. Prorok, “Photon avalanche in lanthanide doped nanoparticles for biomedical applications: Super-resolution imaging,” *Nanoscale Horizons*, vol. 4, no. 4, pp. 881–889, 2019, doi: 10.1039/c9nh00089e.

[34] M. J. Rust, M. Bates, and X. Zhuang, “Sub-diffraction-limit imaging by stochastic optical reconstruction microscopy (STORM),” *Nat. Methods*, vol. 3, no. 10, pp. 793–795, 2006, doi: 10.1038/nmeth929.

[35] Bowen Wang, M. Xiong, J. Susanto, X. Li, W.-Y. Leung, and K. Xu, “Transforming Rhodamine Dyes for (d)STORM Super-Resolution Microscopy via 1,3-Disubstituted Imidazolium Substitution,” *Angew. Chem. Int. Ed.*, vol. 134, no. 61, p. e202113612, 2022.

[36] J. A. Erstling *et al.*, “Ultrasmall, Bright, and Photostable Fluorescent Core–Shell Aluminosilicate Nanoparticles for Live-Cell Optical Super-Resolution Microscopy,” *Adv. Mater.*, vol. 33, no. 8, p. 2006829, 2021, doi: 10.1002/adma.202006829.

[37] L. von Chamier *et al.*, “Democratising deep learning for microscopy with ZeroCostDL4Mic,” *Nat. Commun.*, vol. 12, no. 1, p. 2276, 2021, doi: 10.1038/s41467-021-22518-0.

[38] G. H. P. Eric Betzig Rachid Sougrat O. Wolf Lindwasser Scott Olenych Juan S. Bonifacino Michael W. Davidson Jennifer Lippincott-Schwartz Harald F. Hess *et al.*, “Imaging Intracellular Fluorescent Proteins at Nanometer Resolution,” *Science (80-.).*, vol. 313, no. 5793, pp. 1642–1645, 2006, doi: 10.1126/science.1127344.

[39] L. G. Jensen *et al.*, “Correction of multiple-blinking artifacts in photoactivated localization microscopy,” *Nat. Methods*, vol. 19, no. 5, pp. 594–602, 2022, doi: 10.1038/s41592-022-01463-w.

[40] M. Lelek *et al.*, “Single-molecule localization microscopy,” *Nat. Rev. Methods Prim.*, vol. 1, no. 1, p. 39, 2021, doi: 10.1038/s43586-021-00038-x.

[41] V. Bayle *et al.*, “Single-particle tracking photoactivated localization microscopy of membrane proteins in living plant tissues,” *Nat. Protoc.*, vol. 16, no. 3, pp.

1600–1628, 2021, doi: 10.1038/s41596-020-00471-4.

[42] B. Huang, W. Wang, M. Bates, and X. Zhuang, “Three-Dimensional Super-Resolution Reconstruction Microscopy,” *Science (80-.).*, vol. 319, no. February, pp. 810–813, 2008, [Online]. Available: http://www.ncbi.nlm.nih.gov/pubmed/18174397.

[43] M. G. L. Gustafsson, “Nonlinear structured-illumination microscopy: wide-field fluorescence imaging with theoretically unlimited resolution,” *Proc. Natl. Acad. Sci. U. S. A.*, vol. 102, no. 37, pp. 13081–13086, 2005, doi: 10.1073/pnas.0406877102.

[44] R. Heintzmann and T. Huser, “Super-Resolution Structured Illumination Microscopy,” *Chem. Rev.*, vol. 117, no. 23, pp. 13890–13908, 2017, doi: 10.1021/acs.chemrev.7b00218.

[45] B. Liu *et al.*, “Upconversion Nonlinear Structured Illumination Microscopy,” *Nano Lett.*, vol. 20, no. 7, pp. 4775–4781, 2020, doi: 10.1021/acs.nanolett.0c00448.

[46] S. W. Hell and J. Wichmann, “Breaking the diffraction resolution limit by stimulated emission: stimulated-emission-depletion fluorescence microscopy,” *Opt. Lett.*, vol. 19, no. 11, p. 780, 1994, doi: 10.1364/ol.19.000780.

[47] K. I. Willig, B. Harke, R. Medda, and S. W. Hell, “STED microscopy with continuous wave beams,” *Nat. Methods*, vol. 4, no. 11, pp. 915–918, 2007, doi: 10.1038/nmeth1108.

[48] S. Van De Linde *et al.*, “Direct stochastic optical reconstruction microscopy with standard fluorescent probes,” *Nat. Protoc.*, vol. 6, no. 7, pp. 991–1009, 2011, doi: 10.1038/nprot.2011.336.

[49] G. Pesce, P. H. Jones, O. M. Maragò, and G. Volpe, *Optical tweezers: theory and practice*, vol. 135, no. 12. Springer Berlin Heidelberg, 2020.

[50] S. Helgadottir, A. Argun, and G. Volpe, “Digital microscopy enhanced by deep learning,” *Optica*, vol. 6, no. 4, 2019, doi: 10.1364/oma.2019.at2e.5.

[51] L. Priest, J. S. Peters, and P. Kukura, “Scattering-based Light Microscopy: From Metal Nanoparticles to Single Proteins,” *Chem. Rev.*, vol. 121, no. 19, pp. 11937–11970, 2021, doi: 10.1021/acs.chemrev.1c00271.

[52] T. Heermann, F. Steiert, B. Ramm, N. Hundt, and P. Schwille, “Mass-sensitive particle tracking to elucidate the membrane-associated MinDE reaction cycle,” *Nat. Methods*, vol. 18, no. 10, pp. 1239–1246, 2021, doi: 10.1038/s41592-021-01260-x.

[53] K. Lindfors, T. Kalkbrenner, P. Stoller, and V. Sandoghdar, “Detection and spectroscopy of gold nanoparticles using supercontinuum white light confocal microscopy,” *Phys. Rev. Lett.*, vol. 93, no. 3, pp. 3–6, 2004, doi: 10.1103/PhysRevLett.93.037401.

[54] R. W. Taylor, R. G. Mahmoodabadi, V. Rauschenberger, A. Giessl, A. Schambony, and V. Sandoghdar, “Interferometric scattering microscopy reveals microsecond nanoscopic protein motion on a live cell membrane,” *Nat. Photonics*, vol. 13, no. 7, pp. 480–487, 2019, doi: 10.1038/s41566-019-0414-6.

[55] E. D. B. Foley, M. S. Kushwah, G. Young, and P. Kukura, “Mass photometry enables label-free tracking and mass measurement of single proteins on lipid bilayers,” *Nat. Methods*, vol. 18, no. 10, pp. 1247–1252, 2021, doi: 10.1038/s41592-021-01261-w.

[56] A. J. Cox, A. J. DeWeerd, and J. Linden, “An experiment to measure Mie and Rayleigh total scattering cross sections,” *Am. J. Phys.*, vol. 70, no. 6, pp. 620–625, 2002, doi: 10.1119/1.1466815.

[57] M. Delor, H. L. Weaver, Q. Q. Yu, and N. S. Ginsberg, “Imaging material functionality through three-dimensional nanoscale tracking of energy flow,” *Nat. Mater.*, vol. 19, no. 1, pp. 56–62, 2020, doi: 10.1038/s41563-019-0498-x.

[58] M. J. Sarmento *et al.*, “Exploiting the tunability of stimulated emission depletion microscopy for super-resolution imaging of nuclear structures,” *Nat. Commun.*, vol. 9, no. 1, p. 3415, 2018, doi: 10.1038/s41467-018-05963-2.

[59] M. Yamanaka *et al.*, “SAX microscopy with fluorescent nanodiamond probes for high-resolution fluorescence imaging,” *Biomed. Opt. Express*, vol. 2, no. 7, pp. 1946–1954, 2011, doi: 10.1364/boe.2.001946.

[60] C. Liu *et al.*, “Super-resolution nanoscopy by coherent control on nanoparticle emission,” *Sci. Adv.*, vol. 6, no. 16, p. eaaw6579, 2020, doi: 10.1126/sciadv.aaw6579.

[61] B. E. Urban *et al.*, “Super-resolution two-photon microscopy via scanning patterned illumination,” *Phys. Rev. E - Stat. Nonlinear, Soft Matter Phys.*, vol. 91, no. 4, p. 042703, 2015, doi: 10.1103/PhysRevE.91.042703.

[62] A. G. York *et al.*, “Resolution doubling in live, multicellular organisms via multifocal structured illumination microscopy,” *Nat. Methods*, vol. 9, no. 7, pp. 749–754, 2012, doi: 10.1038/nmeth.2025.

[63] M. G. L. Gustafsson, “Surpassing the lateral resolution limit by a factor of two using structured illumination microscopy,” *J. Microsc.*, vol. 198, pp. 82–87, 2000, doi: 10.1046/j.1365-2818.2000.00710.x.

[64] E. Mudry *et al.*, “Structured illumination microscopy using unknown speckle patterns,” *Nat. Photonics*, vol. 6, no. 5, pp. 312–315, 2012, doi: 10.1038/nphoton.2012.83.

[65] H. Yilmaz, E. G. van Putten, J. Bertolotti, A. Lagendijk, W. L. Vos, and A. P. Mosk, “Speckle correlation resolution enhancement of wide-field fluorescence imaging,” *Optica*, vol. 2, no. 5, pp. 424–429, 2015, doi: 10.1364/optica.2.000424.

[66] K. Fujita, M. Kobayashi, S. Kawano, M. Yamanaka, and S. Kawata, “High-resolution confocal microscopy by saturated excitation of fluorescence,” *Phys. Rev. Lett.*, vol. 99, no. 22, p. 228105, 2007, doi: 10.1103/PhysRevLett.99.228105.

[67] S. De Camillis *et al.*, “Controlling the non-linear emission of upconversion nanoparticles to enhance super-resolution imaging performance,” *Nanoscale*, vol. 12, no. 39, pp. 20347–20355, 2020, doi: 10.1039/d0nr04809g.

[68] L. Liang *et al.*, “Continuous-wave near-infrared stimulated-emission depletion microscopy using downshifting lanthanide nanoparticles,” *Nat. Nanotechnol.*, vol. 16, no. 9, pp. 975–980, 2021, doi: 10.1038/s41565-021-00927-y.

[69] J. Enderlein, “Breaking the diffraction limit with dynamic saturation optical microscopy,” *Appl. Phys. Lett.*, vol. 87, no. 9, p. 094105, 2005, doi: 10.1063/1.2034116.

[70] J. Humpolíčková, A. Benda, and J. Enderlein, “Optical Saturation as a Versatile Tool to Enhance Resolution in Confocal Microscopy,” *Biophys. J.*, vol. 97, no. 9, pp. 2623–2629, Nov. 2009, doi: 10.1016/j.bpj.2009.08.002.

[71] L. Gao, A. Garcia-Uribe, Y. Liu, C. Li, and L. V. Wang, “Photobleaching imprinting microscopy: Seeing clearer and deeper,” *J. Cell Sci.*, vol. 127, no. 2, pp. 288–294, 2014, doi: 10.1242/jcs.142943.

[72] Y. Zhang *et al.*, “Super-resolution fluorescence microscopy by stepwise optical saturation,” *Biomed. Opt. Express*, vol. 9, no. 4, pp. 1613–1629, 2018, doi: 10.1364/boe.9.001613.

[73] Y. Nawa *et al.*, “Saturated excitation microscopy using differential excitation for efficient detection of nonlinear fluorescence signals,” *APL Photonics*, vol. 3, no. 8, p. 080805, 2018, doi: 10.1063/1.5039567.

[74] C. Chen *et al.*, “Heterochromatic Nonlinear Optical Responses in Upconversion Nanoparticles for Super-Resolution Nanoscopy,” *Adv. Mater.*, vol. 33, no. 23, p. 2008847, Jun. 2021, doi: 10.1002/adma.202008847.

[75] J. Wang, L. Wang, J. Zhang, Z. Yang, W. Yan, and J. Qu, “Improving the image quality in STED nanoscopy using frequency spectrum modulation,” *J. Biophotonics*, vol. 14, no. 3, pp. 1–5, 2021, doi: 10.1002/jbio.202000402.

[76] C. Zensen, N. Villadsen, F. Winterer, S. R. Keiding, and T. Lohmüller, “Pushing nanoparticles with light - A femtonewton resolved measurement of optical scattering forces,” *APL Photonics*, vol. 1, no. 2, 2016, doi: 10.1063/1.4945351.

[77] C. D. S. Brites *et al.*, “Instantaneous ballistic velocity of suspended Brownian nanocrystals measured by upconversion nanothermometry,” *Nat. Nanotechnol.*, vol. 11, no. 10, pp. 851–856, 2016, doi: 10.1038/nnano.2016.111.

[78] P. Rodríguez-Sevilla, Y. Arita, X. Liu, D. Jaque, and K. Dholakia, “The Temperature of an Optically Trapped, Rotating Microparticle,” *ACS Photonics*, vol. 5, no. 9, pp. 3772–3778, 2018, doi: 10.1021/acsphotonics.8b00822.

[79] H. C. Boyer, K. Gorkowski, and R. C. Sullivan, “In Situ pH Measurements of Individual Levitated Microdroplets Using Aerosol Optical Tweezers,” *Anal. Chem.*, vol. 92, no. 1, pp. 1089–1096, 2020, doi: 10.1021/acs.analchem.9b04152.

[80] I. Heller *et al.*, “STED nanoscopy combined with optical tweezers reveals protein dynamics on densely covered DNA,” *Nat. Methods*, vol. 10, no. 9, pp. 910–916, 2013, doi: 10.1038/nmeth.2599.

[81] S. Sudhakar *et al.*, “Germanium nanospheres for ultraresolution picotensiometry of kinesin motors,” *Science (80-.).*, vol. 371, no. 6530, 2021, doi: 10.1126/science.abd9944.

[82] Y. Nakayama *et al.*, “Tunable nanowire nonlinear optical probe,” *Nature*, vol. 447, no. 7148, pp. 1098–1101, 2007, doi: 10.1038/nature05921.

[83] P. J. Pauzauskie, A. Radenovic, E. Trepagnier, H. Shroff, P. Yang, and J. Liphardt, “Optical trapping and integration of semiconductor nanowire assemblies in water,”

Nat. Mater., vol. 5, no. 2, pp. 97–101, 2006, doi: 10.1038/nmat1563.

[84] A. Ashkin, J. M. Dziedzic, J. E. Bjorkholm, and S. Chu, "Observation of a single-beam gradient force optical trap for dielectric particles," *Opt. Angular Momentum*, vol. 11, no. 5, pp. 196–198, 2016, doi: 10.1364/ol.11.000288.

[85] P. J. Reece *et al.*, "Characterization of semiconductor nanowires using optical tweezers," *Nano Lett.*, vol. 11, no. 6, pp. 2375–2381, 2011, doi: 10.1021/nl200720m.

[86] D. Lu, M. Pedroni, L. Labrador-Páez, M. I. Marqués, D. Jaque, and P. Haro-González, "Nanojet Trapping of a Single Sub-10 nm Upconverting Nanoparticle in the Full Liquid Water Temperature Range," *Small*, vol. 17, no. 7, 2021, doi: 10.1002/smll.202006764.

[87] I. F. Sbalzarini and P. Koumoutsakos, "Feature point tracking and trajectory analysis for video imaging in cell biology," *J. Struct. Biol.*, vol. 151, no. 2, pp. 182–195, 2005, doi: 10.1016/j.jsb.2005.06.002.

[88] X. Shan *et al.*, "Optical tweezers beyond refractive index mismatch using highly doped upconversion nanoparticles," *Nat. Nanotechnol.*, vol. 16, no. 5, pp. 531–537, May 2021, doi: 10.1038/s41565-021-00852-0.

[89] K. Svoboda and S. M. Block, "Optical trapping of metallic Rayleigh particles," *Opt. Lett.*, vol. 19, no. 13, p. 930, 1994, doi: 10.1364/ol.19.000930.

[90] A. Rohrbach, "Stiffness of optical traps: Quantitative agreement between experiment and electromagnetic theory," *Phys. Rev. Lett.*, vol. 95, no. 16, pp. 1–4, 2005, doi: 10.1103/PhysRevLett.95.168102.

[91] J. Gieseler *et al.*, "Optical Tweezers: A Comprehensive Tutorial from Calibration to Applications," pp. 1–149, 2020, [Online]. Available: http://arxiv.org/abs/2004.05246.

[92] E. L. Florin, A. Pralle, E. H. K. Stelzer, and J. K. H. Hörber, "Photonic forcemicroscope calibration by thermal noise analysis," *Appl. Phys. A Mater. Sci. Process.*, vol. 66, no. SUPPL. 1, pp. 75–78, 1998, doi: 10.1007/s003390051103.

[93] O. M. Maragò *et al.*, "Femtonewton force sensing with optically trapped nanotubes," *Nano Lett.*, vol. 8, no. 10, pp. 3211–3216, 2008, doi: 10.1021/nl8015413.

[94] C. F. Bohren, *Absorption and scattering of light by small particles*. 1983.

[95] R. El-Kurdi and D. Patra, "Gold and silver nanoparticles in resonance Rayleigh scattering techniques for chemical sensing and biosensing: a review," *Microchim. Acta*, vol. 186, no. 10, p. 667, Oct. 2019, doi: 10.1007/s00604-019-3755-4.

[96] S.-W. Chu *et al.*, "Measurement of a Saturated Emission of Optical Radiation from Gold Nanoparticles: Application to an Ultrahigh Resolution Microscope," *Phys. Rev. Lett.*, vol. 112, no. 1, p. 017402, Jan. 2014, doi: 10.1103/PhysRevLett.112.017402.

[97] S. Gottardo, R. Sapienza, P. D. García, A. Blanco, D. S. Wiersma, and C. López, "Resonance-driven random lasing," *Nat. Photonics*, vol. 2, no. 7, pp. 429–432, 2008, doi: 10.1038/nphoton.2008.102.

[98] F. Nickel, M. Bernien, U. Lipowski, and W. Kuch, “Optical differential reflectance spectroscopy for photochromic molecules on solid surfaces,” *Rev. Sci. Instrum.*, vol. 89, no. 3, p. 033113, Mar. 2018, doi: 10.1063/1.5019415.

[99] M. Montazeri *et al.*, “Transient Rayleigh scattering from single semiconductor nanowires,” *AIP Conf. Proc.*, vol. 1566, no. December 2013, pp. 425–426, 2013, doi: 10.1063/1.4848467.

[100] X. Yuan *et al.*, “Antimony Induced {112}A Faceted Triangular GaAs1-xSbx/InP Core/Shell Nanowires and Their Enhanced Optical Quality,” *Adv. Funct. Mater.*, vol. 25, no. 33, pp. 5300–5308, 2015, doi: 10.1002/adfm.201501467.

[101] S. J. Youn, T. H. Rho, B. I. Min, and K. S. Kim, “Extended Drude model analysis of noble metals,” *Phys. Status Solidi*, vol. 244, no. 4, pp. 1354–1362, 2007, doi: 10.1002/pssb.200642097.

[102] Y. Wang, C. Yuan, Z. Zhou, L. Li, and Y. Du, “Propagation of Gaussian laser beam in cold plasma of Drude model,” *Phys. Plasmas*, vol. 18, no. 11, 2011, doi: 10.1063/1.3662433.

[103] J. Lee *et al.*, “Observation and Differentiation of Unique High-Q Optical Resonances Near Zero Wave Vector in Macroscopic Photonic Crystal Slabs,” *Phys. Rev. Lett.*, vol. 109, no. 6, p. 067401, Aug. 2012, doi: 10.1103/PhysRevLett.109.067401.

[104] C. W. Hsu *et al.*, “Observation of trapped light within the radiation continuum,” *Nature*, vol. 499, pp. 188–191, 2013, doi: 10.1038/nature12289.

[105] S. Kim, “Bound states in the continuum in quantum-dot pairs,” *Phys. Rev. A*, pp. 1–4, 2006, doi: 10.1103/PhysRevA.73.022113.

[106] V. A. Sablikov and A. A. Sukhanov, “Helical bound states in the continuum of the edge states in two dimensional topological insulators,” *Phys. Lett. A*, vol. 379, no. 30–31, pp. 1775–1779, 2015, doi: 10.1016/j.physleta.2015.05.005.

[107] M. S. Bahramy, N. Nagaosa, and B. Yang, “Topological protection of bound states against the hybridization,” *Nat. Commun.*, pp. 1–9, 2013, doi: 10.1038/ncomms2524.

[108] M. I. Molina, A. E. Miroshnichenko, and Y. S. Kivshar, “Surface Bound States in the Continuum,” *Phys. Rev. Lett.*, vol. 070401, no. February, pp. 1–4, 2012, doi: 10.1103/PhysRevLett.108.070401.

[109] V. Jacobsen, P. Stoller, C. Brunner, V. Vogel, and V. Sandoghdar, “Interferometric optical detection and tracking of very small gold nanoparticles at a water-glass interface,” *Opt. Express*, vol. 14, no. 1, p. 405, 2006, doi: 10.1364/OPEX.14.000405.

[110] X.-Y. Wan *et al.*, “Real-Time Light Scattering Tracking of Gold Nanoparticles-bioconjugated Respiratory Syncytial Virus Infecting HEp-2 Cells,” *Sci. Rep.*, vol. 4, no. 1, p. 4529, May 2015, doi: 10.1038/srep04529.

[111] M. Montazeri *et al.*, “Photomodulated rayleigh scattering of single semiconductor nanowires: Probing electronic band structure,” *Nano Lett.*, vol. 11, no. 10, pp. 4329–4336, 2011, doi: 10.1021/nl202433g.

[112] G. Jnawali *et al.*, “Ultrafast photoinduced band splitting and carrier dynamics in

chiral tellurium nanosheets," *Nat. Commun.*, vol. 11, no. 1, pp. 1–10, 2020, doi: 10.1038/s41467-020-17766-5.

[113] R. Forker and T. Fritz, "Optical differential reflectance spectroscopy of ultrathin epitaxial organic films," *Phys. Chem. Chem. Phys.*, vol. 11, no. 13, pp. 2142–2155, 2009, doi: 10.1039/b814628d.

[114] F. Wang *et al.*, "Microscopic inspection and tracking of single upconversion nanoparticles in living cells," *Light Sci. Appl.*, vol. 7, no. 4, pp. 18006–18007, 2018, doi: 10.1038/lsa.2018.7.

[115] M. Maddahfar *et al.*, "Stable and Highly Efficient Antibody-Nanoparticles Conjugation," *Bioconjug. Chem.*, vol. 32, no. 6, pp. 1146–1155, 2021, doi: 10.1021/acs.bioconjchem.1c00192.

[116] N. Li, T. D. Canady, Q. Huang, X. Wang, G. A. Fried, and B. T. Cunningham, "Photonic resonator interferometric scattering microscopy," *Nat. Commun.*, vol. 12, no. 1, pp. 1–9, 2021, doi: 10.1038/s41467-021-21999-3.

[117] G. Young *et al.*, "Quantitative mass imaging of single biological macromolecules," *Science (80-.).*, vol. 360, no. 6387, pp. 423–427, 2018, doi: 10.1126/science.aar5839.

[118] D. J. Gargas *et al.*, "Engineering bright sub-10-nm upconverting nanocrystals for single-molecule imaging," *Nat. Nanotechnol.*, vol. 9, no. 4, pp. 300–305, 2014, doi: 10.1038/nnano.2014.29.

[119] H. Dong, L. D. Sun, and C. H. Yan, "Upconversion emission studies of single particles," *Nano Today*, vol. 35, p. 100956, 2020, doi: 10.1016/j.nantod.2020.100956.

[120] S. Wen, J. Zhou, K. Zheng, A. Bednarkiewicz, X. Liu, and D. Jin, "Advances in highly doped upconversion nanoparticles," *Nat. Commun.*, vol. 9, no. 1, p. 2415, Dec. 2018, doi: 10.1038/s41467-018-04813-5.

[121] W. Zou, C. Visser, J. A. Maduro, M. S. Pshenichnikov, and J. C. Hummelen, "Broadband dye-sensitized upconversion of near-infrared light," *Nat. Photonics*, vol. 6, no. 8, pp. 560–564, 2012, doi: 10.1038/nphoton.2012.158.

[122] R. S. Quimby, W. J. Miniscalco, and B. A. Thompson, "Excited-state absorption at 980 nm in erbium doped glass," *Fiber Laser Sources Amplifiers III*, vol. 1581, no. January 1992, pp. 72–79, 1992, doi: 10.1117/12.134972.

[123] Y. Wang *et al.*, "Nd3+-Sensitized Upconversion Nanophosphors: Efficient In Vivo Bioimaging Probes with Minimized Heating Effect," *ACS Nano*, no. 8, pp. 7200–7206, 2013.

[124] P. Kukura, H. Ewers, C. Müller, A. Renn, A. Helenius, and V. Sandoghdar, "High-speed nanoscopic tracking of the position and orientation of a single virus," *Nat. Methods*, vol. 6, no. 12, pp. 923–927, 2009, doi: 10.1038/nmeth.1395.

[125] Y. F. Huang, G. Y. Zhuo, C. Y. Chou, C. H. Lin, W. Chang, and C. L. Hsieh, "Coherent Brightfield Microscopy Provides the Spatiotemporal Resolution to Study Early Stage Viral Infection in Live Cells," *ACS Nano*, vol. 11, no. 3, pp. 2575–2585, 2017, doi: 10.1021/acsnano.6b05601.

[126] Y.-T. Hsiao, C.-N. Tsai, T.-H. Chen, and C.-L. Hsieh, "Label-Free Dynamic

Imaging of Chromatin in Live Cell Nuclei by High-Speed Scattering-Based Interference Microscopy," *ACS Nano*, Dec. 2021, doi: 10.1021/acsnano.1c09748.

[127] Y. F. Huang, G. Y. Zhuo, C. Y. Chou, C. H. Lin, and C. L. Hsieh, "Label-free, ultrahigh-speed, 3D observation of bidirectional and correlated intracellular cargo transport by coherent brightfield microscopy," *Nanoscale*, vol. 9, no. 19, pp. 6567–6574, 2017, doi: 10.1039/c7nr00604g.

[128] J. S. Park *et al.*, "Label-free and live cell imaging by interferometric scattering microscopy," *Chem. Sci.*, vol. 9, no. 10, pp. 2690–2697, 2018, doi: 10.1039/c7sc04733a.

[129] A. J. Merryweather, C. Schnedermann, Q. Jacquet, C. P. Grey, and A. Rao, "Operando optical tracking of single-particle ion dynamics in batteries," *Nature*, vol. 594, no. 7864, pp. 522–528, 2021, doi: 10.1038/s41586-021-03584-2.

[130] D. C. Dowson and B. V. Landau, "The Fréchet distance between multivariate normal distributions," *J. Multivar. Anal.*, vol. 12, no. 3, pp. 450–455, 1982, doi: 10.1016/0047-259X(82)90077-X.

[131] T. Eiter and H. Mannila, "Computing discrete Fr{é}chet distance," *Notes*, vol. 94, p. 64, 1994, [Online]. Available: http://citeseerx.ist.psu.edu/viewdoc/download?doi=10.1.1.90.937&rep=rep1&type=pdf.

[132] Z. J. Yang, R. Jiang, X. Zhuo, Y. M. Xie, J. Wang, and H. Q. Lin, "Dielectric nanoresonators for light manipulation," *Phys. Rep.*, vol. 701, pp. 1–50, 2017, doi: 10.1016/j.physrep.2017.07.006.

[133] M. Ringler *et al.*, "Shaping Emission Spectra of Fluorescent Molecules with Single Plasmonic Nanoresonators," *Phys. Rev. Lett.*, vol. 100, no. 20, p. 203002, May 2008, doi: 10.1103/PhysRevLett.100.203002.

[134] J. Xu *et al.*, "Resonant Scattering Manipulation of Dielectric Nanoparticles," *Adv. Opt. Mater.*, vol. 9, no. 15, p. 2100112, Aug. 2021, doi: 10.1002/adom.202100112.

[135] Y. I. Park, K. T. Lee, Y. D. Suh, and T. Hyeon, "Upconverting nanoparticles: a versatile platform for wide-field two-photon microscopy and multi-modal in vivo imaging," *Chem. Soc. Rev.*, vol. 44, no. 6, pp. 1302–1317, 2015, doi: 10.1039/c4cs00173g.

[136] T. F. Schulze and T. W. Schmidt, "Photochemical upconversion: present status and prospects for its application to solar energy conversion," *Energy Environ. Sci.*, vol. 8, no. 1, pp. 103–125, 2015, doi: 10.1039/c4ee02481h.

[137] Y. Y. Cheng *et al.*, "Improving the light-harvesting of amorphous silicon solar cells with photochemical upconversion," *Energy Environ. Sci.*, vol. 5, no. 5, pp. 6953–6959, 2012, doi: 10.1039/c2ee21136j.

[138] J. Park, M. Xu, F. Y. Li, and H. C. Zhou, "3D Long-Range Triplet Migration in a Water-Stable Metal-Organic Framework for Upconversion-Based Ultralow-Power in Vivo Imaging," *J. Am. Chem. Soc.*, vol. 140, no. 16, pp. 5493–5499, 2018, doi: 10.1021/jacs.8b01613.

[139] A. Ronchi *et al.*, "High Photon Upconversion Efficiency with Hybrid Triplet Sensitizers by Ultrafast Hole-Routing in Electronic-Doped Nanocrystals," *Adv.*

Mater., vol. 32, no. 37, p. 2002953, 2020, doi: 10.1002/adma.202002953.

[140] S. S. Liu, X. Y. Wang, H. Y. Liu, L. Shen, D. Z. Zhao, and X. Y. Li, "Enhancing triplet sensitization ability of donor-acceptor dyads via intramolecular triplet energy transfer," *J. Mater. Chem. C*, vol. 8, no. 10, pp. 3536–3544, 2020, doi: 10.1039/c9tc06337d.

[141] J. H. Kang, S. H. Kim, A. Fernandez-Nieves, and E. Reichmanis, "Amplified Photon Upconversion by Photonic Shell of Cholesteric Liquid Crystals," *J. Am. Chem. Soc.*, vol. 139, no. 16, pp. 5708–5711, 2017, doi: 10.1021/jacs.7b01981.

[142] B. Pfund *et al.*, "SI-UV Light Generation and Challenging Photoreactions Enabled by Upconversion in Water," *J. Am. Chem. Soc.*, 2020, doi: 10.1021/jacs.0c02835.

[143] H. Minami, T. Ichikawa, K. Nakamura, and N. Kobayashi, "Electrochemically triggered upconverted luminescence for light-emitting devices," *Chem. Commun.*, vol. 55, no. 84, pp. 12611–12614, 2019, doi: 10.1039/c9cc05845a.

[144] Z. Jiang, M. Xu, F. Li, and Y. Yu, "Red-light-controllable liquid-crystal soft actuators via low-power excited upconversion based on triplet-triplet annihilation," *J Am Chem Soc*, vol. 135, no. 44, pp. 16446–16453, 2013, doi: 10.1021/ja406020r.

[145] Y. Zhou, C. Ruchlin, A. J. Robb, and K. Hanson, "Singlet Sensitization-Enhanced Upconversion Solar Cells via Self-Assembled Trilayers," *Acs Energy Lett.*, vol. 4, no. 6, pp. 1458–1463, 2019, doi: 10.1021/acsenergylett.9b00870.

[146] H. Kouno, T. Ogawa, S. Amemori, P. Mahato, N. Yanai, and N. Kimizuka, "Triplet energy migration-based photon upconversion by amphiphilic molecular assemblies in aerated water," *Chem Sci*, vol. 7, no. 8, pp. 5224–5229, 2016, doi: 10.1039/c6sc01047d.

[147] H. Kouno, Y. Sasaki, N. Yanai, and N. Kimizuka, "Supramolecular Crowding Can Avoid Oxygen Quenching of Photon Upconversion in Water," *Chem. Eur. J.*, vol. 25, no. 24, pp. 6124–6130, 2019, doi: 10.1002/chem.201806076.

[148] Y. Sasaki *et al.*, "Near-Infrared Optogenetic Genome Engineering Based on Photon-Upconversion Hydrogels," *Angew. Chemie-International Ed.*, vol. 58, no. 49, pp. 17827–17833, 2019, doi: 10.1002/anie.201911025.

[149] S. N. Sanders, M. K. Gangishetty, M. Y. Sfeir, and D. N. Congreve, "Photon Upconversion in Aqueous Nanodroplets," *J. Am. Chem. Soc.*, vol. 141, no. 23, pp. 9180–9184, 2019, doi: 10.1021/jacs.9b03992.

[150] R. Vadrucci, A. Monguzzi, F. Saenz, B. D. Wilts, Y. C. Simon, and C. Weder, "Nanodroplet-Containing Polymers for Efficient Low-Power Light Upconversion," *Adv. Mater.*, vol. 29, no. 41, p. 1702992, 2017, doi: 10.1002/adma.201702992.

[151] A. Turshatov, D. Busko, N. Kiseleva, S. L. Grage, I. A. Howard, and B. S. Richards, "Room-Temperature High-Efficiency Solid-State Triplet-Triplet Annihilation Up-Conversion in Amorphous Poly(olefin sulfone)s," *ACS Appl. Mater. Interfaces*, vol. 9, no. 9, pp. 8280–8286, 2017, doi: 10.1021/acsami.6b12625.

[152] S. E. Seo *et al.*, "Single-photon-driven up-/down-conversion nanohybrids for in

vivo mercury detection and real-time tracking," *J. Mater. Chem. A*, vol. 8, no. 4, pp. 1668–1677, 2020, doi: 10.1039/c9ta10921h.

[153] L. Huang, Y. Zhao, H. Zhang, K. Huang, J. Y. Yang, and G. Han, "Expanding Anti-Stokes Shifting in Triplet-Triplet Annihilation Upconversion for In Vivo Anticancer Prodrug Activation," *Angew. Chem. Int. Ed.*, vol. 56, no. 46, pp. 14400–14404, 2017, doi: 10.1002/anie.201704430.

[154] S. H. C. Askes *et al.*, "Imaging the lipid bilayer of giant unilamellar vesicles using red-to-blue light upconversion," *Chem. Commun.*, vol. 51, no. 44, pp. 9137–9140, 2015, doi: 10.1039/c5cc02197a.

[155] and J. P. Yesub Keum, Seonghun Park, Ying-Pin Chen, "Titanium-Carboxylate Metal-Organic Framework Based on an Unprecedented Ti-Oxo Chain Cluster," *Angew. Chem. Int. Ed.*, vol. 130, pp. 15068–15072, 2018.

[156] Y. S. Tomohiko Sato, Wasuke Mori, Chika Nozaki Kato, Emiko Yanaoka, Tomonori Kuribayashi, Ryoji Ohtera, "Novel microporous rhodium(II) carboxylate polymer complexes containing metalloporphyrin: syntheses and catalytic performances in hydrogenation of olefin," *J. Catal.*, vol. 232, pp. 186–198, 2005.

[157] Y. C. Simon and C. Weder, "Low-power photon upconversion through triplet-triplet annihilation in polymers," *J. Mater. Chem.*, vol. 22, no. 39, pp. 20817–20830, 2012, doi: 10.1039/c2jm33654e.

[158] K. Suzuki *et al.*, "Reevaluation of absolute luminescence quantum yields of standard solutions using a spectrometer with an integrating sphere and a back-thinned CCD detector," *Phys. Chem. Chem. Phys.*, vol. 11, no. 42, pp. 9850–9860, 2009, doi: 10.1039/b912178a.

[159] B. Iyisan *et al.*, "Temperature Sensing in Cells Using Polymeric Upconversion Nanocapsules," *Biomacromolecules*, vol. 21, no. 11, pp. 4469–4478, 2020, doi: 10.1021/acs.biomac.0c00377.

[160] S. H. C. Askes, A. Bahreman, and S. Bonnet, "Activation of a Photodissociative Ruthenium Complex by Triplet-Triplet Annihilation Upconversion in Liposomes," *Angew. Chemie, Int. Ed.*, vol. 53, no. 4, pp. 1029–1033, 2014, doi: 10.1002/anie.201309389.

[161] S. H. C. Askes, P. Brodie, G. Bruylants, and S. Bonnet, "Temperature Dependence of Triplet-Triplet Annihilation Upconversion in Phospholipid Membranes," *J. Phys. Chem. B*, vol. 121, no. 4, pp. 780–786, 2017, doi: 10.1021/acs.jpcb.6b10039.

[162] R. Tian *et al.*, "Development of a novel anti-tumor theranostic platform: a near-infrared molecular upconversion sensitizer for deep-seated cancer photodynamic therapy," *Chem Sci*, vol. 10, no. 43, pp. 10106–10112, 2019, doi: 10.1039/c9sc04034j.

[163] A. V Bandura and S. N. Lvov, "The Ionization Constant of Water over Wide Ranges of Temperature and Density," *J. Phys. Chem. Ref. Data*, vol. 35, no. 1, pp. 15–30, 2006, doi: 10.1063/1.1928231.